https://doi.org/10.1016/j.actamat.2017.02.035

Microstructures-based constitutive analysis for mechanical properties of gradient-nanostructured 304 stainless steels

Linli Zhu[1*], Haihui Ruan[2], Aiying Chen[3,4], Xiang Guo[5,6], and Jian LU[3*]

[1]Department of Engineering Mechanics and Key Laboratory of Soft Machines and Smart Devices of Zhejiang Province, Zhejiang University, Hangzhou 310027, Zhejiang Province, China

[2]Department of Mechanical Engineering, The Hong Kong Polytechnic University, Kowloon, Hong Kong, China

[3]Department of Mechanical and Biomedical Engineering, City University of Hong Kong, Kowloon, Hong Kong, China

[4]School of Material Science and Engineering, University of Shanghai for Science and Technology, Shanghai 200093, China

[5]School of Mechanical Engineering, Tianjin University, Tianjin 300354, China;

[6]Tianjin Key Laboratory of Nonlinear Dynamics and Control, Tianjin 300072, China

Abstract: Austenite stainless steels with gradient nanostructure exhibit exceptional combination of high yield strength and high ductility. In order to describe their structure-property relation, a theoretical model is proposed in this work, in which the depth-dependent bimodal grain size distribution and nanotwin-nanograin composite structure are taken into account. The micromechanical model and the Voigt rule of mixture are adopted in deriving the constitutive relations. Furthermore, the evolution and influence of the nano/micro cracks/voids are considered for predicting the failure strain. The numerical results based on the theoretical model agree well with experimental results in

[*] Corresponding authors at: Department of Engineering Mechanics, Zhejiang University, Hangzhou 310027, Zhejiang Province, China (Linli Zhu). Tel.: +86 571-87953110.
E-mail address: llzhu@zju.edu.cn (Linli Zhu), jianlu@cityu.edu.hk (Jian Lu)

terms of the yield strength, ductility, and the strain hardening rate, demonstrating that the proposed model can well describe the mechanical properties of gradient-nanostructured austenite stainless steels. We further study the variations of the yield strength and ductility of gradient-nanograined and gradient-nanotwinned 304 stainless steels with different distribution of grain size and twin spacing along the depth, which shows that the present model can be applied to optimize the combination of strength and ductility of the gradient-nanostructured metals by tuning depth-dependent distributions of microstructures.

***Keywords**:* Gradient-nanograined metals; Gradient-nanotwinned metals; Mechanical properties; Microstructural size; Bimodal grain size distribution; Micromechanical model.

1. Introduction

Modern industry demands high-performance alloys which possess both high yield strength and good ductility [1,2], although these two properties are mutually exclusive. Various traditional strengthening methods such as the grain refinement, cold working, alloying and phase transformation [3-5] are accompanied with poor ductility and reduced work-hardening capability [6-8]. In the past decade, great efforts have been made and several approaches are suggested to achieve superior strength-ductility combination. They include generating nanometer-scale twins in the grains of polycrystalline metals [9], engineering the bi/multi-modal grain size distribution in nanostructured materials [10,11], and introducing the hierarchical nanostructures, such as the subnanometer intragranular solute cluster, nanometer-scale solute structures and the nanograins/nanotwins, in metals [8,12,13]. More recently, introducing the gradient-microstructures, in which the size of grains or the spacing of twins increases from several nanometers at the surface to the several micrometers in the core, was proposed as an effective methodology to achieve the high yield strength and high ductility, as well as the enhanced fatigue properties [13-20]. Owing to the large variety of microstructures and their distributions, it is necessary to establish a theoretical model for describing their influence on the mechanical properties so that an optimized combination of strength and ductility based on the gradient-nanostructured metallic materials can be predicted.

Many theoretical works have been carried out to explore the deformation mechanisms and predict the mechanical properties of nanotwinned metals. Molecular dynamics (MD) simulation provides evidence of the plastic deformation mechanism, which leads to the convincing explanation of the relation between the twin boundaries (TBs) and the mechanical properties such as the strength, strain hardening and toughness. It has been confirmed that the pinning effect of TBs on dislocations is the dominant mechanism for improving the yield strength [21,22]. Since TBs act as the additional sources of dislocations and gradually lose their coherence, the nanotwinned metals exhibit the increased strain hardening and the high ductility [23-26]. MD analysis further illuminates that the softening and detwinning behaviors in nanotwinned polycrystalline metals originate from the activities of twinning partial dislocations and the nucleation of these partials at TB-GB intersections [27-29]. Furthermore, the size-dependent fracture behaviors in hierarchically nanotwinned metals have been investigated in details using the large-scale MD simulation [30-32]. For the macroscopic mechanical behaviors of nanotwinned metals, various mechanism-based theoretical models have been proposed to describe the constitutive relation and the twin spacing-dependent strength and ductility. Dao *et al*. [33] and Jerusalem *et al*. [34] proposed the two- and three-dimensional plasticity models, respectively, to predict the constitutive relation and the ductility of nanotwinned copper, but softening behaviors are not taken into account in these works. Mirkhani and Joshi [35] presented a discrete twin crystal plasticity model to describe the strengthening-softening transition when the twin spacing decreases in nanotwinned copper. Wei [36] proposed a scaling law of the maximum strength of nanotwinned metals in studying the relation between the grain size and the critical twin spacing. Besides, Zhu *et al*. [37] developed a mechanism-based plasticity model to describe yield strength and ductility of nanotwinned metals as functions of the grain size and twin spacing, and to further predict the grain-size-dependent critical twin spacing at the strengthening-softening transition. Gu *et al*. [38,39] also proposed a unified mechanistic model to describe plastic behaviors of nanograined or nanotwinned metals, which are influenced by grain size and twin spacing. For the hierarchically nanotwinned fcc metals, an extended mechanism-based plasticity model is proposed to predict the flow stress and ductility, both of which are dependent on the twin spacing and grain size [40].

Since the experimental studies revealed that the nanostructured metallic materials with bimodal grain size distribution possess both high strength and good elongation [10,41-43], a number of works have investigated their deformation mechanisms and predicted their mechanical properties. For instance, it has been shown that the existence of dendrites and cavitations on the surface and microcracks in the materials [44-46] are the essential factors to improve the plasticity in bimodal metals/alloys. For modeling the mechanical properties of bimodal metallic materials, the micromechanical composite models (e.g., the Ramberg-Osgood formula) and finite element methods are often utilized to establish the constitutive relation and failure behavior [47]. Joshi *et al*. [48] adopted the secant

Mori–Tanaka (M-T) mean-field approach to predict the mechanical properties of bimodal metals. The modified Mori-Tanaka method was also employed to predict the yield strength, strain hardening, and failure strain in bimodal nickels and coppers by taking the influence of the nano/micoracke s into account [49,50]. Micromechanical models were widely applied in analyzing the influence of volume fraction and grain size on yield strength and ductility of bimodal metals [51-53]. On the other hand, the finite element method is also effective in studying the strengthening of nanograins/nanotwins in metals with bimodal grain size distribution [54-56].

For gradient-nanostructured metals, a few of theoretical works have been performed to simulate the stress-strain response and optimize the yield strength and ductility in this kind of nanostructured metals. To name a few, Li *et al*. [57] applied the finite element method to discuss the major factors affecting the strength and elongation and the process parameters of surface nanocrystallization techniques to achieve the good combination of strength and ductility in gradient-nanograined metals. Liu and Mishaevsky Jr. [58] developed a finite element model to investigate the mechanical and damage behavior of gradient ultrafine-grained titanium. The mechanism-based continuum plasticity models were also proposed to describe the yield strength, ductility as well as the strain hardening in gradient nanograined metals [59]. For the gradient-nanotwinned metals, the finite element simulations were conducted to investigate the relation between the gradient twin structures and mechanical properties such as the strength, the elongation, and the fatigue resistance in linearly gradient steel samples [13,20]. With the aid of the surface mechanical attrition treatment (SMAT), the gradient-nanograined and gradient-nanotwinned 304 stainless steel (304ss) was obtained through controlling the intensity of surface impact [14]. The depth-dependent X-ray diffraction patterns and TEM images demonstrate that there exists the bimodal grain size distribution at different depths. In the gradient-nanotwinned samples, the nanograins and nanotwins are both generated in the coarse grains at different depths. Tensile tests indicated that these gradient-nanostructured 304ss possesses very high yield strength and retains good plasticity [14]. However, the quantitative relation between the gradient distribution of nanostructures and the mechanical properties is still lacking.

The objective of this paper is to explore theoretically the impacts of the gradient-nanograins (GNG) and gradient-nanotwins (GNT) in 304ss on the mechanical properties. To achieve this objective, the corresponding micromechanical models for such two kinds of gradient-nanostructured metals (GNM) are developed in the framework of the modified mean field approach. In modelling the gradient structure in 304ss, the composite structures consisting of nanotwins and nanograins and the bimodal distribution of grain size are considered. Moreover, the micromechanical damage model is applied to analyze the failure behavior due to the evolution of nano/micro-voids/cracks in the nanograined/nanotwinned matrix. We apply the proposed models to describe the stress-strain response and predict the mechanical properties of the gradient-nanostructured 304ss. Numerical results show that the theoretical prediction agrees well with the experimental results.

2. Microstructured models for gradient-nanostructured 304 stainless steels

Experimental studies have proved that engineering the gradient microstructures in nanostructured metallic materials is an effective approach to improve the synergy of strength and ductility [13-20]. In such gradient-nanostructured metals (GNM), the grain size or twin spacing changes from nanometer scale at the surface to micrometer scale in the core. Assuming a uniform uniaxial strain during the experimental tensile testing, the Voigt rule of mixture (ROM) can be adopted to describe the effective stress and strain in gradient-nanostructured metals [60] and it leads to the expression of the equivalent stress $\tilde{\sigma}_{xx}$:

$$\tilde{\sigma}_{xx}=\frac{\sum_{i=1}^{n}{}_{i}\sigma_{xx}^{\mathrm{N}}\mathrm{H}_{i}^{\mathrm{N}}+\sigma_{xx}^{\mathrm{C}}\mathrm{H}^{C}}{\mathrm{H}}, \tag{1}$$

where i, N, and C denote the ith layer, nanostructured region, and coarse-grained region, respectively. n is the number of layers in the nanostructured region; ${}_{i}\sigma_{xx}^{\mathrm{N}}$ and σ_{xx}^{C} are the stresses applied on ith layer of nanostructured region and coarse-grained region, respectively; $\mathrm{H}_{i}^{\mathrm{N}}=\mathrm{H}^{\mathrm{N}}/n$, H^{C}, and H are the thickness of ith layer in nanostructured region, CG core, and the entire gradient-nanostructured metals, respectively. Since each layer of gradient-nanostructured metals consists of two phases as showed in figure 1, the stress ${}_{i}\sigma_{xx}^{\mathrm{N}}$ of nanostructured layers could be calculated from the micromechanical models for the dual-phase metals [61]. In the next section, the theoretical framework of the composite model is presented and it is employed to obtain the stress-strain relations of each layer of GNG-304ss and those of GNT-304ss.

3. The theoretical description for composite structures in GNM

In order to model the stress ${}_{i}\sigma_{xx}^{\mathrm{N}}$ in the regions of both nanotwins and nanograins, the modified mean-field approach is adopted to describe the stress-strain response of these composite nanostructures [49,50,61,64].

3.1 A micromechanical model for dual-phase metals

The bimodal nanostructure in GNG-304ss can be regarded as a composite structure consisting of the small-grained phase (α'-martensite nanograins) and the large-grained phase (γ-austenite ultrafine grains), as shown in figure 1(b). The typical bimodal structure in the 304 stainless steel after SMAT is shown in Fig. 1(e) [14], which exemplified the composite structure. The nanotwinned composite structure can also be considered as a two-phase structure, namely, the nanotwinned matrix phase and nanograined phase, as shown in figure 1(c).

We consider the scenario that the dual-phase composite is subjected to a uniform strain $\bar{\boldsymbol{\varepsilon}}$. The basic relations for $\boldsymbol{\sigma}^{(\alpha)}(z)$ of the constituent α and $\bar{\boldsymbol{\sigma}}(z)$ of the composite will be derived in terms of the secant modulus tensor $\mathbf{L}_0^S(z)$ and the plastic strain $\boldsymbol{\varepsilon}^{p(1)}(z)$ of the inclusion [60], where z is depth from the surface. We further introduce a linear elastic reference material with the modulus tensor $\mathbf{L}_0^S(z)$ the relation:

$$\boldsymbol{\sigma}^0(z)=\mathbf{L}_0^S(z)\bar{\boldsymbol{\varepsilon}}. \tag{2}$$

By introducing $\tilde{\boldsymbol{\sigma}}$ and $\tilde{\boldsymbol{\varepsilon}}$ to be the difference from the reference material, the mean stress of the matrix phase is given by

$$\boldsymbol{\sigma}^{(0)}(z)=\boldsymbol{\sigma}^0(z)+\tilde{\boldsymbol{\sigma}}=\mathbf{L}_0^S(z)(\bar{\boldsymbol{\varepsilon}}+\tilde{\boldsymbol{\varepsilon}})=\mathbf{L}_0^S(z)\boldsymbol{\varepsilon}^{(0)}. \tag{3}$$

Considering the additional perturbations $\boldsymbol{\sigma}^{ap}$ and $\boldsymbol{\varepsilon}^{ap}$, the mean stress of inclusion phase, labeled by superscript (1), can be expressed as follows by means of Eshelby's equivalent principle,

$$\boldsymbol{\sigma}^{(1)}(z)=\boldsymbol{\sigma}^0(z)+\tilde{\boldsymbol{\sigma}}+\boldsymbol{\sigma}^{ap}=\mathbf{L}_1(z)(\boldsymbol{\varepsilon}^{(1)}-\boldsymbol{\varepsilon}^{p(1)})=\mathbf{L}_0^S(z)(\boldsymbol{\varepsilon}^{(1)}-\boldsymbol{\varepsilon}^{p(1)}-\boldsymbol{\varepsilon}^*). \tag{4}$$

Here, $\boldsymbol{\varepsilon}^{(1)} = \bar{\boldsymbol{\varepsilon}} + \tilde{\boldsymbol{\varepsilon}} + \boldsymbol{\varepsilon}^{ap}$ and $\boldsymbol{\varepsilon}^{*}$ is the Eshelby's equivalent transformation strain. The perturbed strain $\boldsymbol{\varepsilon}^{ap}$ is associated with the total transformation strain $(\boldsymbol{\varepsilon}^{p(1)} + \boldsymbol{\varepsilon}^{*})$ and Eshelby's tensor, given by

$$\boldsymbol{\varepsilon}^{ap} = S_0^s(\boldsymbol{\varepsilon}^{p(1)} + \boldsymbol{\varepsilon}^{*}). \tag{5}$$

For a spherical inclusion, $S_0^s = (\alpha_0^s, \beta_0^s)$ in which

$$\alpha_0^s = (1+v_S^s)/3(1-v_S^s); \beta_0^s = 2(4-5v_S^s)/15(1-v_S^s). \tag{6}$$

Considering the weighted mean $\bar{\boldsymbol{\varepsilon}} = \sum c^{(\alpha)}\boldsymbol{\varepsilon}^{(\alpha)}$, $(\alpha = 0,1)$, we have

$$\tilde{\boldsymbol{\varepsilon}} = -c^{(1)}\boldsymbol{\varepsilon}^{ap} = -c^{(1)}S_0^s(\boldsymbol{\varepsilon}^{p(1)} + \boldsymbol{\varepsilon}^{*}). \tag{7}$$

Then, the stress of the composite structure can be calculated from the weighed mean

$${}_i\boldsymbol{\sigma}_{xx}^{\mathrm{N}} = \bar{\boldsymbol{\sigma}}(z) = \sum c^{(\alpha)}\boldsymbol{\sigma}^{(\alpha)} = \mathbf{L}_0^S(z)[\bar{\boldsymbol{\varepsilon}}\text{-}c^{(1)}(\boldsymbol{\varepsilon}^{p(1)} + \boldsymbol{\varepsilon}^{*})]. \tag{8}$$

The equivalent transformation strain can be found from Eq. (4) as,

$$\boldsymbol{\varepsilon}^{p(1)} + \boldsymbol{\varepsilon}^{*} = -\frac{(\mathbf{L}_1 - \mathbf{L}_0^S)\bar{\boldsymbol{\varepsilon}} - \mathbf{L}_1\boldsymbol{\varepsilon}^{p(1)}}{[c^{(0)}(\mathbf{L}_1 - \mathbf{L}_0^S)S_0^s + \mathbf{L}_0^S]}. \tag{9}$$

Substituting Eqs. (7) and (9) into the mean strains of the matrix phase $\boldsymbol{\varepsilon}^{(0)} = \bar{\boldsymbol{\varepsilon}} + \tilde{\boldsymbol{\varepsilon}}$, and the one of the inclusion $\boldsymbol{\varepsilon}^{(1)} = \bar{\boldsymbol{\varepsilon}} + \tilde{\boldsymbol{\varepsilon}} + \boldsymbol{\varepsilon}^{\mathbf{pt}}$, we can obtain the relation between the uniform strain of the composite and the mean strain of the constituents, as shown in Appendix. We can also substitute Eqs. (7) and (9) into Eqs. (3) and (4) and thus obtain the mean stress components of the matrix phase and those of the inclusion, which is also detailed in Appendix. Finally, the macroscopic stress of the composite follows from Eq. (8)

$$\begin{aligned}
&\bar{\sigma}_{kk}(z) = 3\kappa_0\left[1 + \frac{c^{(1)}(\kappa_1 - \kappa_0)}{c^{(0)}\alpha_0^s(\kappa_1 - \kappa_0) + \kappa_0}\right]\bar{\varepsilon}_{kk}(z), \\
&\bar{\sigma}'_{ij}(z) = 2\mu_0^s\left\{\left[1 + \frac{c^{(1)}(\mu_1 - \mu_0^s)}{c^{(0)}\beta_0^s(\mu_1 - \mu_0^s) + \mu_0^s}\right]\bar{\varepsilon}'_{ij}(z) - \frac{c^{(1)}\mu_1}{c^{(0)}\beta_0^s(\mu_1 - \mu_0^s) + \mu_0^s}\varepsilon_{ij}^{p(\mathrm{T})}(z)\right\}
\end{aligned}. \tag{10}$$

where $\bar{\sigma}'_{ij}$ and $\bar{\varepsilon}'_{ij}$ are the deviatoric stress and strain components. These expressions are identical to those of dual-phase metals when the representative volume of the composite structure is subjected to the uniform strain [61].

3.2 Stress-strain relation of the constituents in nanostructured composites

In order to calculate the stress $\boldsymbol{\sigma}^{(\alpha)}(z)$ and strain $\boldsymbol{\varepsilon}^{(\alpha)}$ of constituents in nanostructured composite of gradient-nanostructured metals, the related stress-strain response of the αth phase is determined in the framework of the elastoplasticity. The total strain rate $\dot{\boldsymbol{\varepsilon}}$ can be decomposed into its elastic and plastic parts $\dot{\boldsymbol{\varepsilon}}^{(\alpha)}=\dot{\boldsymbol{\varepsilon}}^{(\alpha)\mathbf{e}}+\dot{\boldsymbol{\varepsilon}}^{(\alpha)\mathbf{p}}$. The elastic strain rate-stress rate follows the linear elastic constitutive relation

$$\dot{\boldsymbol{\varepsilon}}^{(\alpha)\mathbf{e}}=\mathbf{M}^{(\alpha)}:\dot{\boldsymbol{\sigma}}^{(\alpha)}, \tag{11}$$

where $\mathbf{M}^{(\alpha)}$ is the elastic compliance tensor of the αth phase. Based on the conventional J_2-flow rule of plasticity, the plastic strain rate is proportional to the deviatoric stress $\boldsymbol{\sigma}^{(\alpha)\prime}$,

$$\dot{\boldsymbol{\varepsilon}}^{(\alpha)\mathrm{p}}=\frac{3\dot{\varepsilon}^{(\alpha)\mathrm{p}}}{2\sigma_{\mathrm{e}}{}^{(\alpha)}}\boldsymbol{\sigma}^{(\alpha)\prime}. \tag{12}$$

Here, $\sigma^{(\alpha)\prime}{}_{ij}=\sigma^{(\alpha)}{}_{ij}-\sigma^{(\alpha)}{}_{kk}\delta_{ij}/3$ and $\sigma_{\mathrm{e}}{}^{(\alpha)}=\sqrt{3\sigma^{(\alpha)\prime}{}_{ij}\,\sigma^{(\alpha)\prime}{}_{ij}/2}$ is the von Mises equivalent stress. $\dot{\varepsilon}^{(\alpha)\mathrm{p}}$ is the equivalent plastic strain rate which is determined by

$$\dot{\varepsilon}^{(\alpha)\mathrm{p}}=\dot{\varepsilon}^{(\alpha)}[\frac{\sigma_{\mathrm{e}}{}^{(\alpha)}}{\sigma_{flow}{}^{(\alpha)}}]^{\mathrm{m}_0}, \tag{13}$$

where $\dot{\varepsilon}^{(\alpha)}=\sqrt{2\dot{\varepsilon}^{(\alpha)\prime}{}_{ij}\,\dot{\varepsilon}^{(\alpha)\prime}{}_{ij}/3}$ is the equivalent strain rate and $\dot{\varepsilon}^{(\alpha)\prime}{}_{ij}=\dot{\varepsilon}^{(\alpha)}_{ij}-\dot{\varepsilon}^{(\alpha)}_{kk}\delta_{ij}/3$. $\sigma_{flow}{}^{(\alpha)}$ is the flow stress of the αth phase, and m_0 is the rate-sensitivity exponent. Then, the related secant Young's modulus and secant Poisson ratio of αth phase can be written as

$$E^{(\alpha)s}(z)=\frac{\sigma^{(\alpha)}}{\varepsilon^{(\alpha)\mathbf{e}}+\varepsilon^{(\alpha)\mathbf{p}}}=\frac{E^{(\alpha)}}{1+\frac{E^{(\alpha)}\varepsilon^{(\alpha)}}{\sigma_{flow}^{(\alpha)}}(\frac{\sigma^{(\alpha)}}{\sigma_{flow}^{(\alpha)}})^{\mathrm{m}_0-1}},\ v^{(\alpha)s}(z)=\frac{1}{2}-(\frac{1}{2}-v^{(\alpha)}\frac{E^{(\alpha)s}}{E^{(\alpha)}}), \quad (14)$$

where $E^{(\alpha)}$ and $v^{(\alpha)}$ denote the Young's modulus and Poisson's ratio of the αth phase in nanostructured composite metals. Since the deformation mechanisms in nanograined metals and nanotwinned metals are different from those in coarse-grained metals, the flow stresses in nanostructured regions and coarse-grained region are used in corresponding calculations. Therefore, the secant bulk and shear moduli of the αth phase, which is supposed to be isotropic, is given by

$$\kappa_\alpha(z)=\frac{E^{(\alpha)s}}{3(1-2v^{(\alpha)s})},\mu_\alpha(z)=\frac{E^{(\alpha)s}}{2(1+v^{(\alpha)s})}. \quad (15)$$

4. Flow stresses of the constituents in the nanostructured composite metals

4.1 Flow stress in the bimodal composite

With the increase of the depth in the GNG-304ss, the grain size in the ultrafine-grained γ-austenite phase increases to the micrometer scale. Therefore, the γ-austenite phase can be regarded as the coarse-grained phase in the bimodal metals. The intragrain dislocation-mediated interaction will dominate the primary deformation mechanism, which is often described by the Taylor-type flow stress, giving as

$$\sigma_{flow}^{A}(z)=\sigma_0+M\alpha\mu b\sqrt{\rho_I}+\sigma_{\mathrm{b}}, \quad (16)$$

where α, μ and M are the empirical constant, the shear modulus and the Taylor factor, respectively. σ_0 is the lattice friction stress and σ_b represents the back stress. ρ_{I} is the density of dislocations in the crystal interior of grains, determined by [65]

$$\frac{\partial \rho_I}{\partial \varepsilon^{\mathrm{p}}} = M\left(\frac{1}{bd_G(z)} + \frac{\psi\sqrt{\rho_I}}{b} - k_{20}\left(\frac{\dot{\varepsilon}^{\mathrm{p}}}{\dot{\varepsilon}_0}\right)^{-\mathrm{n}_0^{-1}} \rho_I\right). \tag{17}$$

Here, ψ is a proportionality factor, k_{20} and $\dot{\varepsilon}_0$ are the constants, and n_0 is inversely proportional to the temperature. Note from Eq. (16) that the Taylor evolution law includes the isotropic strain hardening, which is characterized by Eq. (17), and the back stress induces the kinematic hardening that can be expressed by

$$\sigma_b = M\,\frac{\mu b}{d_G(z)} N_{\mathrm{b}}, \tag{18}$$

where N_{b} is the number of dislocations blocked at the grain boundaries in the coarse-grained phase and it is a function of the plastic strain.

For the nano-grained α'-martensite phase, the strength is much higher than that of coarse grains, owing to the blocking mechanism of grain boundaries. Consequently, the contribution of grain boundaries to the plastic deformation must be taken into account during plastic deformation. The dislocation density in the grain boundary dislocation pile-up zones (GBDPZs) is used to explore the influence of grain boundaries on the flow stress, i.e.,

$$\sigma_{flow}^{M}(z) = \sigma_0 + M\alpha\mu b\sqrt{\rho_I + \rho_{GB}}, \tag{19}$$

in which ρ_{I} can be obtained from Eq. (17), and the density of dislocations in the GBDPZ is given by [36]

$$\rho_{GB} = k^{GB}\frac{\eta^{GB}}{b}. \tag{20}$$

Here, $k^{GB} = 6d_{GBDPZ}/\phi^{GB}d_G(z)$, d_{GBDPZ} is the thickness of GBDPZ and ϕ_3 is the geometrical factor.

4.2 Flow stress in the nanotwinned composite

The twin boundaries inside coarse grains, also blocking dislocation movement, enable accumulation of dislocations along them and bring about much higher dislocation density than those in the grains without twin boundaries. Such dislocation-based activities in TBs dominate the plastic deformation, leading to the simultaneous improvement in strength and ductility. For the nanotwinned composite, the nano-scale twin lamellae play the essential role in strengthening the materials and also maintain the good plasticity for composite metals. Here, the dislocation pile-up zones (DPZ) of twin boundaries are proposed to describe the dislocations-based flow stress in nanotwinned phase, given as

$$\sigma_{flow}^{\mathrm{T}}(z) = \sigma_0 + M\alpha\mu b\sqrt{\rho_I + \rho_{TB}}, \tag{21}$$

where ρ_{I} is the density of dislocations between twin boundaries, determined by Eq. (17), and ρ_{TB} is the dislocation density in the DPZ nearby the twin boundaries, expressed as [37,40]:

$$\rho_{TB}(z) = \frac{\chi_0}{d_G{}^2} + \frac{\chi_1}{d_G d_{TB}(z)} - \frac{\chi_2}{d_{TB}^2(z)}. \tag{22}$$

In Eq. (22), χ_0, χ_1 and χ_2 are constants independent of the grain size and the twin spacing. Due to the depth-dependent twin spacing $d_{TB}(z)$, the dislocation density ρ_{TB} becomes also depth-dependent.

5. Failure behavior of gradient-nanostructured metals

5.1 The criterion for microcracks generations in nanostructured metals

Experimental and theoretical studies revealed that the nano/micro-scale defects such as the nanovoids or nano/microcracks generated during plastic deformation play an essential role in mechanical behaviors of nanostructured metals. For example, the dendrites, cavitations, and the nano/microcracks dominate the fracture mechanism in bimodal metals or alloys [44-46]. The nano/microcracks that appear in the grain boundaries or in the twinned matrix result in the failure behaviors of nanograined metals and nanotwinned metals, respectively [66-69].

Note that the opening crack can be characterized by a continuous array of dislocations [70]. When the crack grows, more dislocations emanate from the crack tip. Inspired by this physical picture, the stress-based criterion for generating nano/microcracks is that the flow stress τ^i_{flow} of *i*th phase is larger than the necessary stress τ_{crit} for nucleating a dislocation [37], i.e.,

$$\tau^i_{flow} \geq \tau_{crit} . \tag{24}$$

It is assumed that the nanostructured composite metal will start to generate the nano/microcracks when the flow stress of *i*th phase exceeds the stress necessary to nucleate dislocations in the nanograined phase or the nanotwinned phase. The critical shear stress to generate a dislocation has been described thoroughly by Asaro and Rice [71]. By considering the nucleation of a dislocation loop from a stress concentration, the free energy of the expanding loop can be given as:

$$U = \mu b_1^2 (2-v)/8(1-v) r \ln(r/r_0) - 1.4 b_1 \tau_{crit} \sqrt{\pi d^*/2} (r^{3/2} - r_0^{-3/2}) + \gamma \frac{1}{2} \pi (r^2 - r_0^2) , \tag{25}$$

in which γ is stacking fault energy, b_1 is the magnitude of the Burgers vector. d^* equals d_{TB} for TBs and d_G for GBs. Combining with the conditions of $\partial U / \partial r = 0; \partial^2 U / \partial r^2 = 0$, we can determine the critical value of the applied shear stress τ_{crit}.

5.2 Change of mechanical properties of the cracked phase

When a large number of nano/microcracks are generated in the nanostructured composite metal during deformation, the influence of them must be taken into account. On the one hand, the presence of nano/microcracks leads to the change of overall stress-strain relation of the nanograined or the nanotwinned phase. On the other hand, the nano/microcracks lead to more dislocations in the grain boundaries of nanograined phase, giving rise to the additional back stress effect in the nanograined phase. The effective-medium approach involving the effect of microcracks is utilized to obtain the stress and strain relation.

Suppose that the representative volume element (RVE) is subjected to tractions in equilibrium with a uniform far-field stress of σ^{∞}. The average strain in a solid with nano/microcracks is the sum of regular and singular terms as [72]

$$\bar{\boldsymbol{\varepsilon}}_{\mathbf{CP}} = \mathbf{M} : \boldsymbol{\sigma}^{\infty} + \sum_i (< \underline{\mathbf{b}} > \mathbf{n} + \mathbf{n} < \underline{\mathbf{b}} >)^i S^i / (2V), \tag{26}$$

where $\mathbf{M}$ is the compliance tensor, V is the volume of the RVE and the superscript i is a quantity of the ith nano/microcrack. S^i is the surface area, $\underline{\mathbf{b}}$ is the average opening displacement discontinuity vector and $\mathbf{n}$ stands for the unit vector normal to the crack face. For the nano/microcrack with isotropic (random) orientation distribution, the effective modulus and Poisson's ratio follow

$$E = E_0[1 + \frac{16(1-v_0^2)(1-3v_0/10)}{9(1-v_0/2)}\rho]^{-1}$$
$$G = G_0[1 + \frac{16(1-v_0)(1-v_0/5)}{9(1-v_0/2)}\rho]^{-1}; v = v_0[1 + \frac{8(1\text{-}v_0^2)}{45(1-v_0/2)}\rho]^{-1} \quad (27)$$

Here, ρ is the density of nano/microcracks in the materials, which can be described by the strain-based Weibull distribution function

$$\rho = \mathrm{R}_0(1 - f_W(\varepsilon_p)) = \mathrm{R}_0[1 - \exp(-(\varepsilon_p/\varepsilon_0)^{\mathrm{M}}], \quad (28)$$

where R_0 is a reference density of nano/microcracks, $f_W(\varepsilon_p)$ is the strain-based Weibull distribution function and ε_0 is the reference strain and M the Weibull modulus. Suppose that all nano/microcracks are vertical to the loading direction, the effective moduli are simplified to be:

$$E = E_0[1 + \frac{16(1-v_0^2)}{3}\rho]^{-1}; G = G_0[1 + \frac{8(1+v_0)}{3(1-v_0/2)}\rho]^{-1}. \quad (29)$$

Since the nano/microcracks-induced back stress appears in the nanograined phase, the flow stress of nanograined phase is changed into

$$\sigma_{flow}^{\mathrm{M}}(z) = \sigma_0 + M\alpha\mu b\sqrt{\rho_I + \rho_{GB}} + \sigma_b^*, \quad (30)$$

where σ_b^* is additional back stress originated from the nano/microcrack, simply expressed as $\sigma_b^* = M\mu bN^*/d_G$. Here, N^* is the number of additional dislocations accumulated at the grain boundaries, which varies with the plastic strain following the evolution law as:

$$\frac{dN^*}{d\varepsilon^p} = \frac{\zeta^*}{b}(1 - \frac{N^*}{N_B^*}), \quad (31)$$

where ε^{p}, ζ^{*}, and N_{B}^{*} are the plastic strain, the mean spacing between slip bands, and the maximum number of dislocation loops at the grain boundaries in the nanograined phase, respectively.

6. Results and discussion

We now apply the developed theoretical models in this section to predict the constitutive response and failure behavior of gradient-nanostructured 304ss. The relations between mechanical properties and the size, volume fraction as well as the different gradient distribution of microstructures are explored. The material parameters used in all calculations are given in Table 1, which were extracted from the literature [73,74] or obtained by fitting the experimental results [14]. With the aid of these parameters, the constitutive relations of the GNG-304ss and GNT-304ss are simulated, and the yield strength and ductility are also predicted based on the proposed models.

6.1 Distribution of size and volume fraction of microstructures in 304ss after SMAT

The important result of SMAT process is the depth-dependent size and volume faction of microstructural components [14]. To investigate mechanical behaviors of the 304ss prepared by SMAT, the depth-dependent grain size, twin spacing, and volume fraction of the microstructural components must be determined through fitting the experimental measurements. Figure 2(a) plots the experimental results [14] and fitting curves of sizes of α'-martensite grain and γ-austenite grain against the depth. The distribution of grain size can be described using

$$d_{\mathrm{G}}(x)=d_{\mathrm{G0}}(1-\{1+\exp[(x-D_{\mathrm{ep}})/c_{0}]\}^{-1}), \tag{32}$$

where, d_{G0} is the initial size of coarse grains before SMAT process, D_{ep} and c_{0} are the fitting constants, both of which are different for α'-martensite and γ-austenite grains.

Figure 2(b) shows the fitting curve and experimental data of depth-dependent volume fractions of α'-martensite grains and γ-austenite grains. The distribution function of α'-martensite grains is expressed as

$$f_\alpha = P_0 + (1 - P_0)\exp(-x / c_1), \tag{33}$$

where c_1 **and** P_0 **are the fitting parameters. And the volume fraction of γ-austenite grains is** $f_\gamma = 1 - f_\alpha$**.**

For the GNT-304ss, the twin spacing changes along the depth from several tens of nanometers at the top layer to several hundreds at the central zone. To describe the experimental data [14] as shown in Figure 3(a), we adopt the fitting function

$$d_{TW} = d_{T0} + d_{T1}\exp(x / c_2), \tag{34}$$

where d_{T0}, d_{T1}, and c_2 are fitting constants. Since the α'-martensite nanograins are generated in γ-austenite nanotwinned grains, we suppose the martensite grain size is approximately equal to the twin spacing, namely, $d_{\alpha'\text{-G}}(x) = d_{TW}(x)$. The fitting curve of volume fraction of the nanotwinned phase against the depth is plotted in Figure 3(b), which is based on the equation

$$f_{TW}(x) = f_{T0} - f_{T1}\exp(-x / c_3), \tag{35}$$

where f_{T0}, f_{T1}, and c_3 are fitting constants. Then, we can obtain the volume fraction of α'-martensite nanograins as $f_{\alpha'\text{-}G} = 1 - f_{TW}$.

6.2 Comparison with experiments on constitutive response and failure strain

Once the depth-dependent volume fraction and size of microstructures are determined, the stress-strain responses of the gradient-nanostructured 304ss can be calculated based on the proposed models. After selecting the proper parameters for the tunable constants in the models, we plot the numerical results of the stress-strain relation for the GNG-304ss in Figure 4(a). The experimental data of stress-strain relation of GNG-304ss [14] are also presented in the figure. It is noted that the calculated stress-strain response based on the proposed model agrees well with the experimental results. The predicted yield strength and the failure strain are 600 MPa and 40%, in a good agreement with the measurements. The strain hardening and work-hardening rate both agree with the experiments very well, as shown in Figure 4(b). Therefore, the proposed model for GNG metals can work well for predicting the mechanical behaviors for 304ss with gradient microstructure.

The stress-strain relation of GNT-304ss is further investigated using the model of GNT-metals as proposed in Sections 4 and 5. By using the parameters provided in Table 1, the mechanical properties of GNT-304ss, including the yield strength, the strain hardening, and the ductility, are numerically obtained and plotted in Figure 5(a), where the experimental results [14] are also shown. It is interesting to note that the calculated stress-strain relation agrees well with the experimental measurements. We find that the predicated work-hardening rate is also in line with the experimental data, as shown in Figure 5(b), indicating that the proposed model presented in this work can admirably describe the mechanical behaviors of GNT-metals. **To further validate the proposed model, we apply it to describe stress-strain responses of the linearly gradient 304ss prepared by the pre-rotation treatment procedure [20]. Figure 5(c) shows the comparison between the theoretical and experimental results [20], demonstrating a good agreement. Since the gradient distribution of twin spacing is not measured in Ref. [20], we use our model to predict the twin spacing distribution along the depth, which renders the parameters in the distribution function Eq. (34)** d_{T0}, d_{T1} **and** c_2

to be 50 nm, 16 nm and 790 μm for 180° pre-twisted sample, respectively, and 20 nm, 16 nm and 810 μm for 360° pre-twisted sample, respectively.

6.3 Contributions from different strengthening mechanisms

For the sake of a comprehensive understanding on strengthening mechanisms in the gradient-nanostructured 304ss, we discuss the influences of the α'-martensite grains and γ-austenite grains in GNG-304ss, together with the effects of γ-austenite nanotwins and α'-martensite nanograins in GNT-304ss on mechanical properties. Figure 6(a) compares the contribution of the smaller α'-martensite grains and larger γ-austenite grains on the strength of the GNG-304ss. It is noted that both the gradient-distributed α'-martensite grains and γ-austenite grains contribute to yield strength of the GNG-304ss. However, the strain hardening behavior is dominated by the gradient-distributed γ-austenite grains, and there is no hardening effect from α'-martensite grains. Figure 6(b) further shows the influence of the gradient-distributed volume fraction of γ-austenite grains and α'-martensite grains on the stress-strain response. There is small volume fraction of α'-martensite grains in GNG-304ss, leading to the weak contribution to the strengthening and strain hardening from α'-martensite grains. When the material is full of the γ-austenite nanograins, there is no change for the strain hardening compared with that of the gradient-distributed volume fraction of γ-austenite grains, while the yield strength increases from 300 MPa to 450 MPa. Therefore, one can conclude from Figure 6 that the α'-martensite grains and the γ-austenite grains have different contributions on the strengthening and hardening behaviors, which are sensitive to the volume fraction of each phases.

Figure 7(a) shows the strain-strain curves for GNT-304ss and compares the contributions from different strengthening mechanisms, namely, nanotwin strengthening and α'-martensite nanograin strengthening. The influence of back stress is also demonstrated by switching its effect on (solid line) and off (dashed dot line) in the figure. Due to the small volume fraction of the nanograins, the γ-austenite nanotwins is the main cause of the large yield strength and the enhanced strain hardening rate. Furthermore, the nano/microcrack-induced back stress has a significant contribution to the strain hardening as shown in Figure 7(a). We further analyzed the influence of the gradient-distributed volume fraction of γ-austenite nanotwin and α'-martensite nanograin on the stress-strain response. However, the yield strength for the uniform-distributed nanotwinned γ-austenite is merely slightly larger than that for gradient-distributed volume fraction. The strain hardening rate has almost no change. This is owing to the fact that the volume fraction of γ-austenite nanotwin in the GNT-304ss has been sufficiently large as shown in Fig. 7(b).

6.4 Microstructural size-dependent mechanical properties

Since the constitutive models of gradient-nanostructured metals presented in Sections 3 and 4 involve the depth-dependent sizes of microstructures, the stress-strain responses of gradient-nanostructured 304ss are sensitive to the twin spacing, the grain size, and their gradient distributions. Figure 8(a) shows the stress-strain curves of GNG-304ss with different gradient distribution parameter D_{ep} in Eq. (32). It is noted from the figure that when D_{ep} increases from 200 μm to 400 μm, the yield strength rises notably. We also find that the increment of yield strength changes with D_{ep} nonlinearly, as shown in Figure 8(b). The reason is that with the larger D_{ep}, the grain size increases with the depth more slowly, leading to much more nanograins, as seen in figure 8(c). Furthermore, the failure strains of GNG-304ss with different D_{ep} are predicted by accounting for the influence of nano/microcracks. The yield strength and the failure strain for different D_{ep} are plotted in Figure 8(d). It is noticeable that with D_{ep} increasing, the yield strength is increased, while the failure strain is decreased, which is the trade-off between yield strength and ductility.

The flow stress of the nanotwinned phase of GNT-metals, described by Eq. (22), shows that the dislocation density is related to the twin spacing and the grain size. Therefore, the total stress-strain response of GNT-304ss depends on the size of microstructures, such as the twin spacing and grain size in the nanotwinned phase. Since the grain size in the nanotwinned phase is unchanged after the SMAT process, only the twin-spacing-dependent mechanical properties are analyzed in GNT-304ss. Figure 9(a) depicts the stress-strain responses of GNT-304ss with different parameter d_{T0} in Eq. (34). In the gradient distribution function of twin spacing, d_{T0} refers to the initial twin spacing at the surface layer. The larger d_{T0} indicates the larger overall twin spacing along the depth. Consequently, it can be found from Figure 9(a) that the yield strength is dependent on d_{T0} remarkably. The yield strength decreases from 900 MPa to 650 MPa with d_{T0} varying from 10 nm to 90 nm, as shown in Figure 9(b). We further studied the variation of failure strain with d_{T0} and plot the yield strength against the failure strain for different d_{T0} in Figure 9(c). It is intriguing to note that when d_{T0} decreases from 90 nm to 10 nm, both the yield strength and the failure strain are improved, and that the yield strength and ultimate strength increase with the failure strain almost linearly. It implies that the higher yield strength and better ductility can be achieved in the GNT metals through controlling the twin spacing, which is consistent with the finding in nanotwinned polycrystalline fcc metals.

6.5 Predicted yield strength and failure strain for different volume fractions

The gradient-nanostructured 304ss can be regarded as a composite material containing the α'-martensite nanograins and γ-austenite grains/nanotwinned grains. Therefore, the mechanical properties of the gradient nanostructured 304ss are dependent on the volume faction of each component. Figure 10(a) shows stress-strain relations of the GNG-304ss with different volume fraction of α'-martensite nanograined phase, where P_0 is the parameter in Eq. (33). The larger P_0 indicates the more α'-martensite nanograins in the GNG-304ss, as shown in Figure 10(b). Figure 10(a) exhibits that the yield strength increases with P_0. Furthermore, this dependence is almost linear, as shown in Figure 10(c). The failure strain of the GNG-304ss can also be predicted with different values of P_0. We present the predicted yield strength and failure strain in Figure 10(d) for different P_0. For the GNT-304ss, we plot the corresponding stress-strain relations in Figure 10(e) with different values of parameter f_T in the function of volume fraction of the nanotwinned phase, namely, Eq. (35). Fig. 10(f) shows that when the value of f_{T0} increases from 0.1 to 0.5, the yield strength only changes slightly. Since the yield strength of the nanotwinned phase is close to that of the nanograined phase, the yield strength is improved 60 MPa when f_{T0} increases from 0.1 to 0.5, as shown in Figure 10(f).

7. Conclusions

In this work, the theoretical model for describing the strength and ductility of the gradient-nanostructured metals have been developed and successfully applied to GNG-304ss and GNT-304ss. Because of existence of the composite structures in the gradient-nanostructured 304ss, the proposed constitutive models are based on the framework of the micromechanical analysis which enables the description of the stress-strain relation of dual-phase metals. The constitutive relations of the nanograined phase, nanotwinned phase, and the coarse-grained phase are explicitly formulated. For the gradient-nanograined 304ss which involves the bimodal nanostructures, the constitutive relations for both the nanograined phase and the coarse-grained phase are used. For the gradient-nanotwinned 304ss, the constitutive relations for nanograined phase and nanotwinned phase are included. Moreover, the impacts of nano/microcracks generated during plastic deformation are considered to predict the failure strain of the gradient-nanostructured 304ss.

After identifying the gradient distributions of volume fraction and size of microstructures in gradient-nanostructured 304ss, our models can predict the stress-strain relations of the GNG-304ss and GNT- 304ss, which agree well with experimental results. It was revealed that the proposed constitutive models can describe the mechanical performances of the gradient-nanostructured 304ss. These models can also predict the mechanical properties such as the yield strength and ductility of the gradient-nanostructured metals. We further analyzed the different strengthening mechanisms in the gradient-nanostructured 304ss. Numerical results revealed that the different gradient distributions of size and volume fraction of the nanograined phase in the GNG-304ss and the nanotwinned phase in the GNT-304ss, which can be controlled in the SMAT process, lead to a large range of yield strength and ductility. The proposed theoretical models capture the features of the mechanical responses of the gradient-nanostructured 304ss, which will shed the light on optimizing the size and distribution of microstructures in gradient-nanostructured materials to achieve exceptional strength and ductility in metallic materials.

Acknowledgements

The authors gratefully acknowledge the support received from the National Natural Science Foundation of China (Grant nos. 11472243, 11372214, 50890174, 11621062), the National Key Basic Research Program (Grant no. 2012CB932203), Doctoral Fund of Ministry of Education of China (20130101120175), the Research Grants Council of the Hong Kong Special Administrative Region of China under grants CityU8/CRF/08 and GRF/CityU519110, the Croucher Fundation CityU9500006, and the internal research funds (G-UA2L) of Hong Kong Polytechnic University.

References

[1] G. Frommeyer, U. Brux, P. Neumann, Supra-ductile and high-strength manganese-TRIP/TWIP steels for high energy absorption purposes, ISI J. Int. 43 (2003) 438-446.

[2] B.C. DeCooman, K.G. Chin, J.K. Kim, High Mn TWIP steels for automotive applications. In: New Trends and Developments in Automotive System Engineering, Ed. Chiaberge, M., In. Tech. (2011) 101-128.

[3] Y.T. Zhu, X.Z. Liao, Nanostructured metals: retaining ductility, Nat. Mater. 3 (2004) 351-352.

[4] M.A. Meyers, A. Mishra, D.J. Benson, Mechanical properties of nanocrystalline materials, Prog. Mater. Sci. 51 (2006) 427-556.

[5] R.O. Ritchie, The conflicts between strength and toughness, Nat. Mater. 10 (2011) 817-822.

[6] M. Dao, L. Lu, R.J. Asaro, J.T.M. De Hosson, E. Ma, Toward a quantitative understanding of mechanical behavior of nanocrystalline metals, Acta Mater. 55 (2007) 4041-4065.

[7] O. Bouaziz, S. Allain, C.P. Scott, P. Cugy, D. Barbier, High manganese austenitic twinning induced plasticity steels: A review of the microstructure properties relationships, Curr. Opin. Solid State Mat. Sci. 15 (2011) 141-168.

[8] H.N. Kou, J. Lu, Y. Li, High-strength and high-ductility nanostructured and amorphous metallic materials, Adv. Mater. 26 (2014) 5518-5524.

[9] L. Lu, X. Chen, X. Huang, K. Lu, Revealing the maximum strength in nanotwinned copper, Science 323 (2009) 607-610.

[10] Y.M. Wang, M.W. Chen, F.H. Zhou, E. Ma, Extraordinarily high tensile ductility in a nanostructured metal, Nature 419 (2002) 912-915.

[11] Y.H. Zhao, T. Topping, J.F. Bingert, J.J. Thornton, A.M. Dangelewicz, Y. Li, W. Liu, Y.T. Zhu, Y.Z. Zhou, E.J. Lavernia, High tensile ductility and strength in bulk nanostructured nickel, Adv. Mater. 20 (2008) 3028-3033.

[12] P.V. Liddicoat, X.Z. Liao, Y.H. Zhao, Y.T. Zhu, M.Y. Murashkin, E.J. Lavernia, R.Z. Valiev, S.P. Ringer, Nanostructural hierarchy increases the strength of aluminium alloys, Nat. Commun. 1 (2010) 63(1-7).

[13] Y.J. Wei, Y.Q. Li, L.C. Zhu, Y. Liu, X.Q. Lei, G. Wang, Y.X. Wu, Z.L. Mi, J.B. Liu, H.T. Wang, H.J. Gao, 2014. Evading the strength-ductility trade-off dilemma in steel through gradient hierarchical nanotwins, Nat. Commun. 5 (2014) 3580(1-8).

[14] A.Y. Chen, H.H. Ruan, J. Wang, H.L. Chan, Q. Wang, Q. Li, J. Lu, The influence of strain rate on the microstructure transition of 304 stainless steel, Acta Mater. 59 (2011) 3697-3709.

[15] H.T. Wang, N.R. Tao, K. Lu, Architectured surface layer with a gradient nanotwined structure in a Fe-Mn austenitic steel, Scr. Mater. 68 (2013) 22-27.

[16] K. Lu, Making strong nanomaterials ductile with gradients, Science 345 (2014) 1455-1456.

[17] X.L. Wu, P. Jiang, L. Chen, F.P. Yuan, Y.T. Zhu, Extraordinary strain hardening by gradient structure, Proc. Natl. Acad. Sci. USA 111 (2014) 7197-7201.

[18] X.P. Tan, Y.H. Kok, Y.J. Tan, M. Descoins, D. Mangelinck, S.B. Tor, K.F. Leong, C.K. Chua, Graded microstructure and mechanical properties of additive manufactured Ti–6Al–4V via electron beam melting, Acta Mater. 97 (2015) 1-16.

[19] X.L. Wu, M.X. Yang, F.P. Yuan, L. Chen, Y.T. Zhu, Combining gradient structure and TRIP effect to produce austenite stainless steel with high strength and ductility, Acta Mater. 112 (2016) 337-346.

[20] Z.W. Ma, J.B. Liu, G. Wang, H.T. Wang, Y.J. Wei, H.J. Gao, Strength gradient enhances fatigue resistance of steels, Sci. Rep. 6 (2016) 22156 (1-11).

[21] Y.G. Zheng, J. Lu, H.W. Zhang, Z. Chen, Strengthening and toughening by interface-mediated slip transfer reaction in nanotwinned copper, Scr. Mater. 60 (2009) 508-511.

[22] P. Chowdhury, H. Sehitoglu, H.J. Maier, R. Rateick, Strength prediction in NiCo alloys-The role of composition and nanotwins, Int. J. Plast. 79 (2016) 237-258.

[23] A. Froseth, P.M. Derlet, H. Van Swygenhoven, Grown-in twin boundaries affecting deformation mechanisms in nc-metals, Appl. Phys. Lett. 85 (2004) 5863-5865.

[24] T. Zhu, J. Li, A. Samanta, H.G. Kim, S. Suresh, Interfacial plasticity governs strain rate sensitivity and ductility in nanostructured metals, Proc. Natl. Acad. Sci. 104 (2007) 3031-3036.

[25] Z.H. Jin, P. Gumbsch, K. Albe, E. Ma, K. Lu, H. Gleiter, H. Hahn, Interactions between non-screw lattice dislocations and coherent twin boundaries in face-centered cubic metals, Acta Mater.56 (2008) 1126-1135.

[26] L.Q. Pei, C. Lu, X. Zhao, L. Zhang, K.Y. Cheng, G. Michal, K. Tieu, Brittle versus ductile behaviour of nanotwinned copper: A molecular dynamics study, Acta Mater. 89 (2015) 1-13.

[27] J. Wang, N. Li, O. Anderoglu, X. Zhang, A. Misra, J.Y. Huang, J.P. Hirth, Detwinning mechanisms for growth twins in face-centered cubic metals, Acta Mater. 58 (2010) 2262-2270.

[28] X.Y. Li, Y.J. Wei, L. Lu, K. Lu, H.J. Gao, Dislocation nucleation governed softening and maximum strength in nano-twinned metals, Nature 464 (2010) 877-880.

[29] Y.X. Zhu, Z.H. Li, M.S. Huang, Y. Liu, Strengthening mechanisms of the nanolayered polycrystalline metallic multilayers assisted by twins, Int. J. Plast. 72 (2015) 168-184.

[30] F.P. Yuan, X.L. Wu, Size effects of primary/secondary twins on the atomistic deformation mechanisms in hierarchically nanotwinned metals, J. Appl. Phys. 113 (2013a) 203516(1-6).

[31] F.P. Yuan, X.L. Wu, Atomistic scale fracture behaviours in hierarchically nanotwinned metals, Philosophical Magazine 93 (2013) 3248-3259.

[32] L.G. Sun, X.Q. He, L.L. Zhu, J. Lu, Two softening stages in nanotwinned Cu, Philosophical Magazine 94 (2014) 4037–4052.

[33] M. Dao, L. Lu, Y. Shen, S. Suresh, Strength, strain-rate sensitivity and ductility of copper with nanoscale twins, Acta Mater. 54 (2006) 5421-5432.

[34] A. Jerusalem, M. Dao, S. Suresh, R. Radovitzky, Three-dimensional model of strength and ductility of polycrystalline copper containing nanoscale twins, Acta Mater. 56 (2008) 4647-4657.

[35] H. Mirkhani, S.P. Joshi, Crystal plasticity of nanotwinned microstructures: A discrete twin approach for copper, Acta Mater. 59 (2011) 5603-5617.

[36] Y.J. Wei, Scaling of maximum strength with grain size in nanotwinned fcc metals, Phys. Rev. B 83 (2011) 132104(1-4).

[37] L.L. Zhu, H.H. Ruan, X.Y. Li, M. Dao, H.J. Gao, J. Lu, Modeling grain size dependent optimal twin spacing for achieving ultimate high strength and related high ductility in nanotwinned metals, Acta Mater. 59 (2011) 5544–5557.

[38] P. Gu, M. Dao, R.J. Asaro, S. Suresh, A unified mechanistic model for size-dependent deformation in nanocrystalline and nanotwinned metals, Acta Mater. 59 (2011) 6861-6868.

[39] P. Gu, M. Dao, S. Suresh, Analysis of size-dependent slip transfer and inter-twin flow stress in a nanotwinned fcc metal, Acta Mater. 67 (2014) 409-417.

[40] L.L. Zhu, S.X. Qu, X. Guo, J. Lu, Analysis of the twin spacing and grain size effects on mechanical properties in hierarchically nanotwinned face-centered cubic metals

based on a mechanism-based plasticity model, J. Mech. Phys. Solid. 76 (2015) 162-179.

[41] B. Ahn, E.J. Lavernia, S.R. Nutt, Dynamic observations of deformation in an ultrafine-grained Al–Mg alloy with bimodal grain structure, J. Mater. Sci. 43 (2008) 7403-7408.

[42] H. Simchi, A. Simchi, Tensile and fatigue fracture of nanometric alumina reinforced copper with bimodal grain size distribution, Mater. Sci. Eng. A 507 (2009) 200-206.

[43] L. Farbaniec, G. Dirras, A. Krawczynska, F. Mompiou, H. Couque, F. Naimi, F. Bernard, D. Tingaud, Powder metallurgy processing and deformation characteristics of bulk multimodal nickel, Mater. Character. 94 (2014) 126-137.

[44] G. He, M. Hagiwara, J. Eckert, W. Löser, Inverse deformation-fracture responses between dendrite and matrix in Ti-base nanostructure-dendrite composite, Phil. Mag. Lett. 84 (2004) 365-375.

[45] G.J. Fan, H. Choo, P.K. Liaw, E.J. Lavernia, Plastic deformation and fracture of ultrafine-grained Al–Mg alloys with a bimodal grain size distribution, Acta Mater. 54 (2006) 1759-1766.

[46] Z.H. Lee, V. Radmilovic, B. Ahn, E.J. Lavernia, S.R. Nutt, Tensile deformation and fracture mechanism of bulk bimodal ultrafine-grained Al-Mg alloy, Metall. Mater. Trans. A 41 (2010) 795-801.

[47] R.Q. Ye, B.Q. Han, E.J. Lavernia, Simulation of deformation and failure process in bimodal Al alloys, Metall. Mater. Trans. A 36 (2005) 1833-1840.

[46] S.P. Joshi, K.T. Ramesh, B.Q. Han, E.J. Lavernia, Modeling the constitutive response of bimodal metals, Metall. Mater. Trans. A 37 (2006) 2397-2404.

[49] L.L. Zhu, J. Lu, Modelling the plastic deformation of nanostructured metals with bimodal grain size distribution, Int. J. Plast. 30-31 (2012) 166-184.

[50] L.L. Zhu, S.Q. Shi, K. Lu, J. Lu, A statistical model for predicting the mechanical properties of nanostructured metals with bimodal grain size distribution, Acta Mater. 60 (2012) 5762-5772.

[51] B. Raeisinia, C.W. Sinclair, W.J. Poole, C.N. Tome, On the impact of grain size distribution on the plastic behaviour of polycrystalline metals, Modelling Simul. Mater. Sci. Eng. 16 (2008) 025001(1-15).

[52] S. Ramtani, G. Dirras, H.Q. Bui, A bimodal bulk ultra-fine-grained nickel: experimental and micromechanical investigations, Mech. Mater. 42 (2010) 522-536.

[53] L.L. Zhu, X. Guo, H.H. Ruan, Simulating size and volume fraction-dependent strength and ductility of nanotwinned composite copper, ASME-J. Appl. Mech. 83 (2016) 071009.

[54] X. Guo, R. Ji, G.J. Weng, L.L. Zhu, J. Lu, Micromechanical simulation of fracture behavior of bimodal nanostructured metals, Mater. Sci. Eng. A 618 (2014) 479-489.

[55] H. Hosseini-Toudeshky, M. Jamalian, Simulation of micromechanical damage to obtain mechanical properties of bimdal Al using XFEM, Mech. Mater. 89 (2015) 229-240.

[56] X. Guo, G. Yang, G.J. Weng, The saturation state of strength and ductility of bimodal nanostructured metals, Mater. Lett. 175 (2016) 131–134.

[57] J.J. Li, S.H. Chen, X.L. Wu, A.K. Soh, J. Lu, The main factor influencing the tensile properties of surface nano-crystallized graded materials, Mater. Sci. Eng. A 527 (2010) 7040-7044.

[58] H.S. Liu, Jr. Mishnaevsky, Gradient ultrafine-grained titanium: Computational study of mechanical and damage behavior, Acta Mater. 71 (2014) 220-233.

[59] J.J. Li, S.H. Chen, X.L. Wu, A.K. Soh, A physical model revealing strong strain hardening in nano-grained metals induced by grain size gradient structure, Mater. Sci. Eng. A 620 (2015) 16-21.

[60] J.J. Li, A.K. Soh, Modeling of the plastic deformation of nanostructured materials with grain size gradient, Int. J. Plast. 39 (2012) 88-102.

[61] G.J. Weng, The overall elastoplastic stress–strain relation of dual-phase metals, J Mech. Phys. Solid 38 (1990) 419-441.

[62] K. Lu, F.K. Yan, H.T. Wang, N.R. Tao, Strengthening austenitic steels by using nanotwinned austenitic grains, Scr. Mater. 66 (2012) 878-883.

[63] F.K. Yan, G.Z. Liu, N.R. Tao, K. Lu, Strength and ductility of 316L austenitic stainless steel strengthened by nano-scale twin bundles, Acta Mater. 60 (2012) 1059-1071.

[64] Y.P. Jiang, X.P. Shi, K. Qiu, Micromechanical modeling the plastic deformation of particle-reinforced bulk metallic glass composites, Metall. Mater. Trans. A 46 (2015) 3705-3712.

[65] U.F. Kocks and H. Mecking, The physics and phenomenology of strain hardening, Prog. Mater. Sci. 48 (2003) 171-273.

[66] Z.W. Shan, L. Lu, A.M. Minor, E.A. Stach, S.X. Mao, The effect of twin plane spacing on the deformation of copper containing a high density of growth twins, JOM 60 (2008) 71-74.

[67] H. Zhou, S. Qu, The effect of nanoscale twin boundaries on fracture toughness in nanocrystalline Ni, Nanotechnology 21 (2010) 035706.

[68] H. Wang, A. Nie, J. Liu, P. Wang, W. Yang, B. Chen, H. Liu, M. Fu, In situ TEM study on crack propagation in nanoscale Au thin films, Scr. Mater. 65 (2011) 377-379.

[69] Z. Zeng, X.Y. Li, L. Lu, T. Zhu, Fracture in a thin film of nanotwinned copper, Acta Mater. 98 (2015) 313-317.

[70] B.A. Bilay, J.D. Eshelby, Dislocations and the theory of fracture. In *Fracture*, vol. I , Ed. Liebowitz, H., Academic Press, New York (1969) 99-182.

[71] R.J. Asaro, S. Suresh, Mechanistic models for the activation volume and rate sensitivity in metals with nanocrystalline grains and nano-scale twins, Acta Mater. 53 (2005) 3369-3382.

[72] M. Kachanov, Elastic solids with many cracks and related problems, Adv. Appl. Mech. 30 (1994) 259-445.

[73] H.M. Ledbetter, N.V. Frederick, M.W. Austin, Elastic-constant variability in stainless-steel 304, J. Appl. Phys. 51 (1980) 305-309.

[74] M. Delince, Y. Brechet, J.D. Embury, M.G.D. Geers, P.J. Jacques, T. Pardoen, Structure-property optimization of ultrafine-grained dual-phase steels using a microstructure-based strain hardening model, Acta Mater. 55 (2007) 2337-2350.

Figure Captions

Figure 1. Schematic drawings of the gradient-nanostructured metals separated into *N* layers with the same strain in each layer during deformation (a), the

gradient-nanograined 304ss with bimodal grain size distribution (b), and the gradient-nanotwinned 304ss with composite structures (c). To exemplify the schematics, further shown are the cross-sectional SEM images of the gradient-nanograined 304ss with the bimodal grain size distribution (d), and gradient-nanotwinned 304ss with the depth-dependent twin density (e) [14].

Figure 2. The depth-dependence of Grain size (a) and volume fraction (b) of α'-martensite grains and γ-austensite grains in gradient-nanograined 304ss. The symbols and lines are the experimental data and fitting curves, respectively.

Figure 3. Twin spacing (a) and volume fraction of components (b) as functions of depth for the gradient-nanotwinned 304ss.

Figure 4. The stress-strain responses (a) and strain-dependent strain hardening rate (b) with a comparison between the experiments and theoretical results for the gradient-nanograined 304ss.

Figure 5. The comparison between the experimental and theoretical results on stress-strain responses (a) and strain hardening rate (b) for the gradient-nanotwinned 304ss prepared by SMAT [14] and stress-strain responses (c) for pre-twisted 304ss with linearly gradient nanostructures [20].

Figure 6. Comparison between different strengthening mechanisms in the gradient-nanograined 304ss (a), and the influence of the gradient distribution of components on the stress-strain response (b).

Figure 7. Separation of the strengthening contributions associated with nanotwins, nanograins as well as the back stress in the gradient-nanotwinned 304ss (a); and the influence of the gradient distribution of nanograins and nanotwins on the stress-strain response (b).

Figure 8. Predicted stress-strain relationship with different D_{ep} (a), the predicted yield strength varying with D_{ep} (b), the grain size distributed along the depth with different D_{ep} (c), and the predicted yield strength vs. failure strain for different grain size distribution (d) in the gradient-nanograined 304ss.

Figure 9. Predicted stress-strain relationship with different d_{T0} (a), the predicted yield strength varying with d_{T0} (b), and the predicted yield strength vs. failure strain for different d_{T0} (c) in the gradient-nanotwinned 304ss.

Figure 10. Predicted stress-strain relationship with different P_0 (a), the volume fraction distribution along the depth with different P_0 (b), the predicted yield strength varying with P_0 (c), and the predicted yield strength vs. failure strain (d) in the gradient-nanograined 304ss. The predicted stress-strain relationship with different f_{T0} (e), and the predicted yield strength varying with f_{T0} (f) in the gradient-nanotwinned 304ss.

Table Caption

Table 1. Descriptions, symbols, magnitudes, and equations in which the different parameters of the models appear

Table 1.

Description, symbol, magnitude, and equation in which the different parameters of the models appear

Parameter (Unit)	Symbol	Magnitude
Grain size (nm)	d_{G0}	15000
Elastic modulus (GPa)	E	199.6
Shear modulus (GPa)	μ	74
Poisson's ratio	ν	0.29
Magnitude of the Burgers vector (nm)	b	0.26
Taylor factor	M	3.06
Taylor constant	α	0.3
Thickness of GBDPZ (nm)	d_{GBDPZ}	3.58
Thickness of TBDPZ (nm)	d_{TBDPZ}	3.58
Maximum number of dislocation	N_0	1090
Maximum number of dislocation loops at the grain boundary	N_B^*	150
Mean spacing between slip bands (nm)	ζ^*	2
Dislocation density related parameters	χ_0, χ_1, χ_2	3.75×10^{-5}, 2.12×10^{4}, 1.74×10^{4}
Dynamic recovery constant	k_{20}	18.5
Proportionality factor	ψ	0.2
Dynamic recovery constant	n	12.25
Reference strain rate (s^{-1})	$\dot{\varepsilon}_0$	1.75
Geometric factor	ϕ^{TB}, $\phi_i (i=1,2)$	0.5~1.5
Gradient function parameter of γ-austenite (μm)	D_{ep}, c_0	275, 40
Gradient function parameter of α'- martensite (μm)	D_{ep}, c_0	300, 45
Gradient function parameter	P_0	0.6
Gradient function parameter (μm)	c_1, c_2, c_3	65, 148, 78
Gradient function parameter (nm)	d_{T0}, d_{T1}	12, 16
Gradient function parameter	f_{T0}, f_{T1}	0.936, 0.16

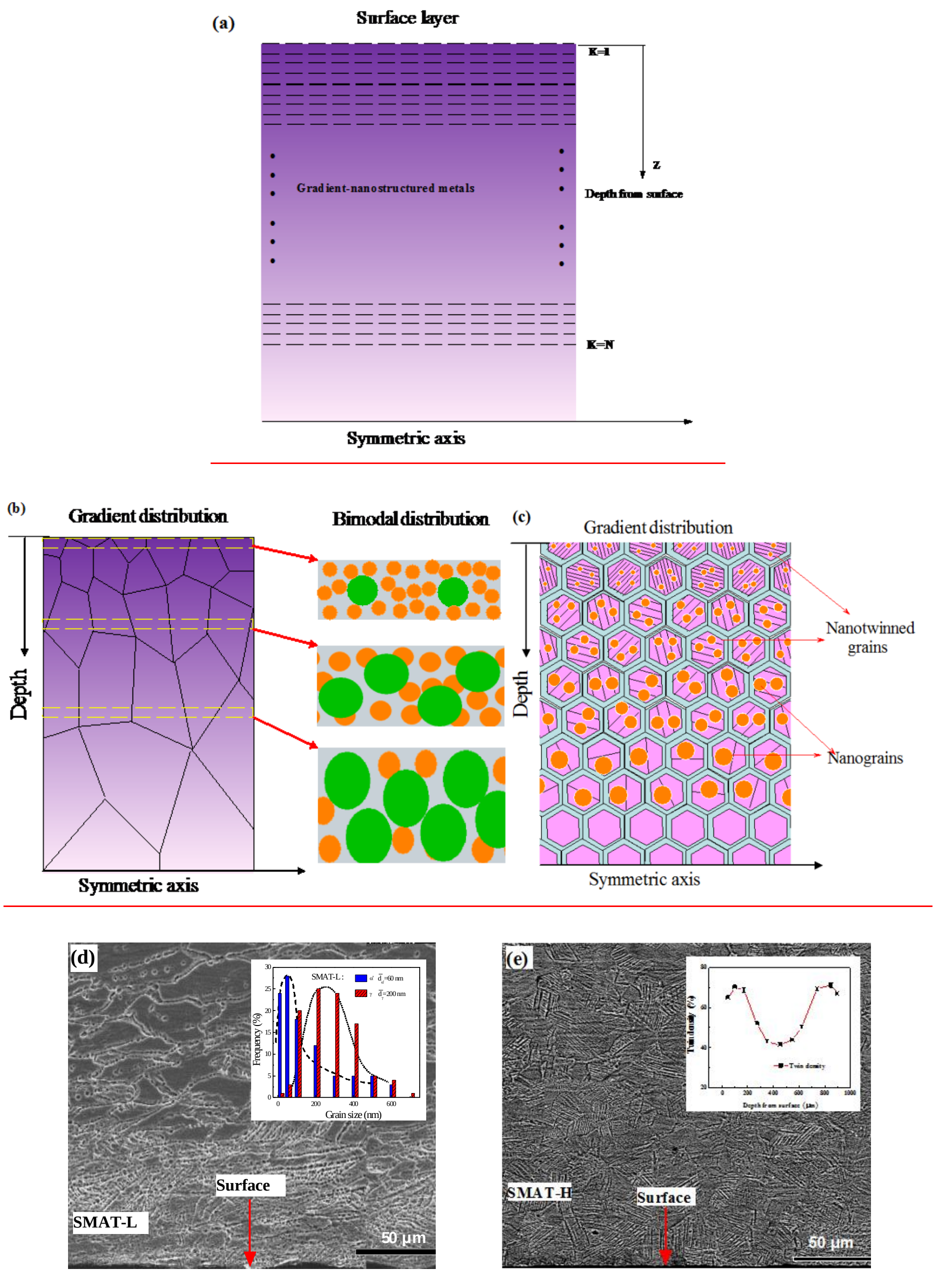

Figure 1. Schematic drawings of the gradient-nanostructured metals separated into *N* layers with the same strain in each layer during deformation (a), the gradient-nanograined 304ss with bimodal grain size distribution (b), and the gradient-nanotwinned 304ss with composite structures (c). To exemplify the schematics, further shown are the cross-sectional SEM images of the gradient-nanograined 304ss with the bimodal grain size distribution (d), and gradient-nanotwinned 304ss with the depth-dependent twin density (e) [14].

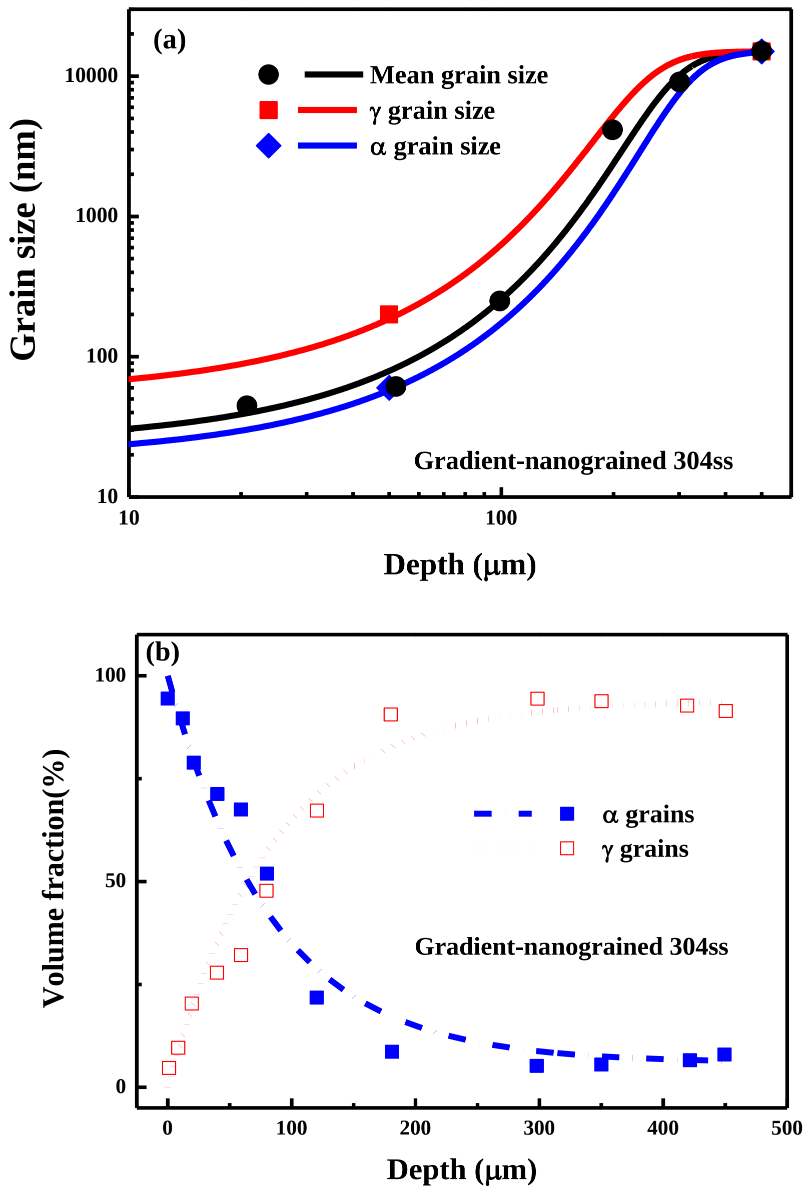

Figure 2. The depth-dependence of Grain size (a) and volume fraction (b) of α'-martensite grains and γ-austensite grains in gradient-nanograined 304ss. The symbols and lines are the experimental data and fitting curves, respectively.

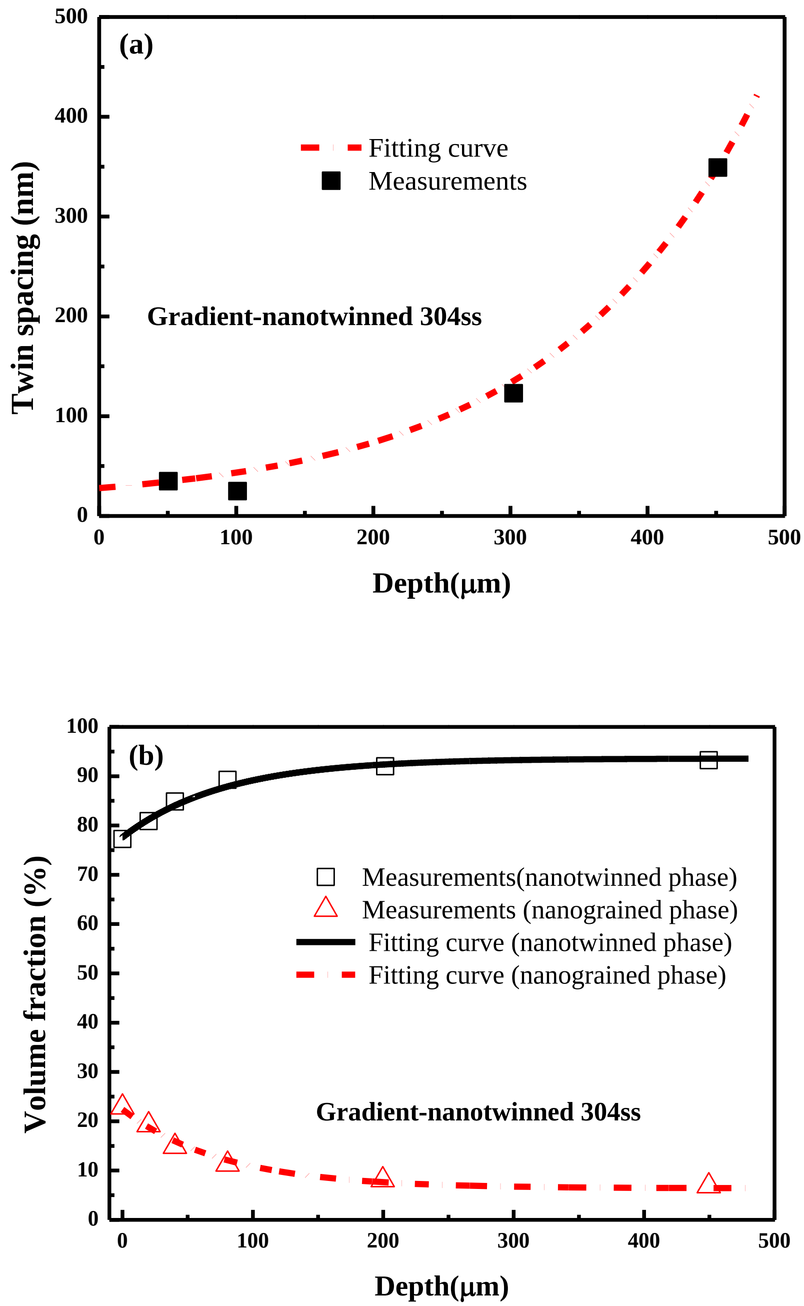

Figure 3. Twin spacing (a) and volume fraction of components (b) as the functions of depth for gradient-nanotwinned 304ss.

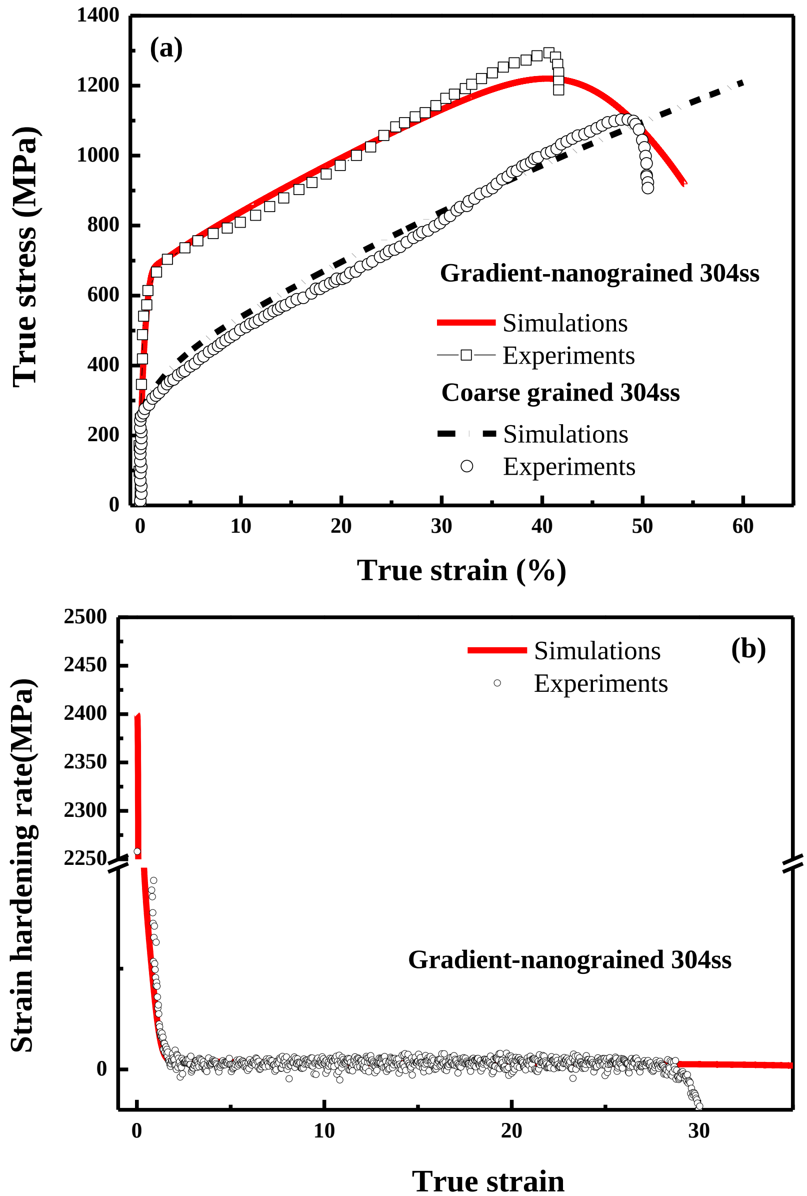

Figure 4. The stress-strain responses (a) and strain-dependent strain hardening rate (b) with a comparison between the experiments and theoretical results for the gradient-nanograined 304ss.

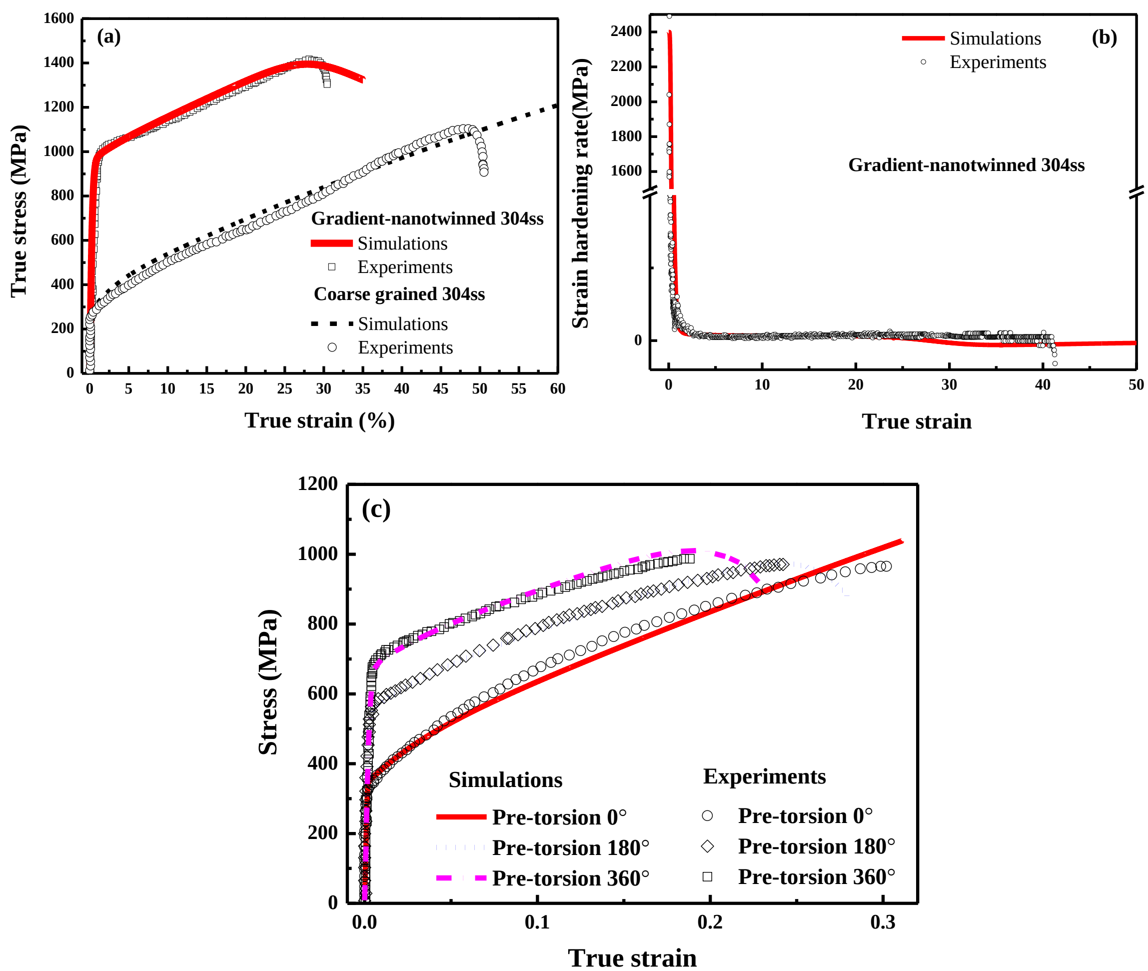

Figure 5. The comparison between the experimental and theoretical results on stress-strain responses (a) and strain hardening rate (b) for the gradient-nanotwinned 304ss prepared by SMAT [14] and stress-strain responses (c) for pre-twisted 304ss with linearly gradient nanostructures [20].

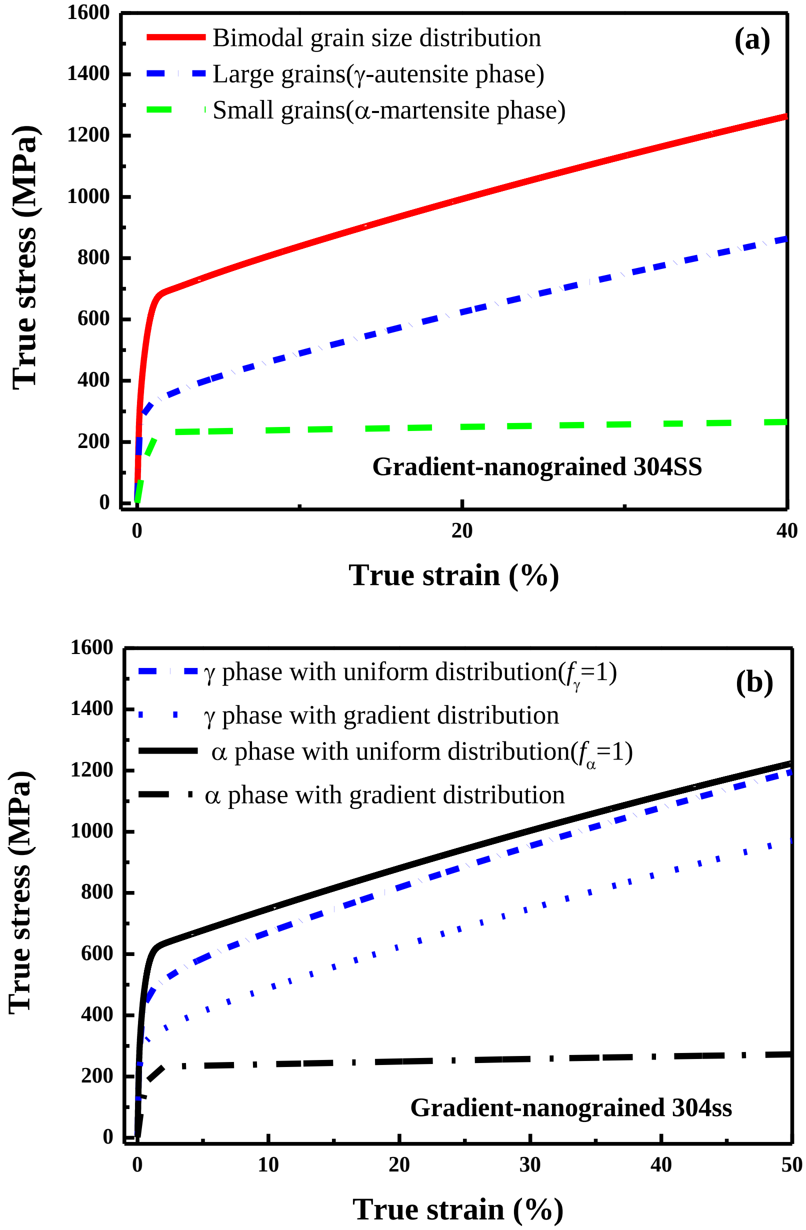

Figure 6. Comparison between different strengthening mechanisms in the gradient-nanograined 304ss (a), and the influence of the gradient distribution of components on the stress-strain response (b).

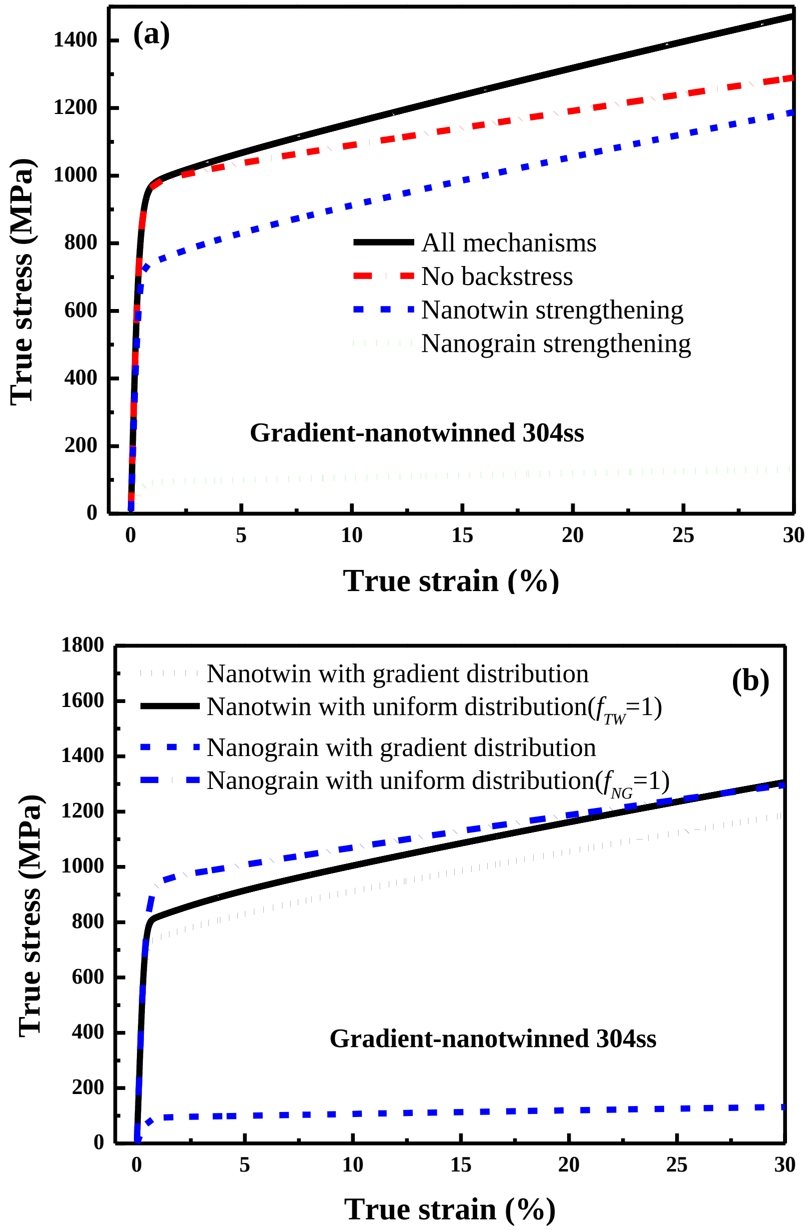

Figure 7. Separation of the strengthening contributions associated with nanotwins, nanograins as well as the back stress in the gradient-nanotwinned 304ss (a); and the influence of the gradient distribution of nanograins and nanotwins on the stress-strain response (b).

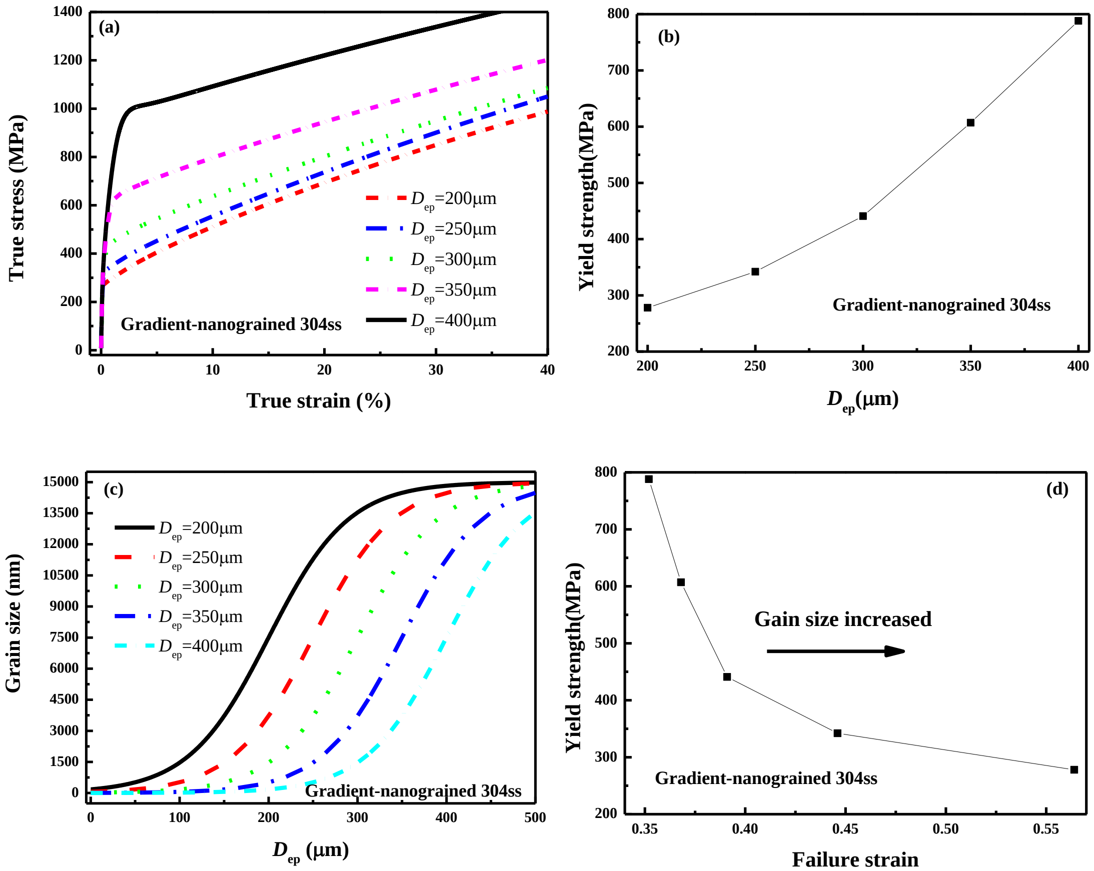

Figure 8. Predicted stress-strain relationship with different D_{ep} (a), the predicted yield strength varying with D_{ep} (b), the grain size distributed along the depth with different D_{ep} (c), and the predicted yield strength vs. failure strain for different grain size distribution (d) in the gradient-nanograined 304ss.

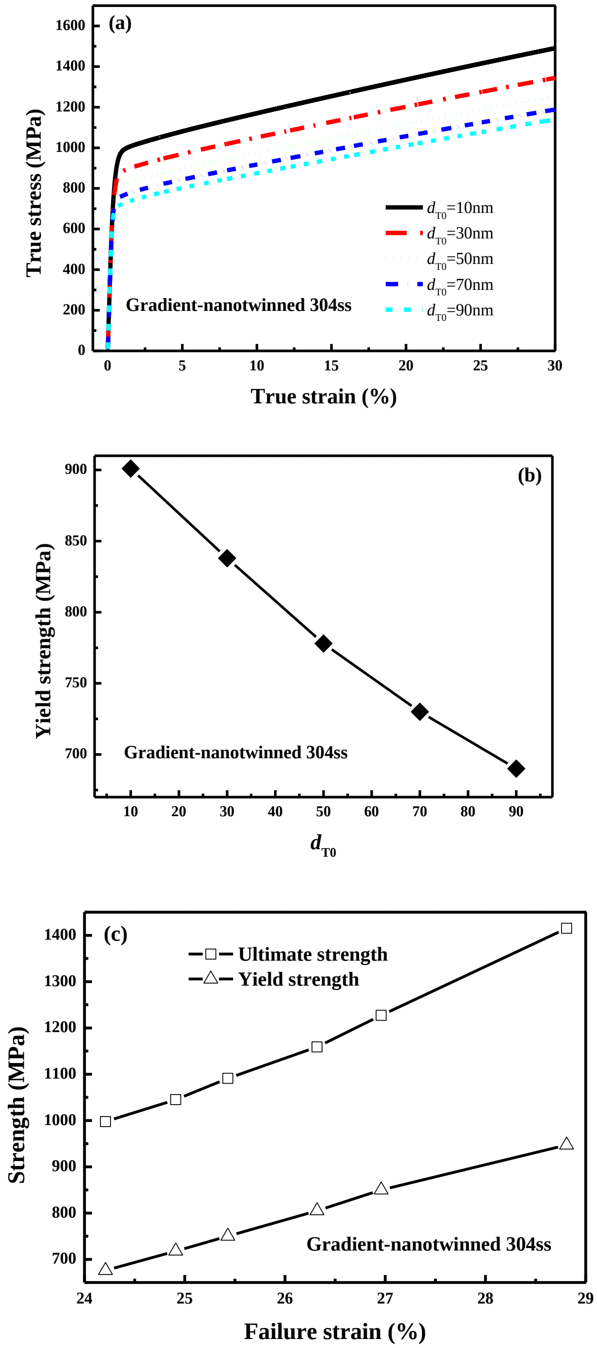

Figure 9. Predicted stress-strain relationship with different d_{T0} (a), the predicted yield strength varying with d_{T0} (b), and the predicted yield strength vs. failure strain for different d_{T0} (c) in the gradient-nanotwinned 304ss.

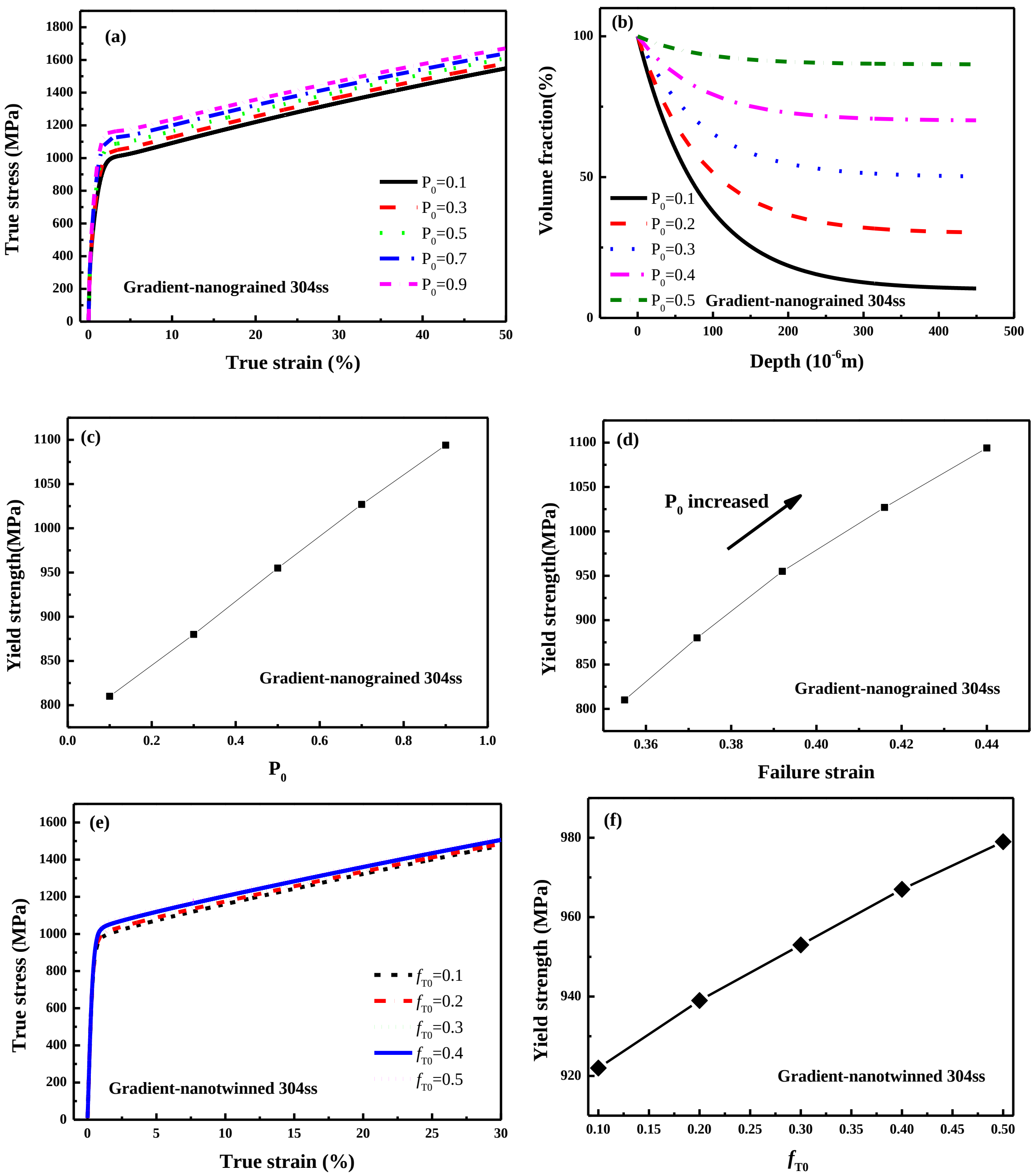

Figure 10. Predicted stress-strain relationship with different P_0 (a), the volume fraction distribution along the depth with different P_0 (b), the predicted yield strength varying with P_0 (c), and the predicted yield strength vs. failure strain (d) in the gradient-nanograined 304ss. The predicted stress-strain relationship with different f_{T0} (e), and the predicted yield strength varying with f_{T0} (f) in the gradient-nanotwinned 304ss.

Figure1a
Click here to download high resolution image

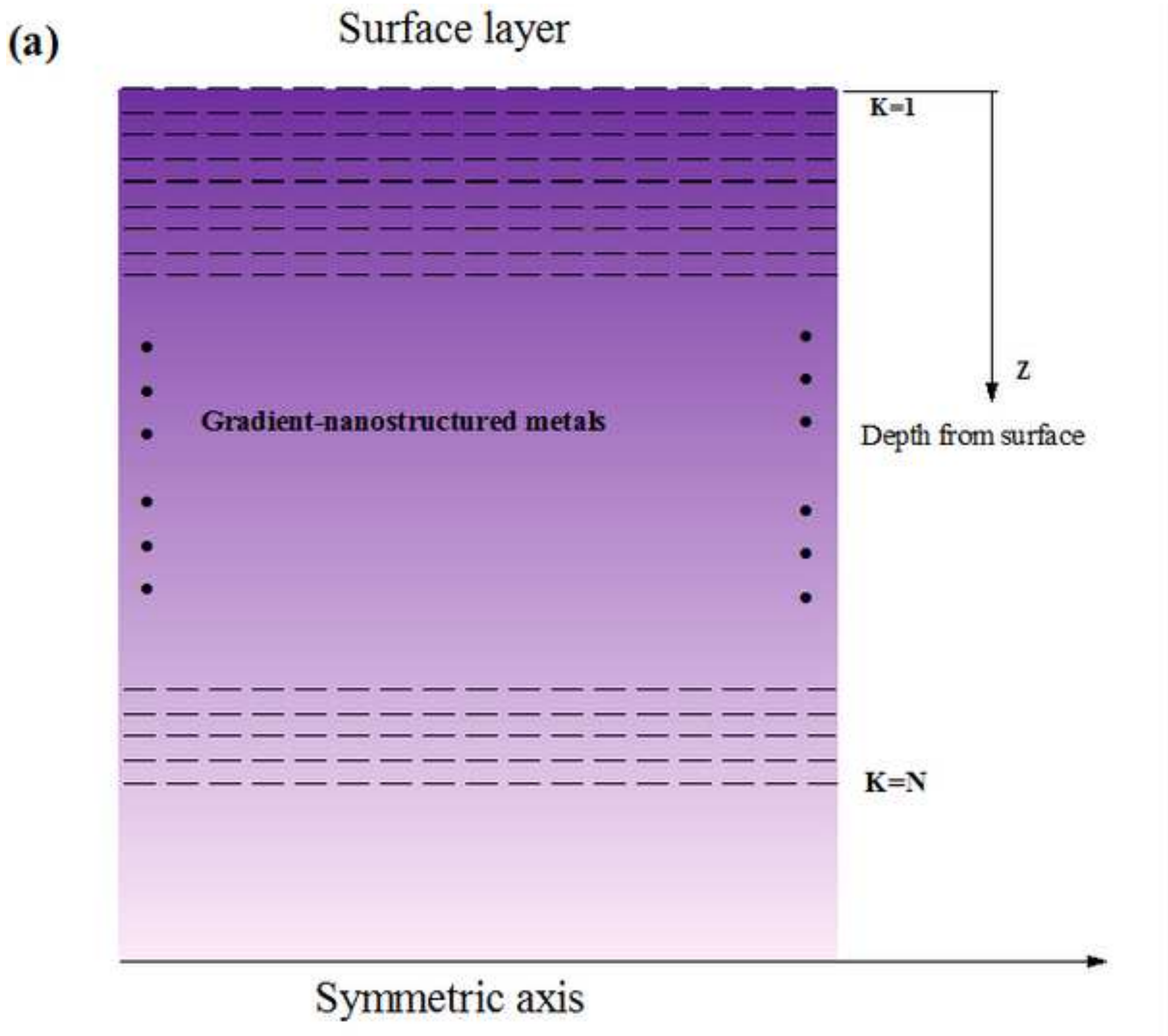

Figure1b
Click here to download high resolution image

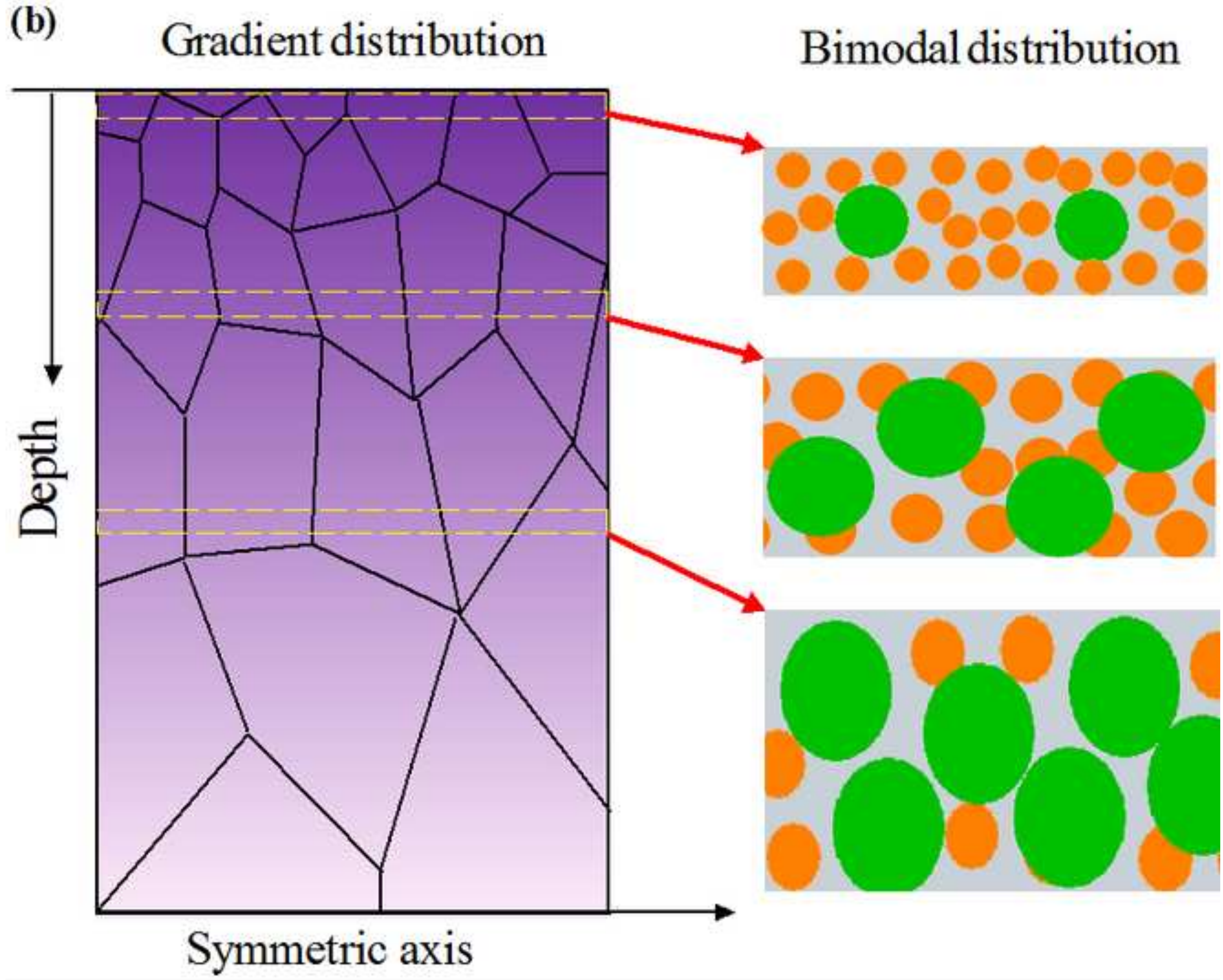

Figure1c
Click here to download high resolution image

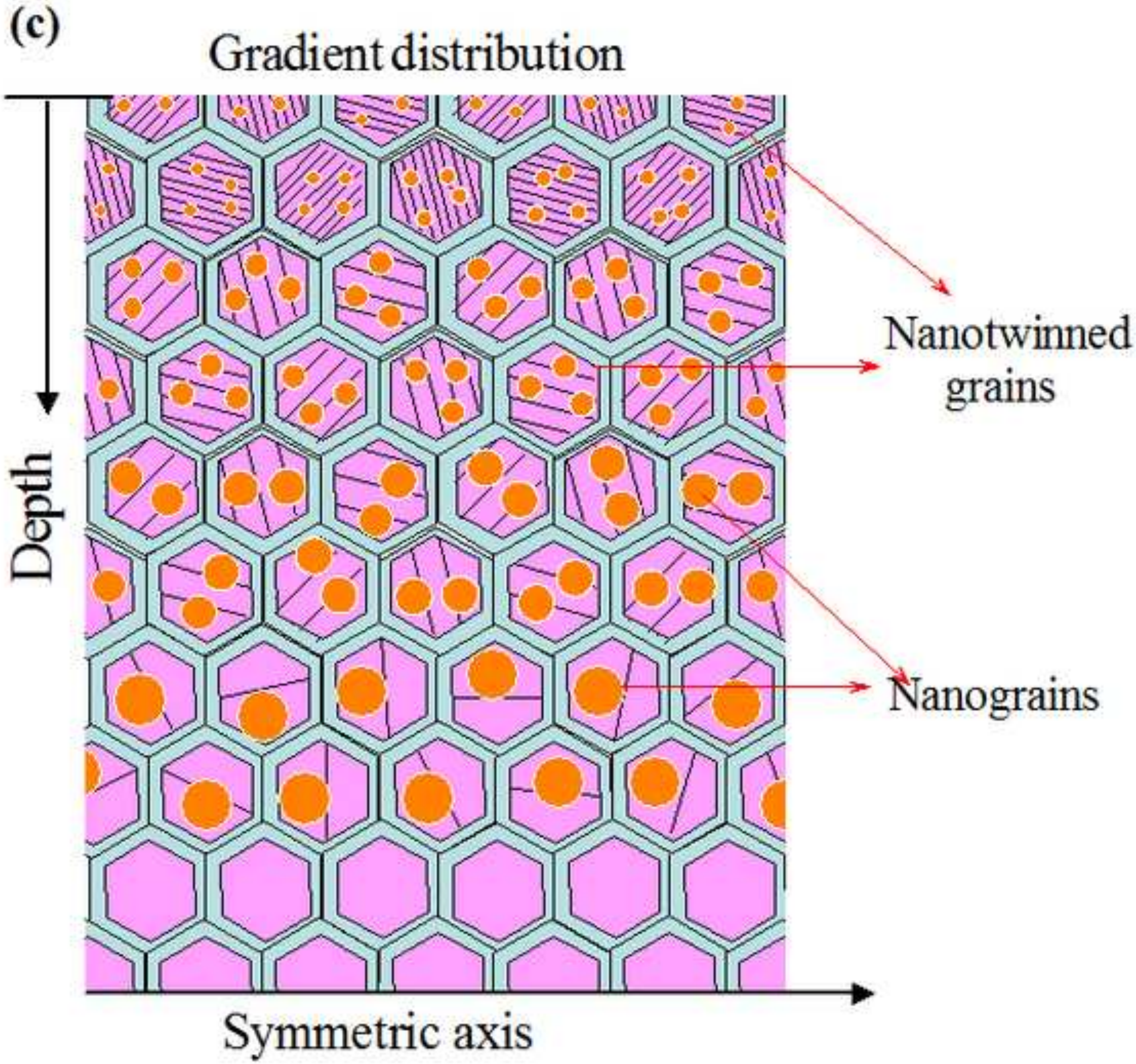

Figure1d

Click here to download high resolution image

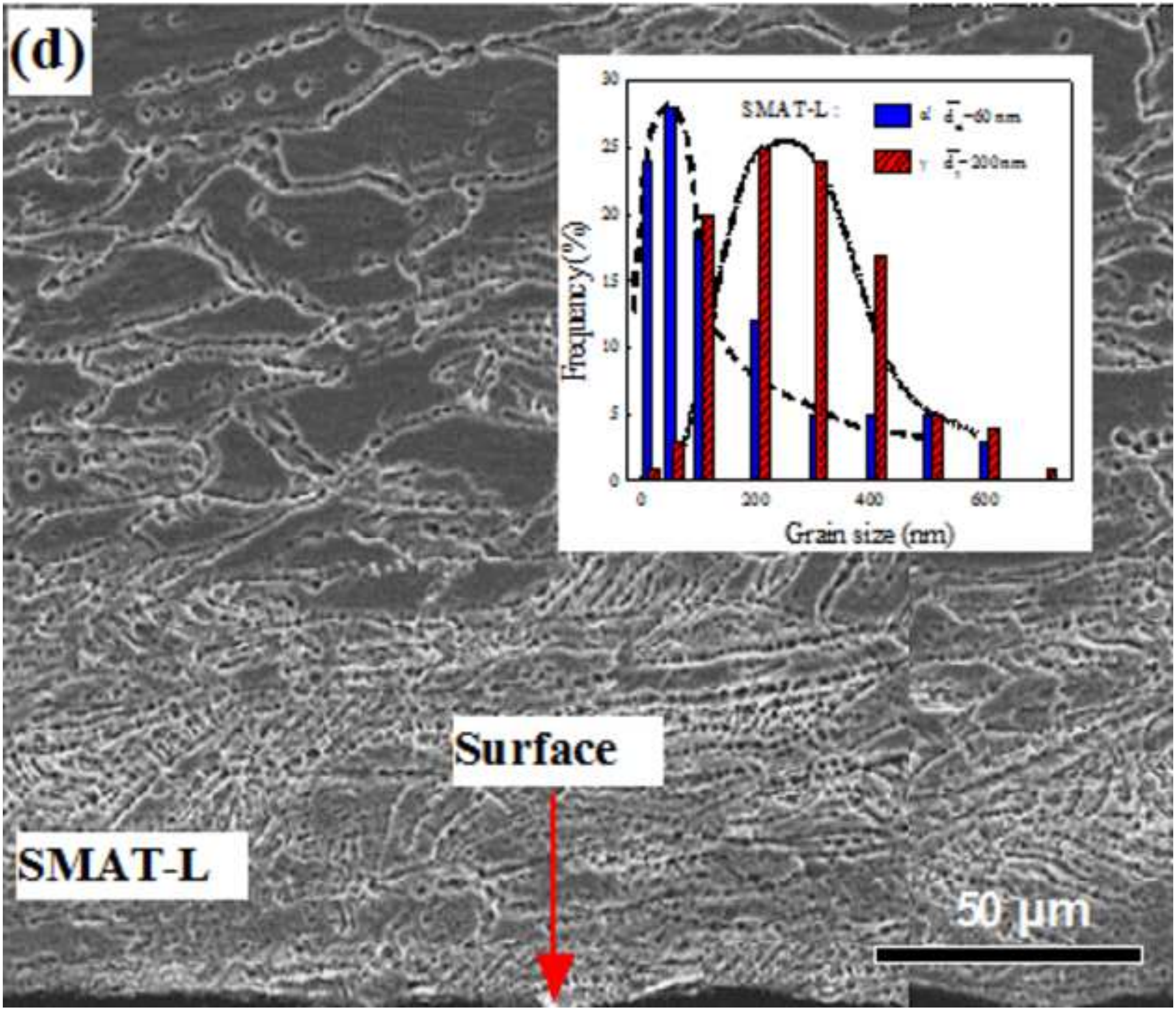

Figure1e

Click here to download high resolution image

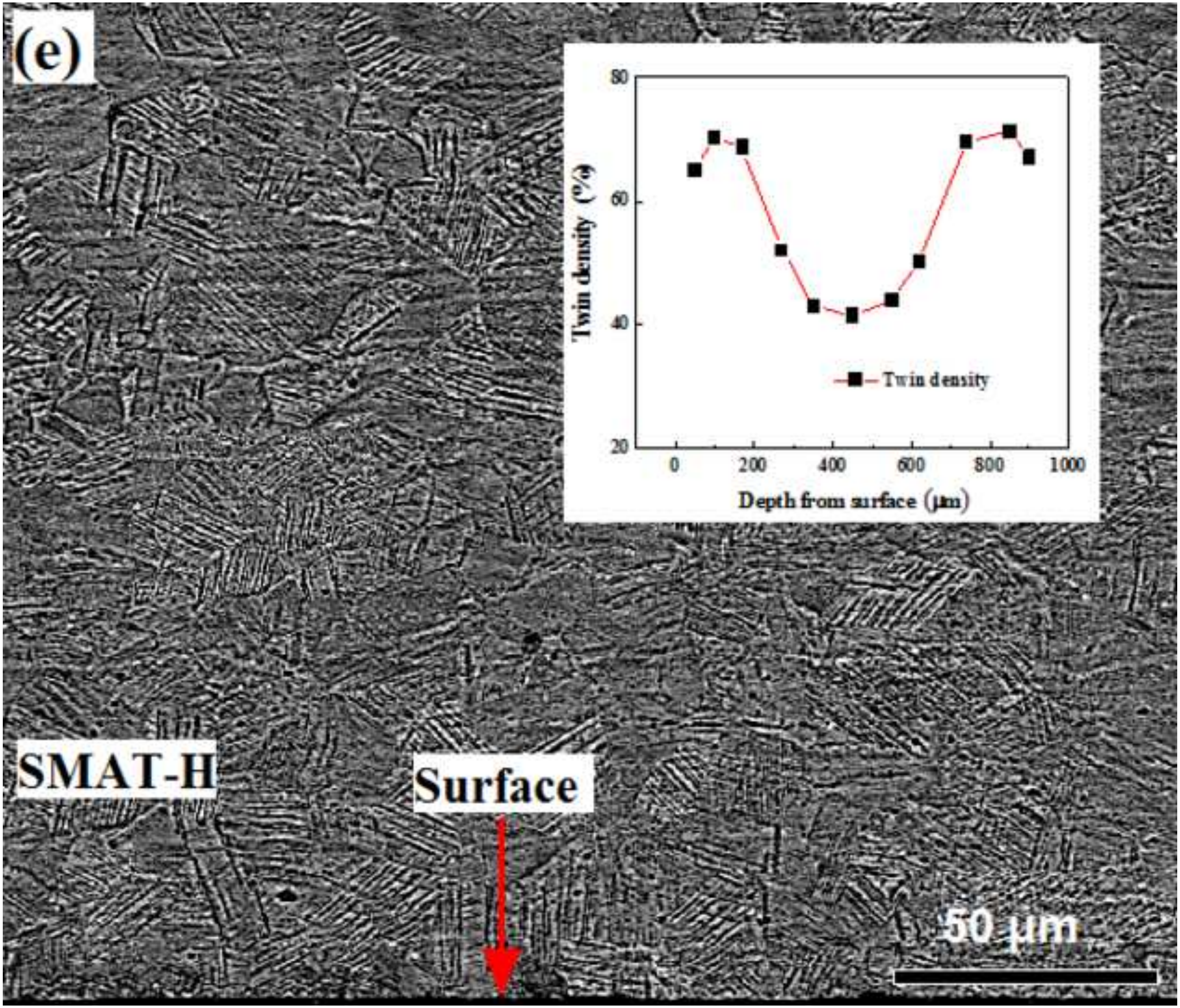

Figure2a
Click here to download high resolution image

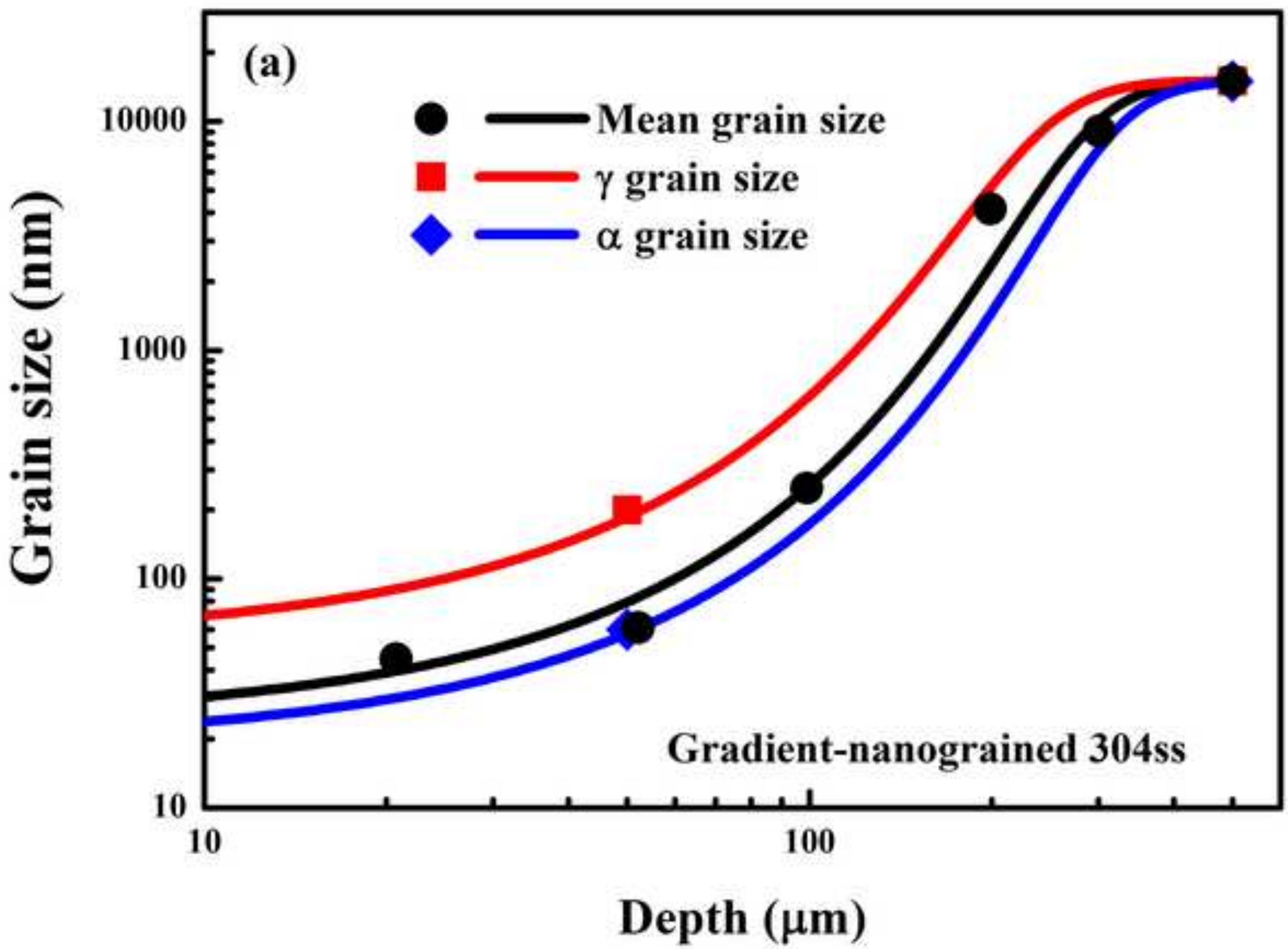

Figure2b
Click here to download high resolution image

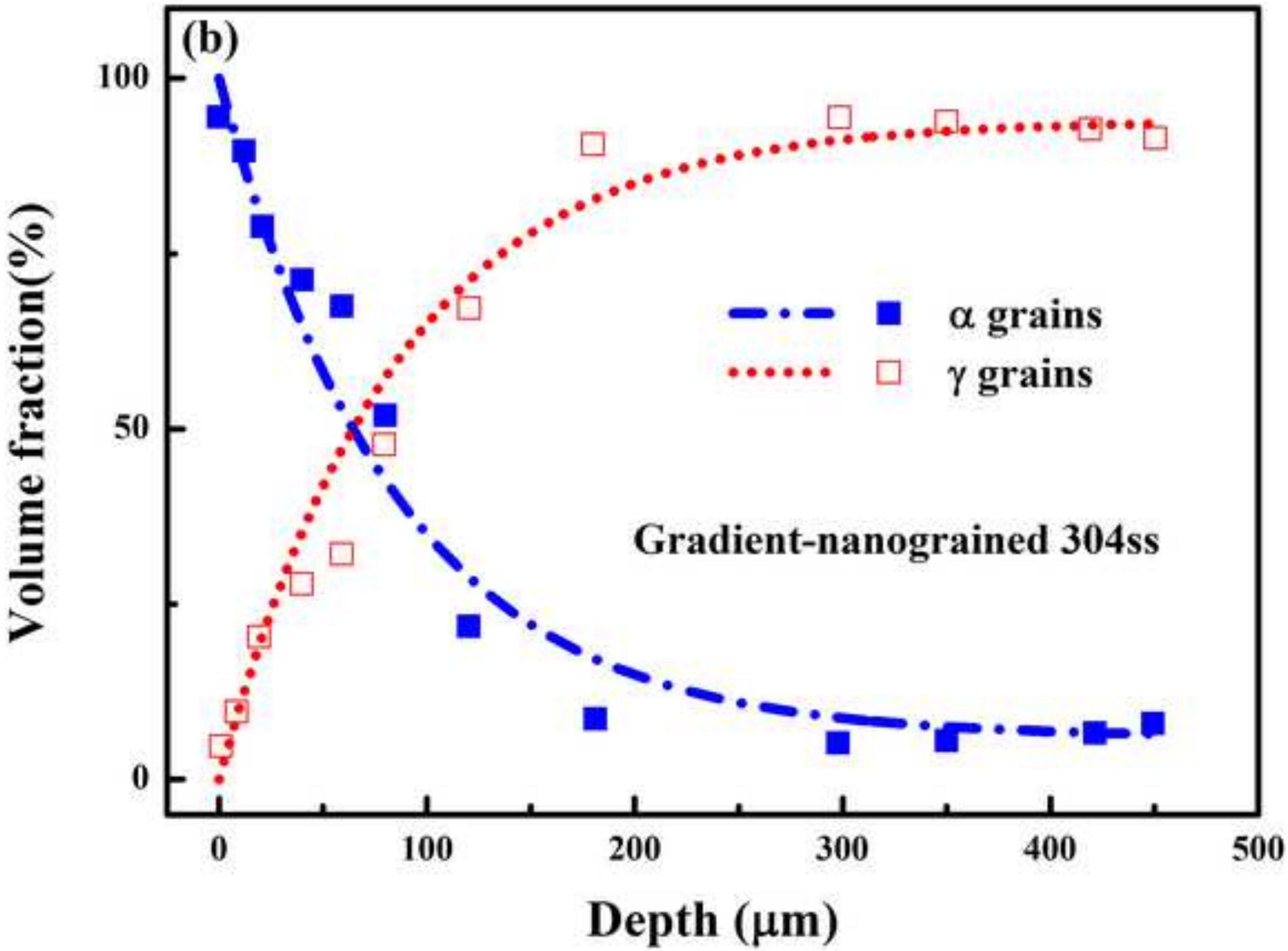

Figure3a

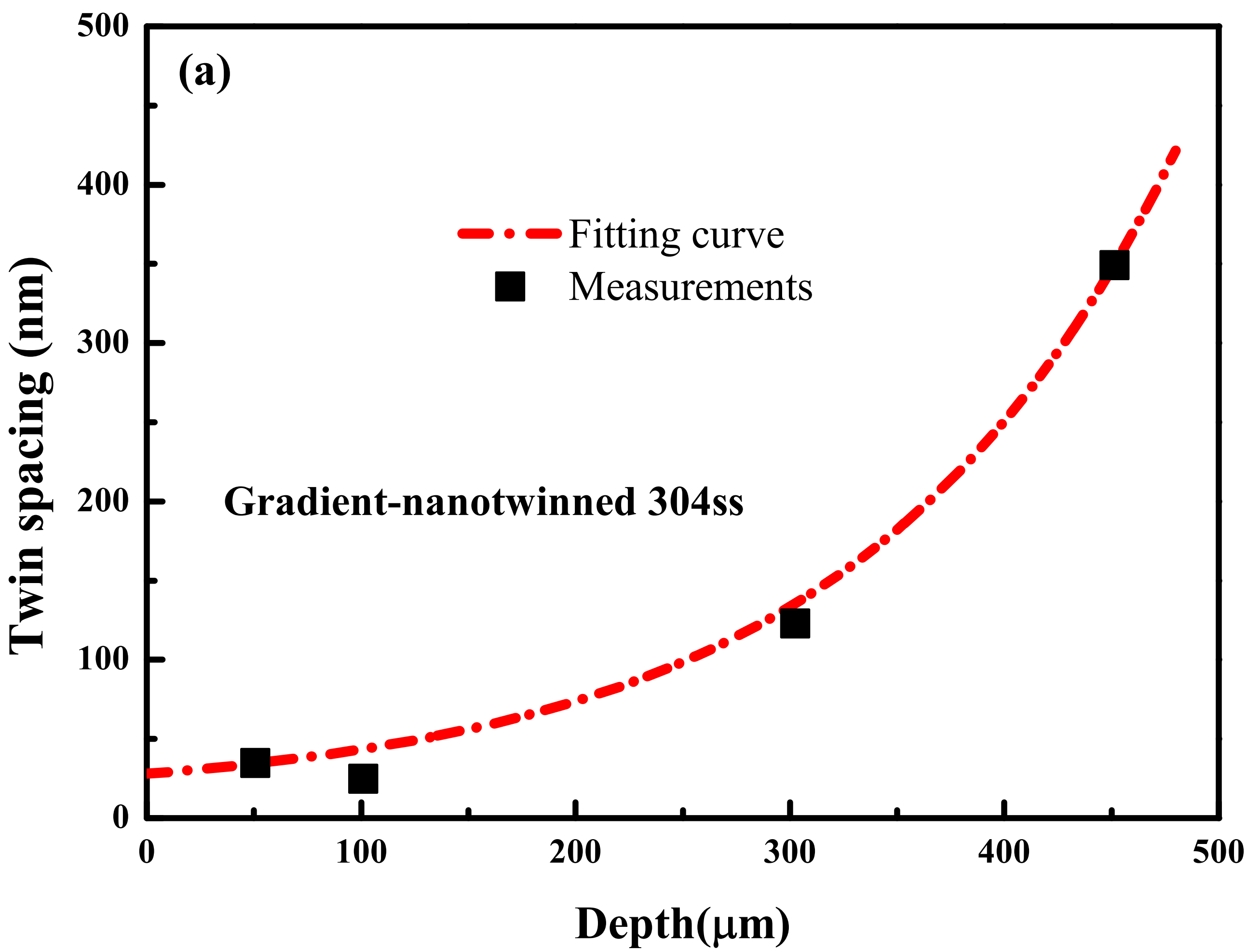

(a)
Fitting curve
Measurements
Gradient-nanotwinned 304ss
Twin spacing (nm)
Depth(μm)
0
100
200
300
400
500

Figure3b

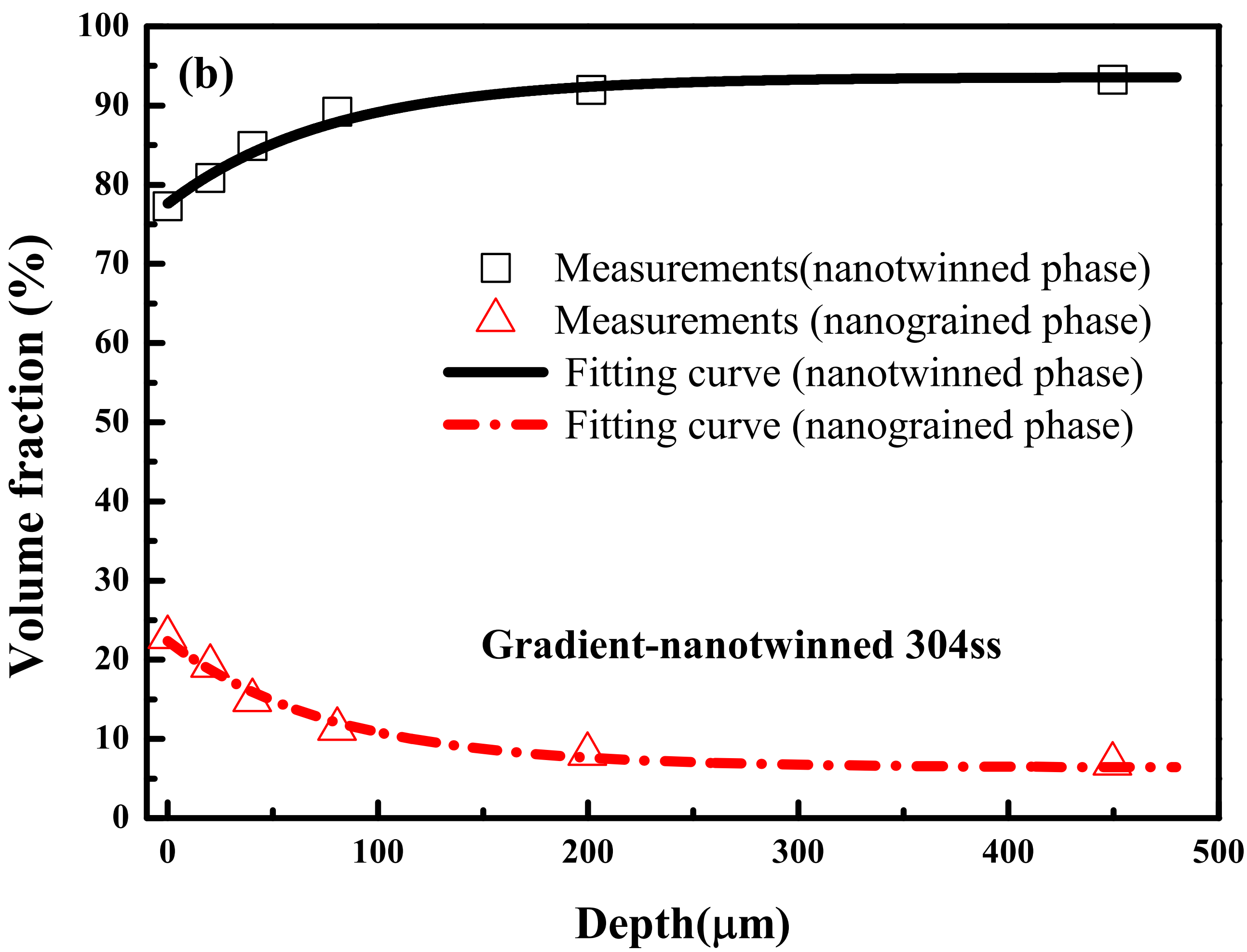
(b)
Measurements(nanotwinned phase)
Measurements (nanograined phase)
Fitting curve (nanotwinned phase)
Fitting curve (nanograined phase)
Gradient-nanotwinned 304ss
Volume fraction (%)
Depth(μm)
0
10
20
30
40
50
60
70
80
90
100
0
100
200
300
400
500

Figure4a

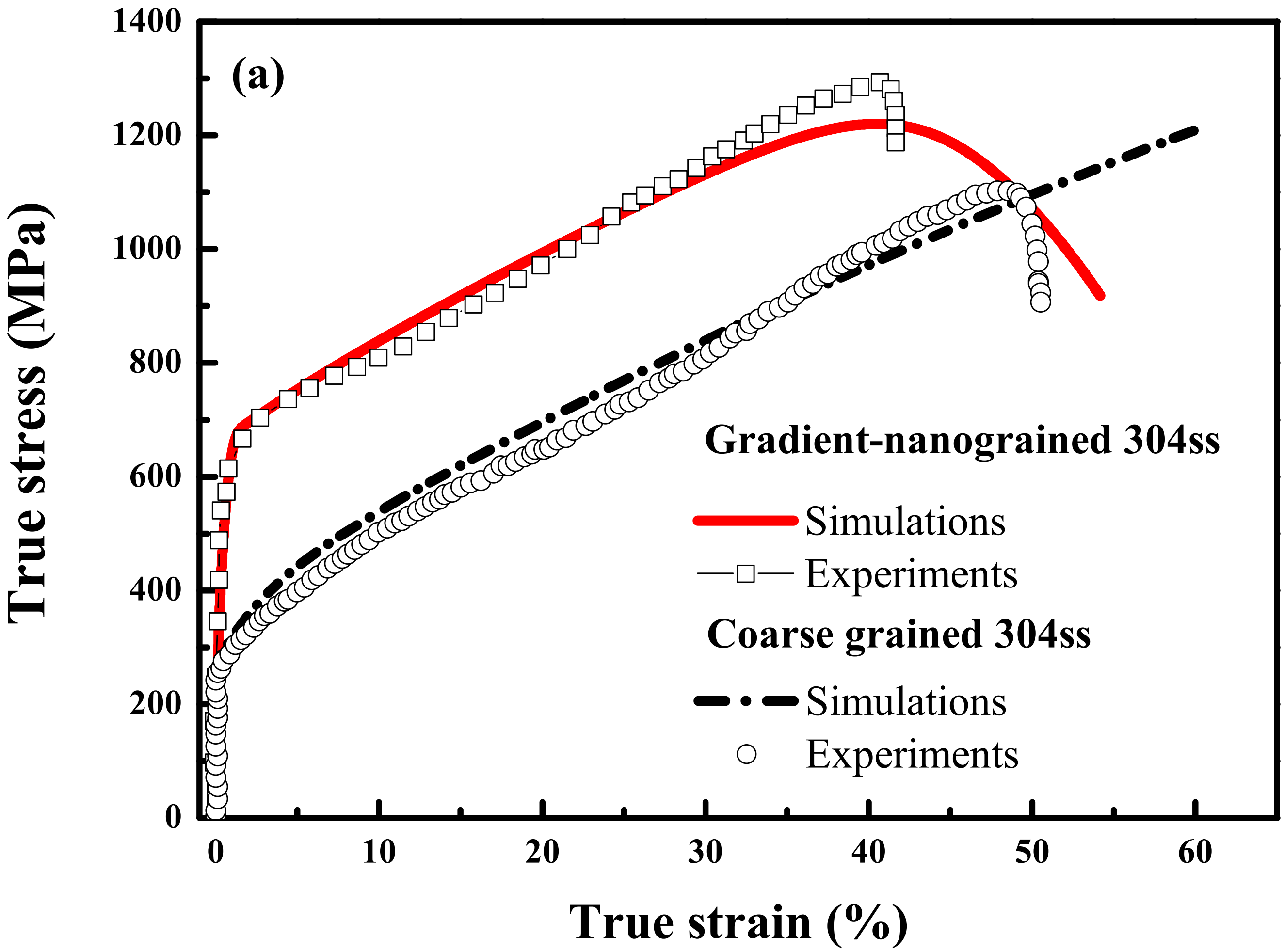
(a)
1400
1200
1000
800
600
400
200
0
0
10
20
30
40
50
60
True stress (MPa)
True strain (%)
Gradient-nanograined 304ss
Simulations
Experiments
Coarse grained 304ss
Simulations
Experiments

Figure4b

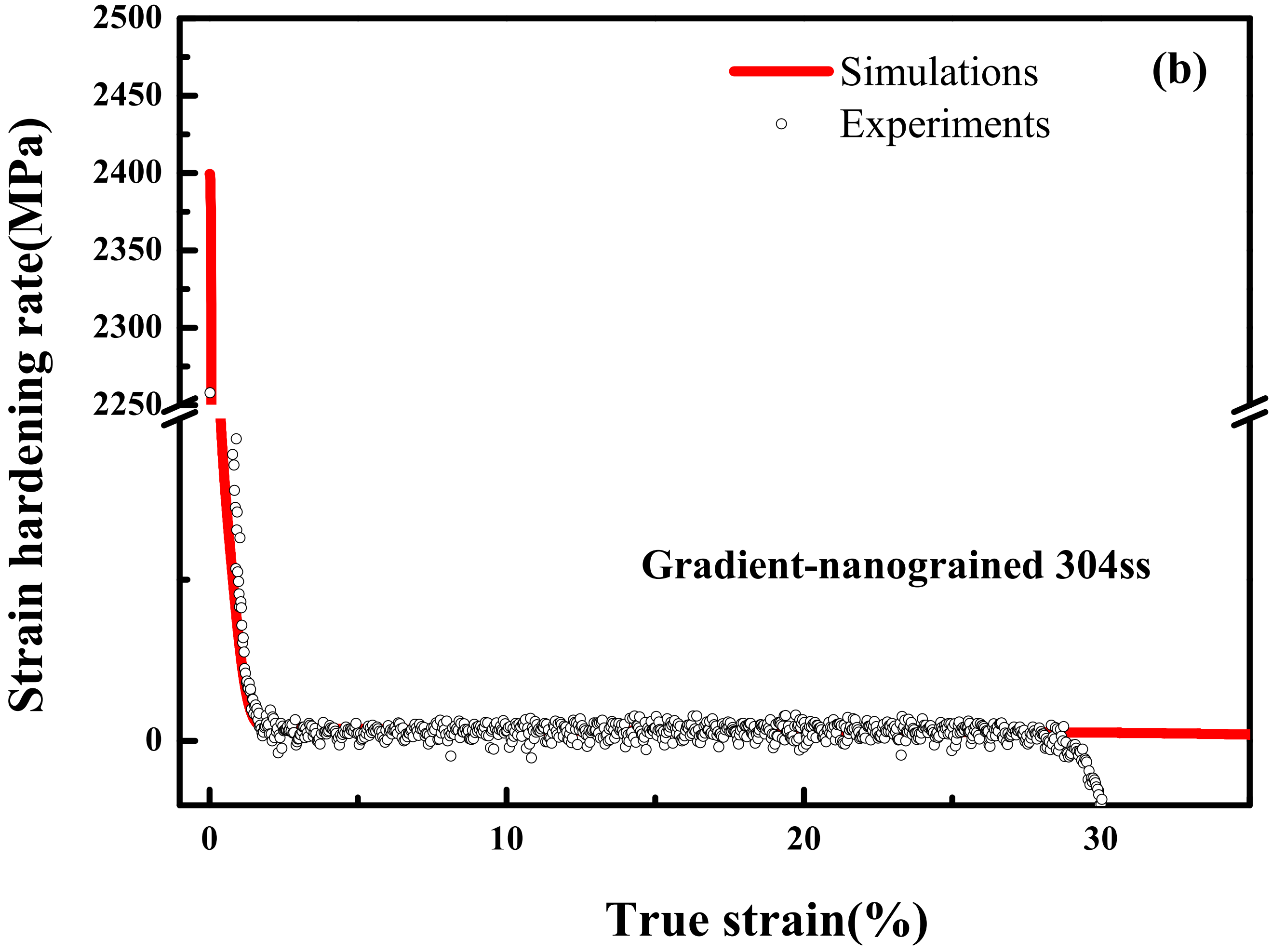

Simulations
Experiments
(b)
Gradient-nanograined 304ss
Strain hardening rate(MPa)
True strain(%)
2500
2450
2400
2350
2300
2250
0
0
10
20
30

Figure5a

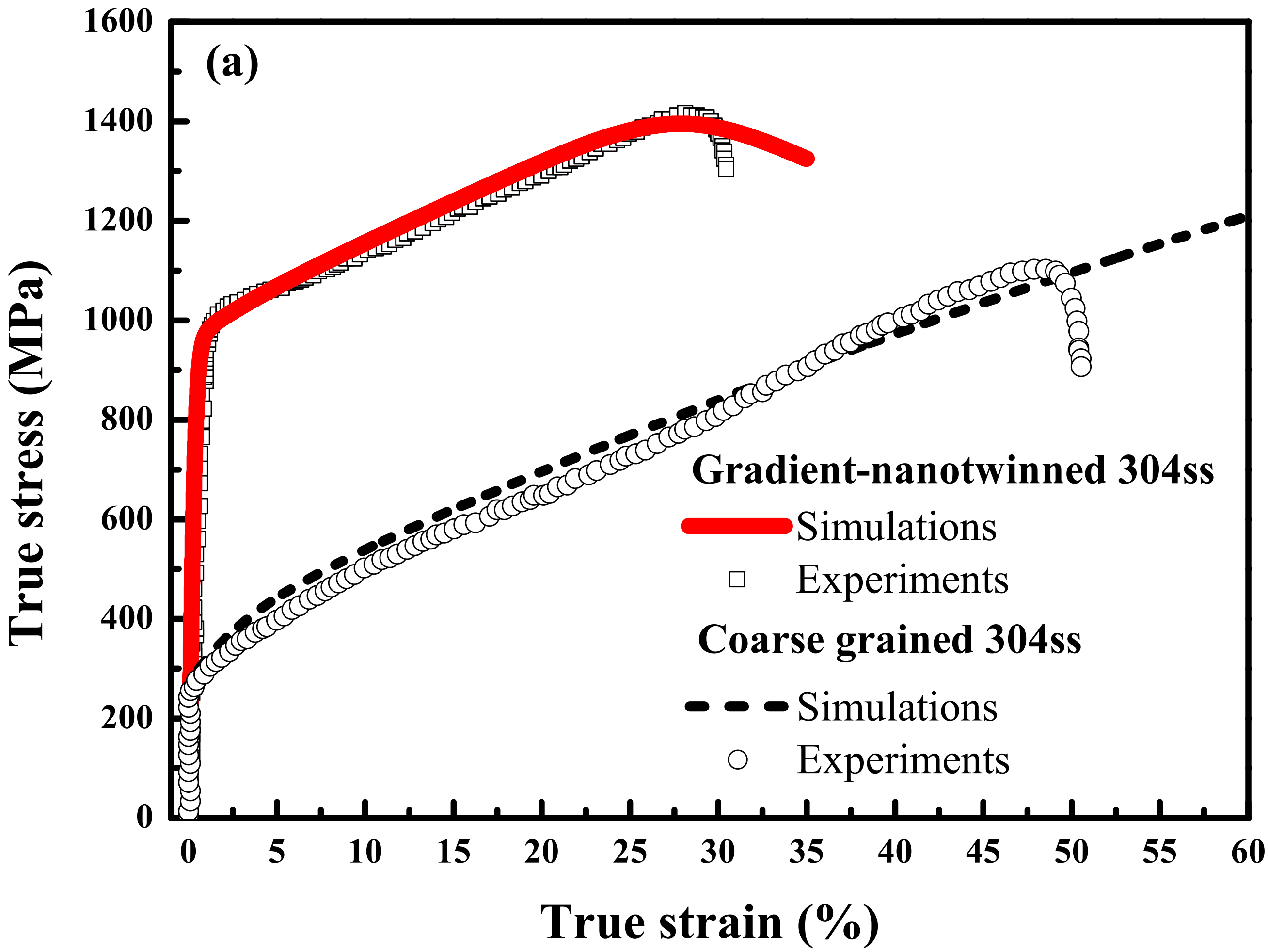

(a)
True stress (MPa)
True strain (%)
0
200
400
600
800
1000
1200
1400
1600
0
5
10
15
20
25
30
35
40
45
50
55
60
Gradient-nanotwinned 304ss
Simulations
Experiments
Coarse grained 304ss
Simulations
Experiments

Figure5b

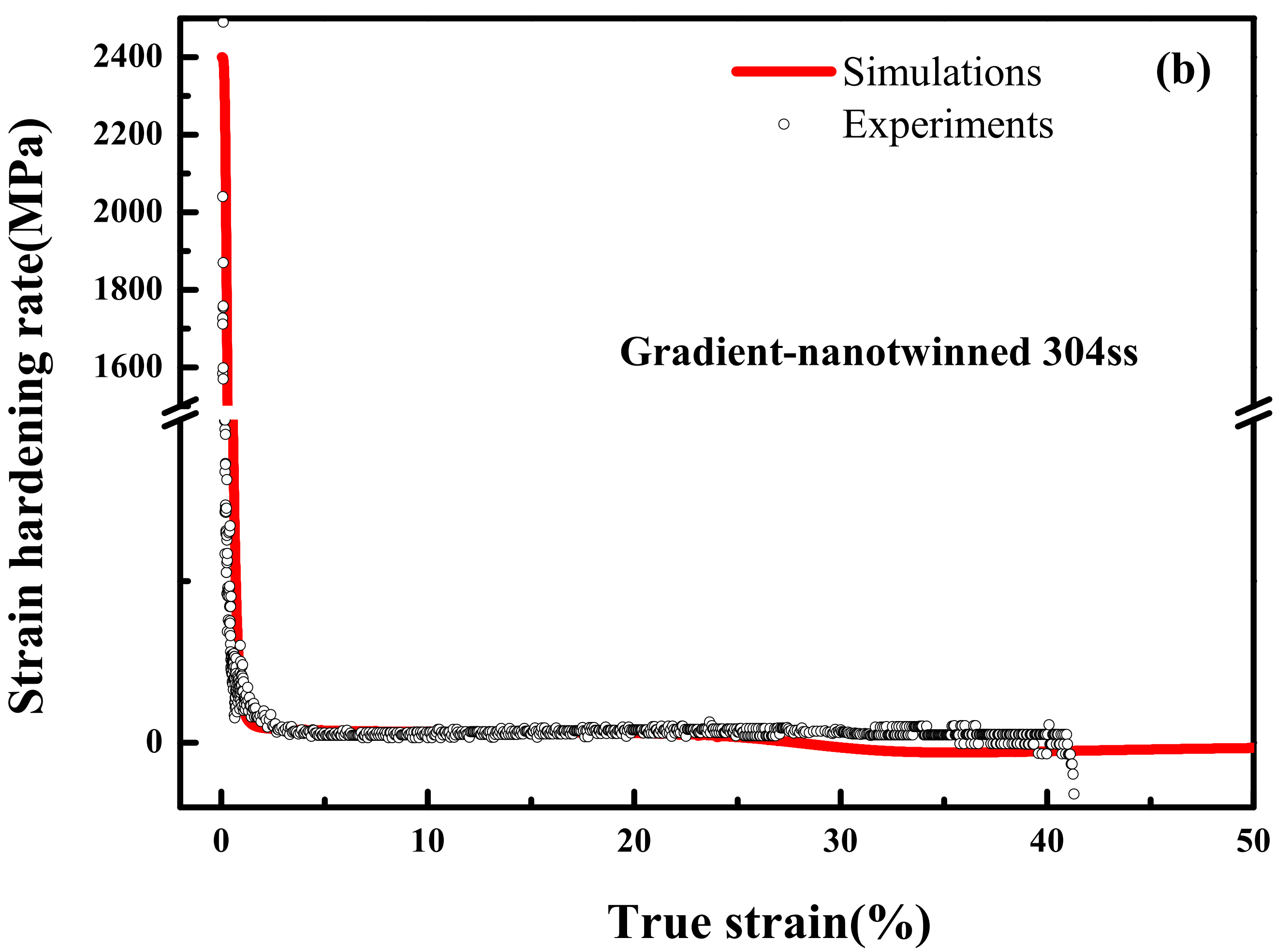

Strain hardening rate(MPa)
2400
2200
2000
1800
1600
0
0
10
20
30
40
50
True strain(%)
Simulations
Experiments
(b)
Gradient-nanotwinned 304ss

Figure5c
Click here to download high resolution image

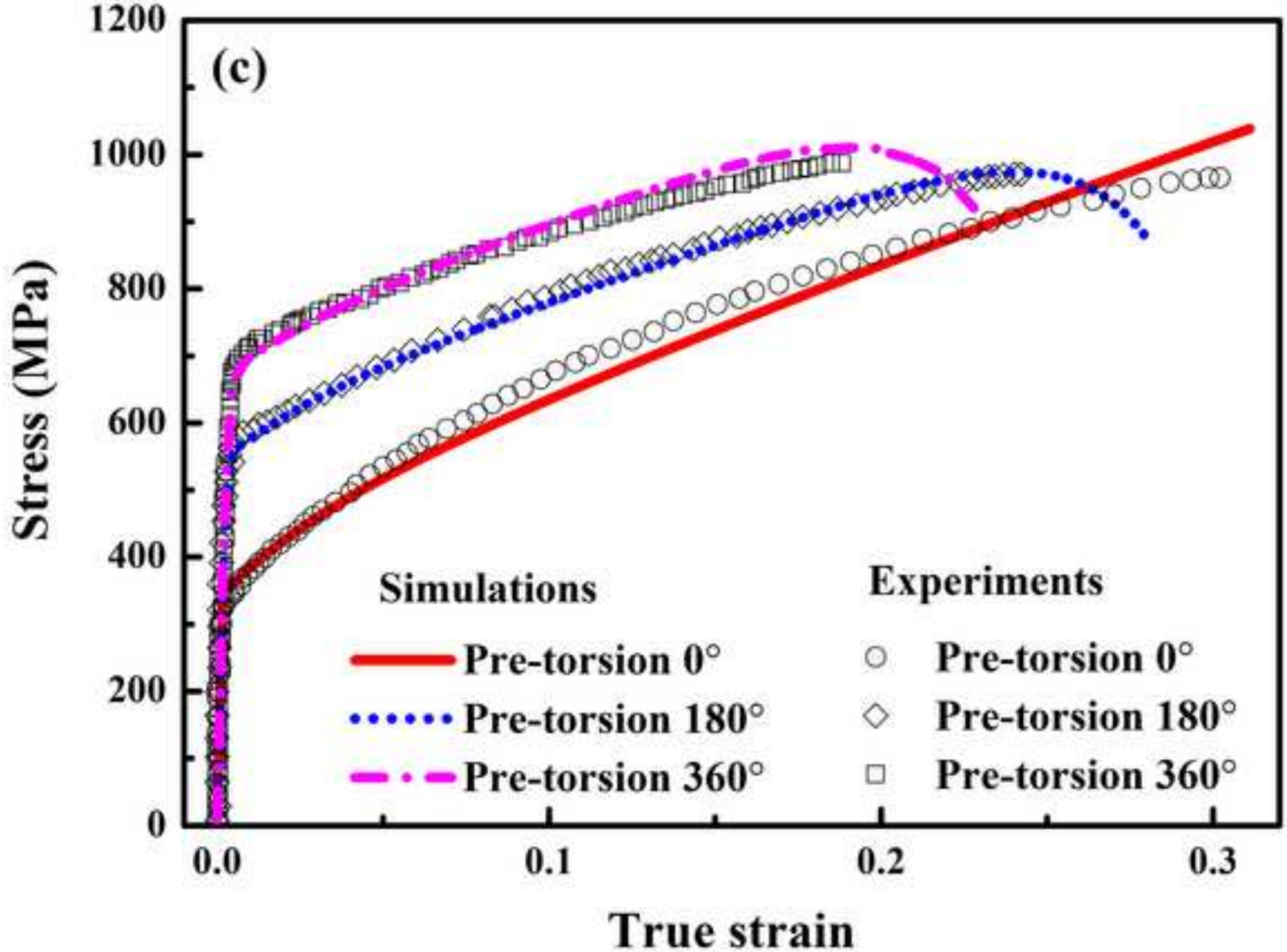

Figure6a
Click here to download high resolution image

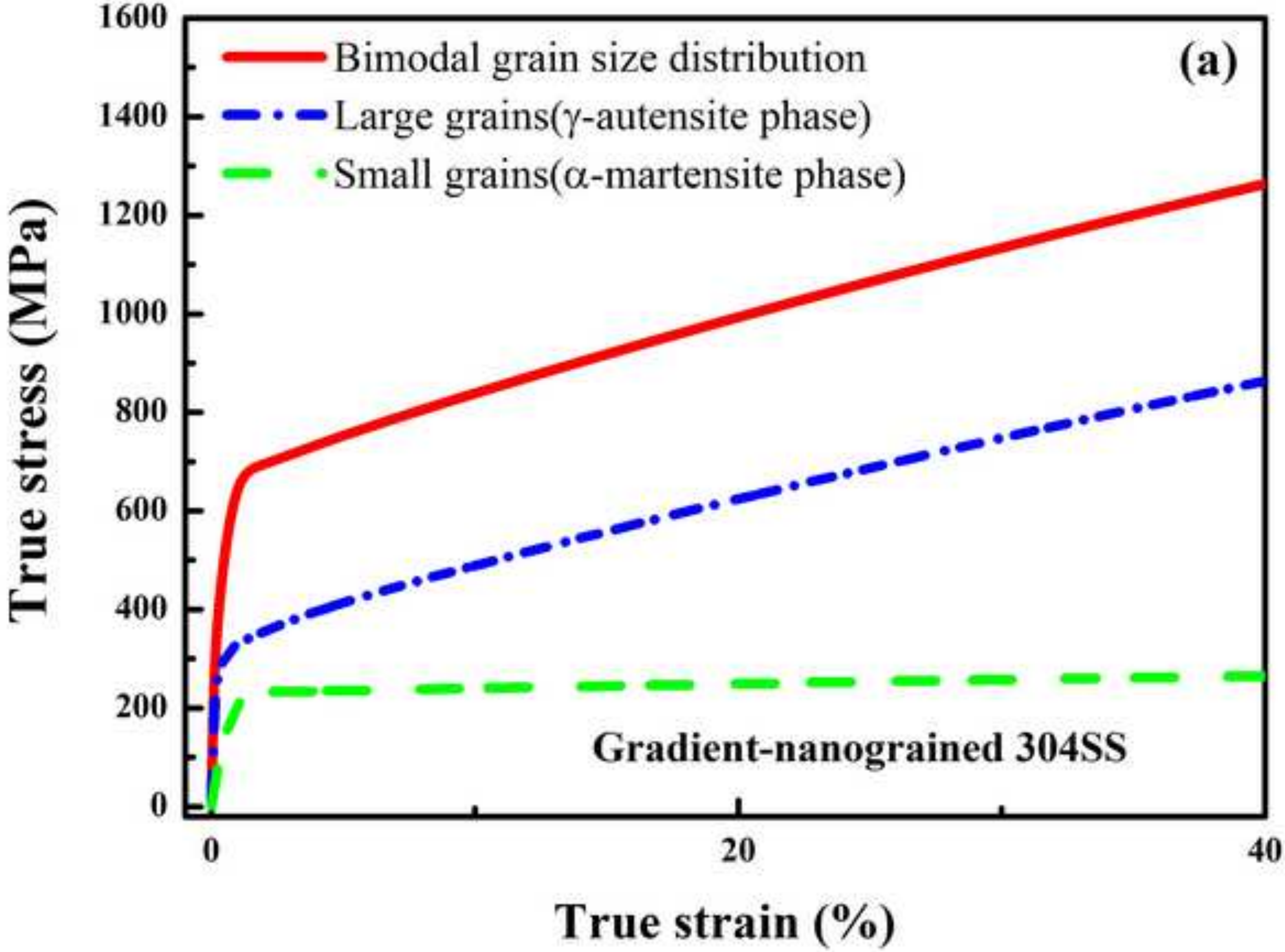

Figure6b

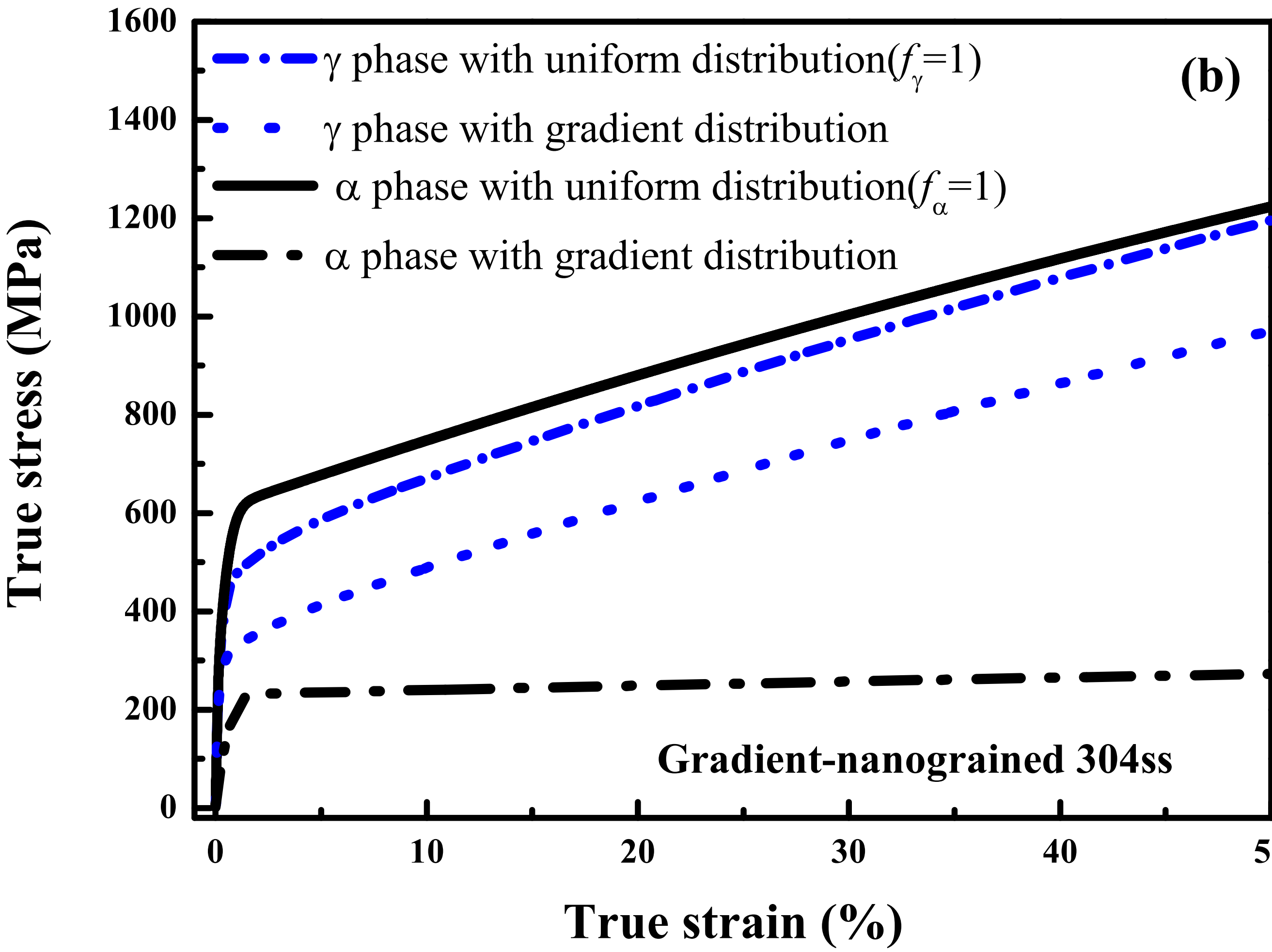

1600
1400
1200
1000
800
600
400
200
0
True stress (MPa)
0
10
20
30
40
50
True strain (%)
γ phase with uniform distribution($f_γ$=1)
γ phase with gradient distribution
α phase with uniform distribution($f_α$=1)
α phase with gradient distribution
(b)
Gradient-nanograined 304ss

Figure7a

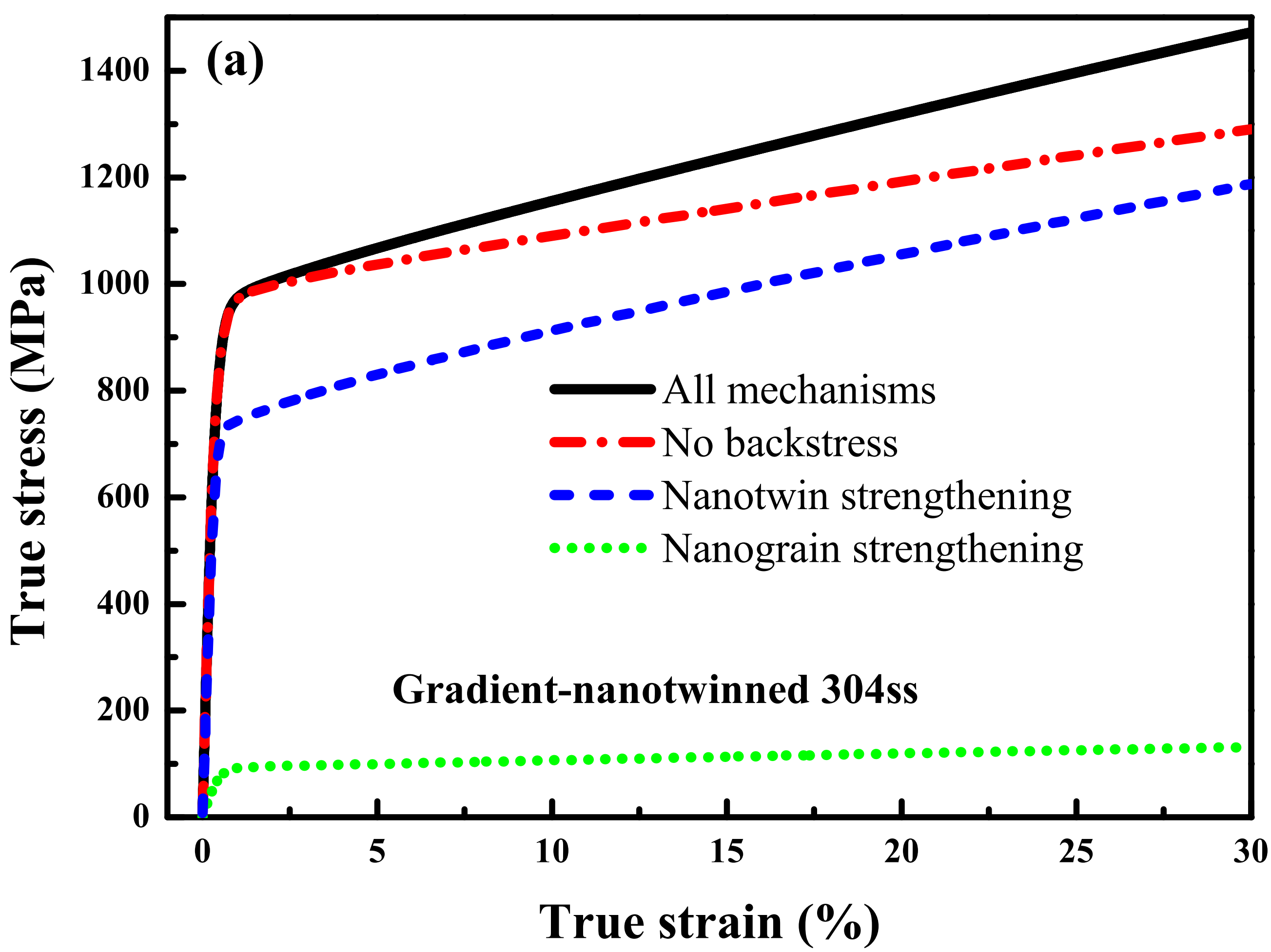
(a)
True stress (MPa)
True strain (%)
All mechanisms
No backstress
Nanotwin strengthening
Nanograin strengthening
Gradient-nanotwinned 304ss
0
200
400
600
800
1000
1200
1400
0
5
10
15
20
25
30

Figure7b

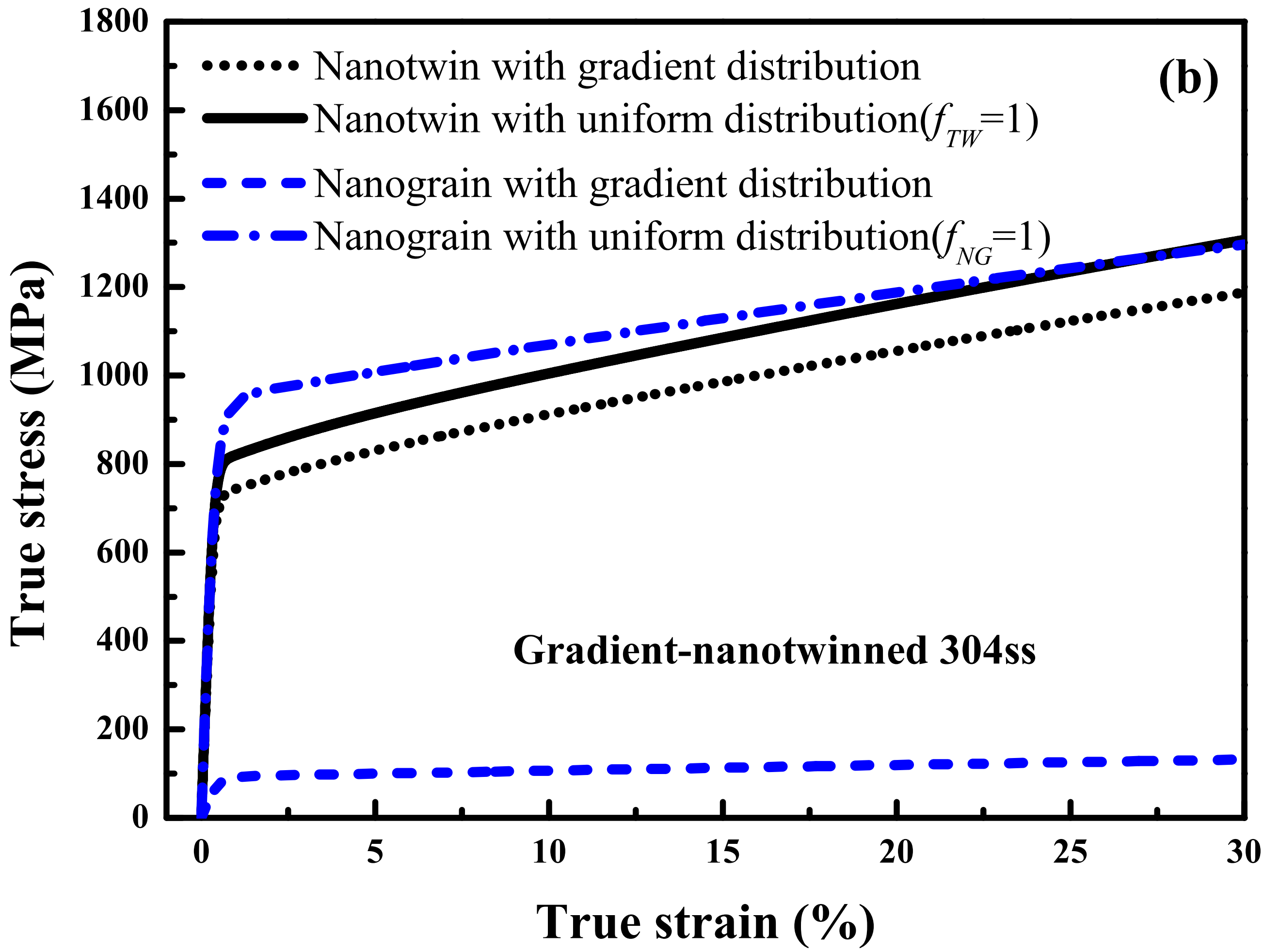

1800
1600
1400
1200
1000
800
600
400
200
0
0
5
10
15
20
25
30
True stress (MPa)
True strain (%)
Nanotwin with gradient distribution
Nanotwin with uniform distribution(f_{TW}=1)
Nanograin with gradient distribution
Nanograin with uniform distribution(f_{NG}=1)
(b)
Gradient-nanotwinned 304ss

Figure8a
Click here to download high resolution image

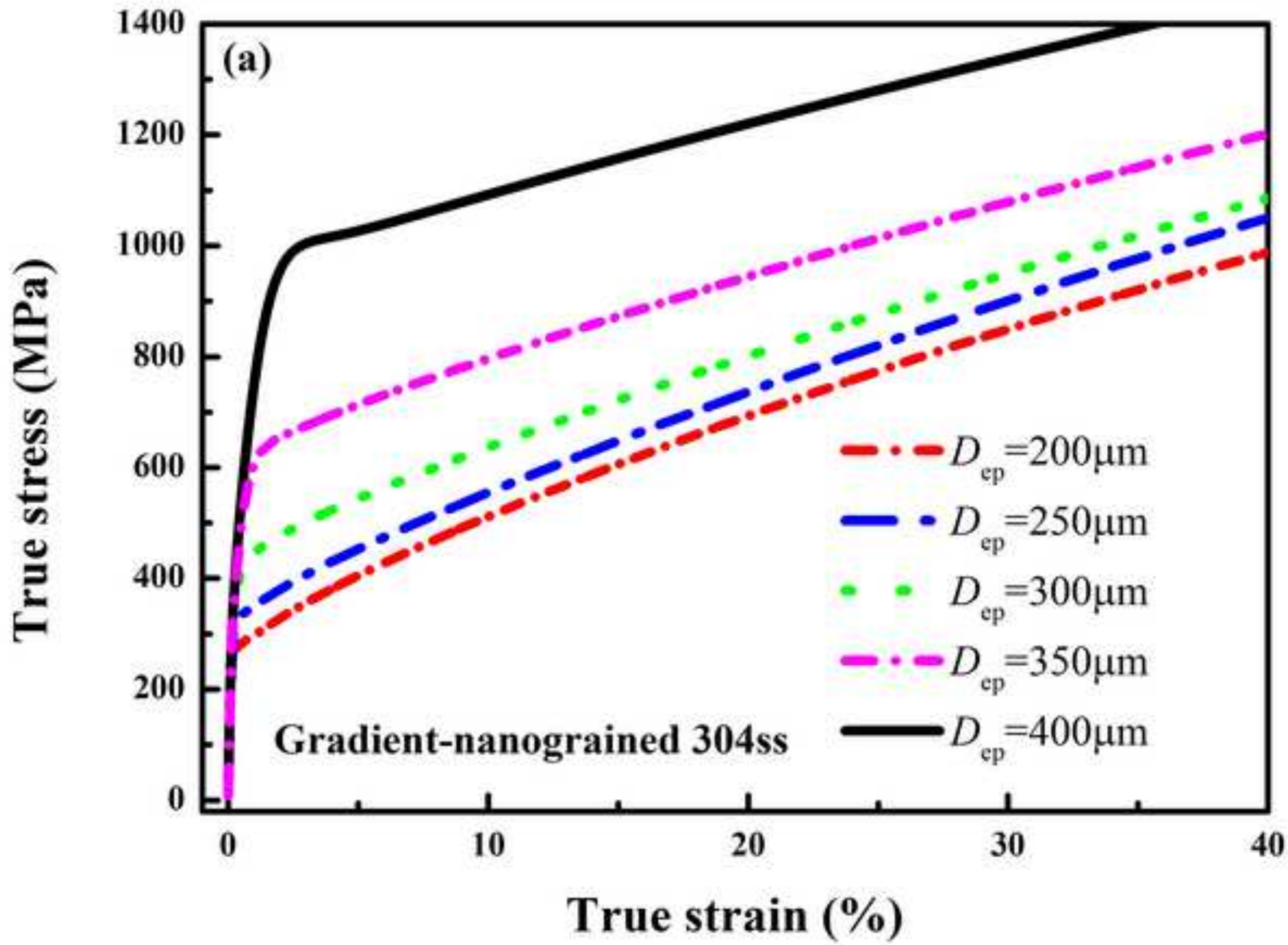

Figure8b
Click here to download high resolution image

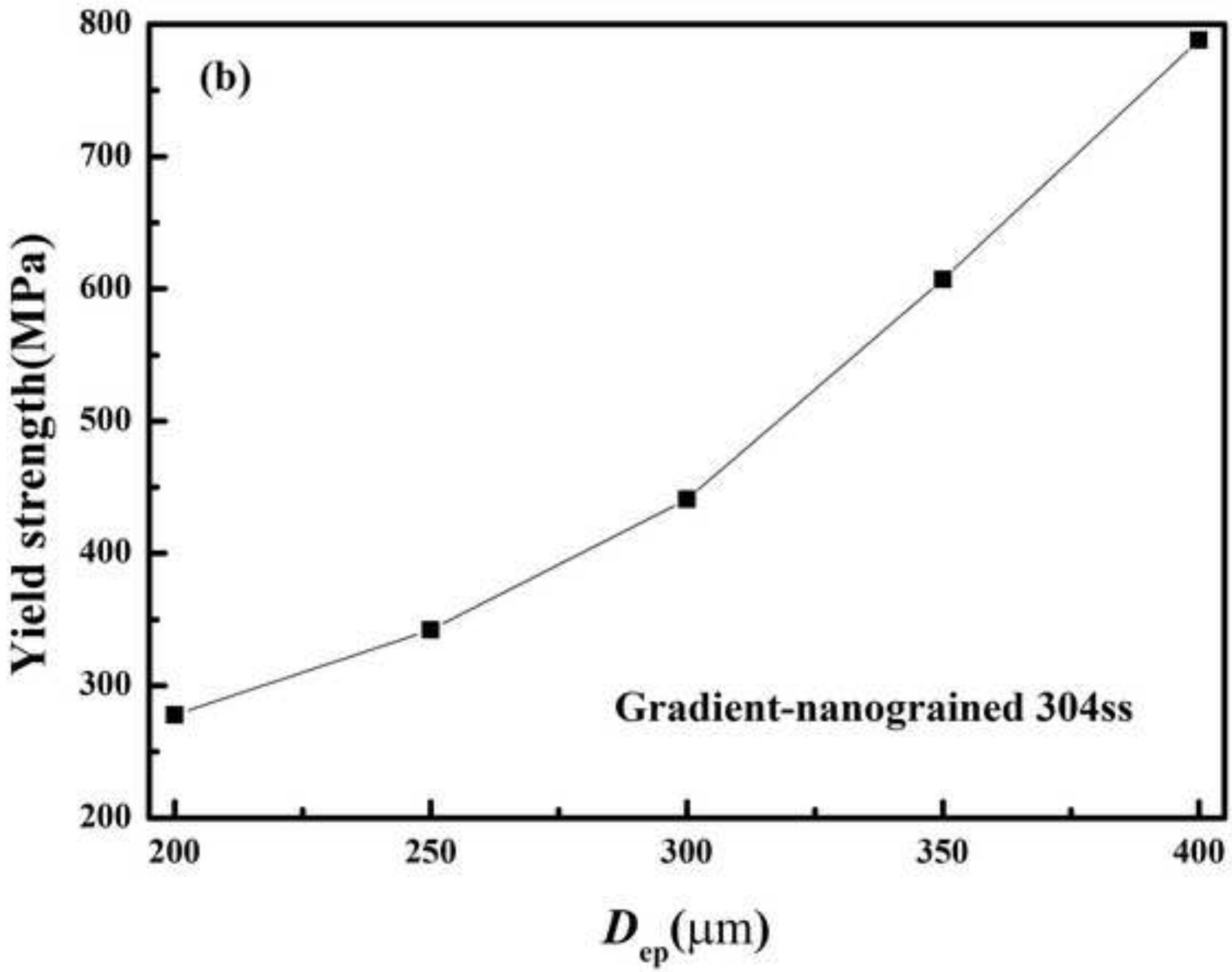

Figure8c
Click here to download high resolution image

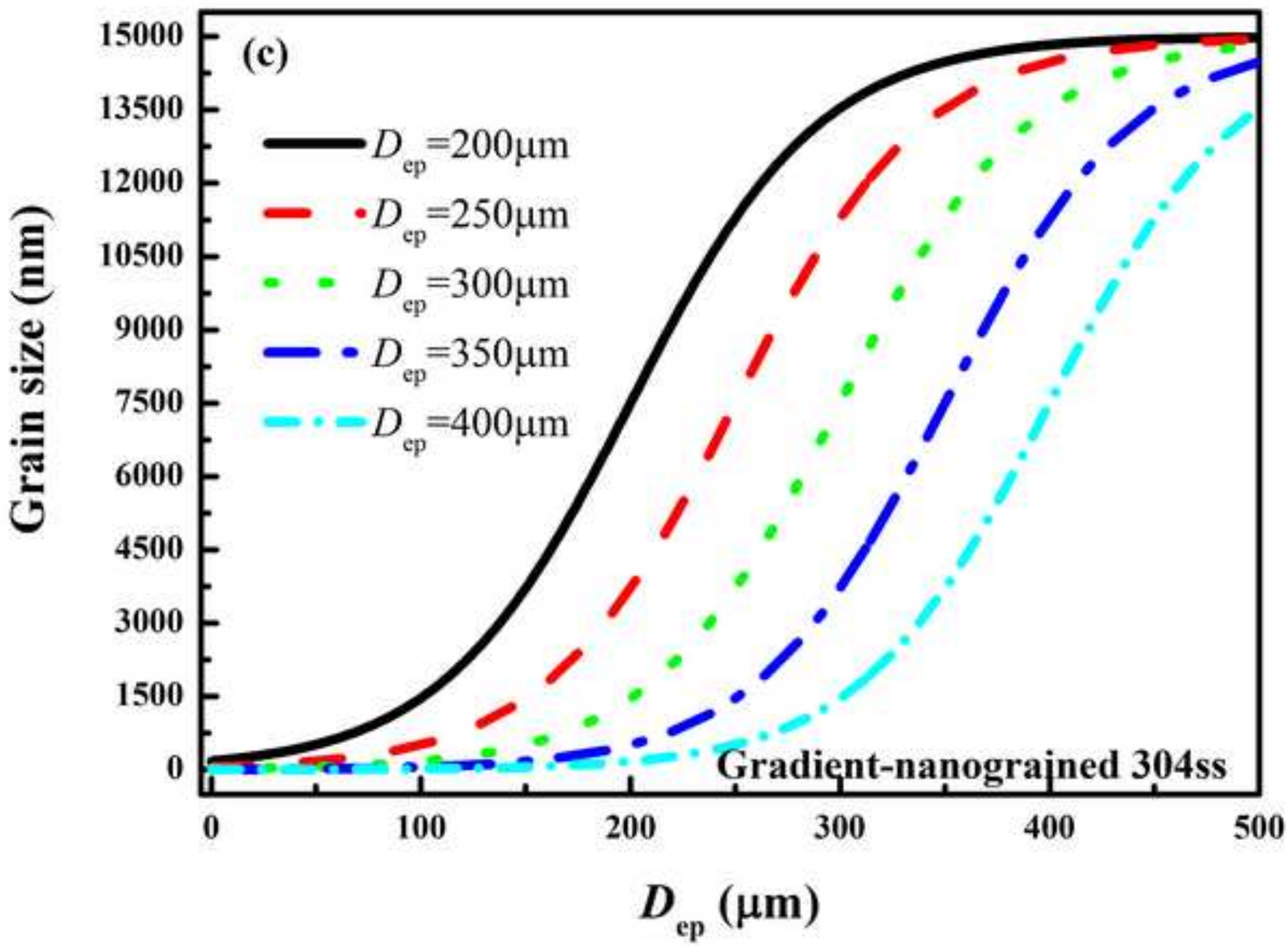

Figure8d

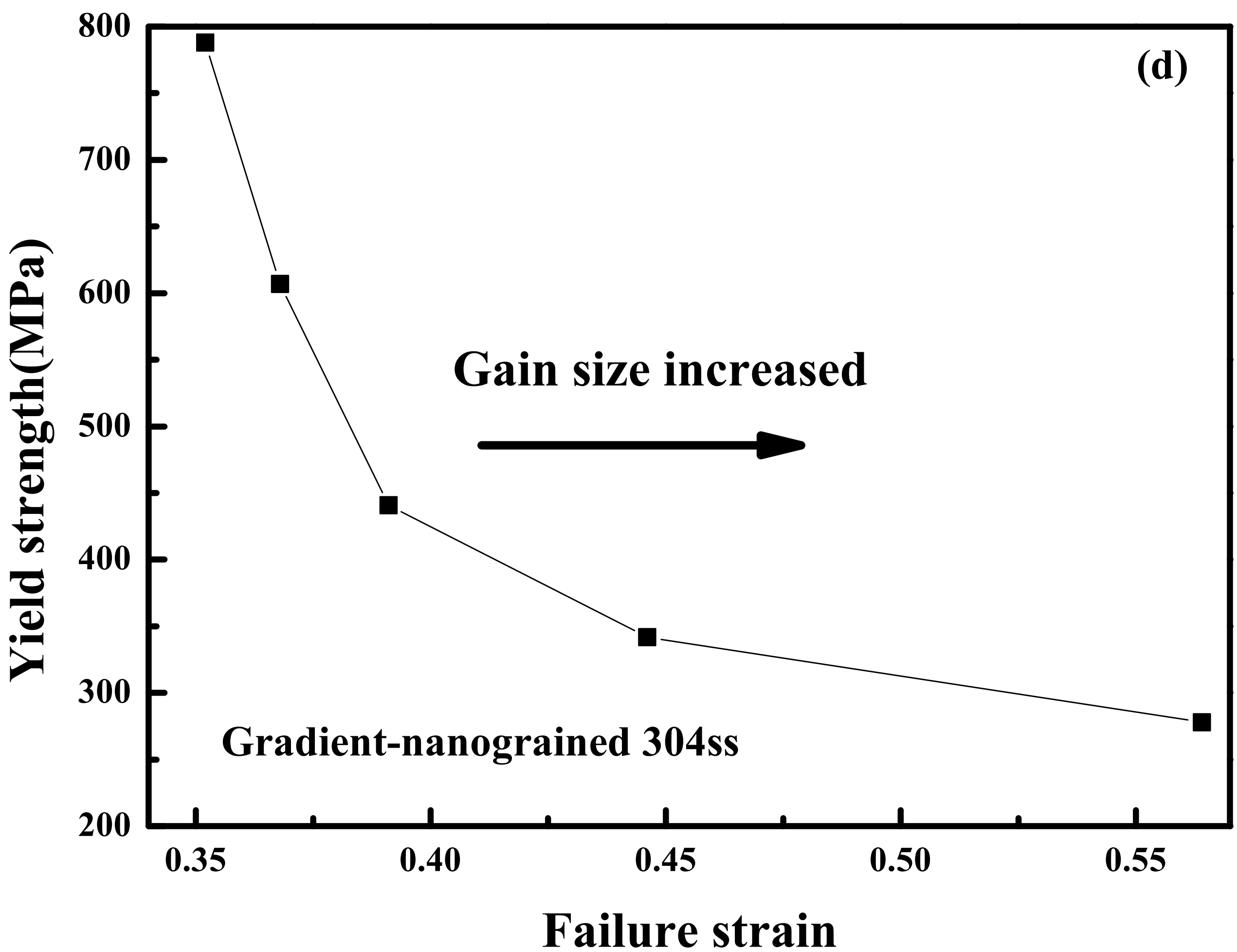

(d)
Gain size increased
Gradient-nanograined 304ss
Yield strength(MPa)
800
700
600
500
400
300
200
0.35
0.40
0.45
0.50
0.55
Failure strain

Figure9a

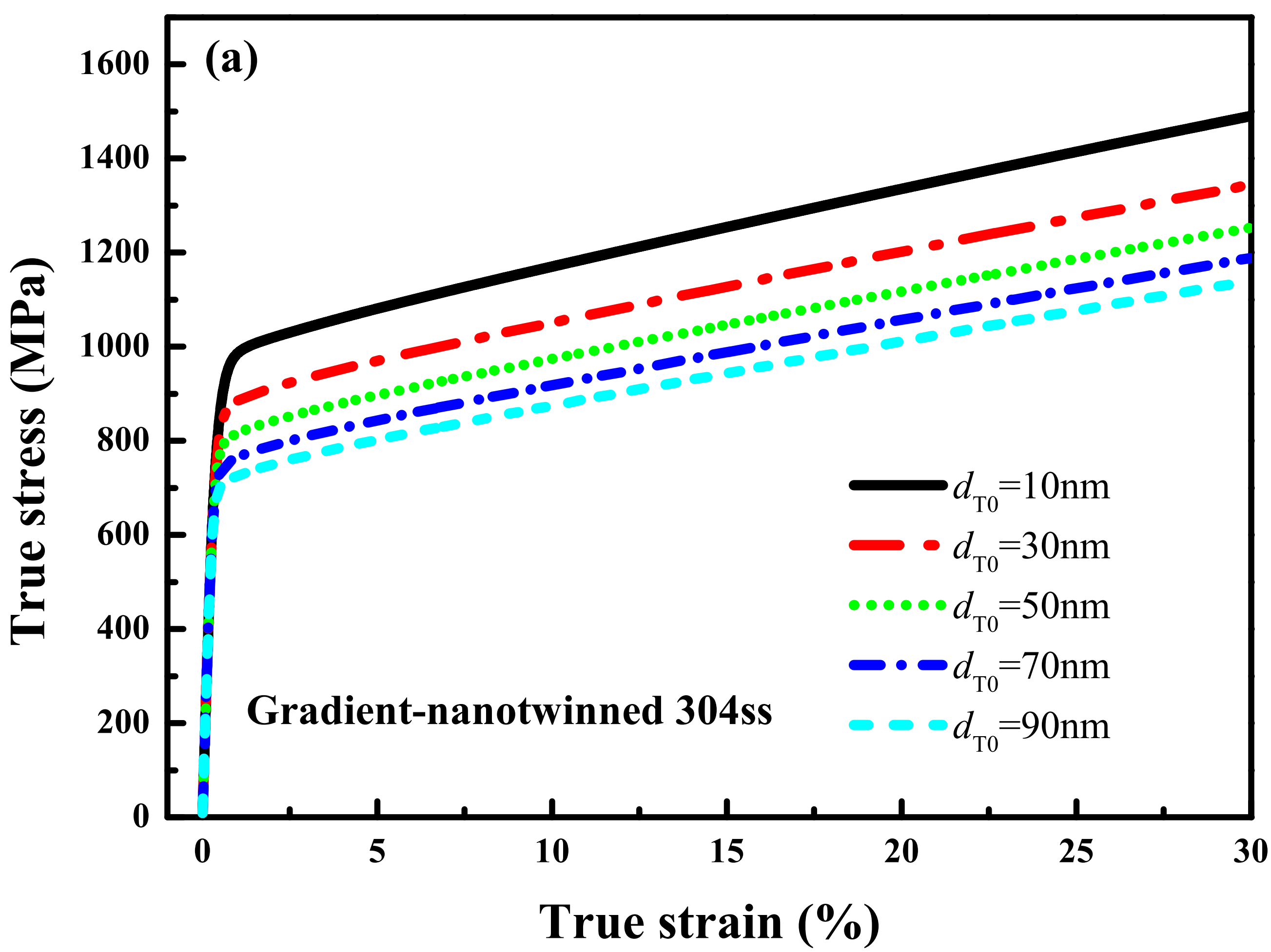
(a)
1600
1400
1200
1000
800
600
400
200
0
True stress (MPa)
0
5
10
15
20
25
30
True strain (%)
d_{T0}=10nm
d_{T0}=30nm
d_{T0}=50nm
d_{T0}=70nm
d_{T0}=90nm
Gradient-nanotwinned 304ss

Figure9b

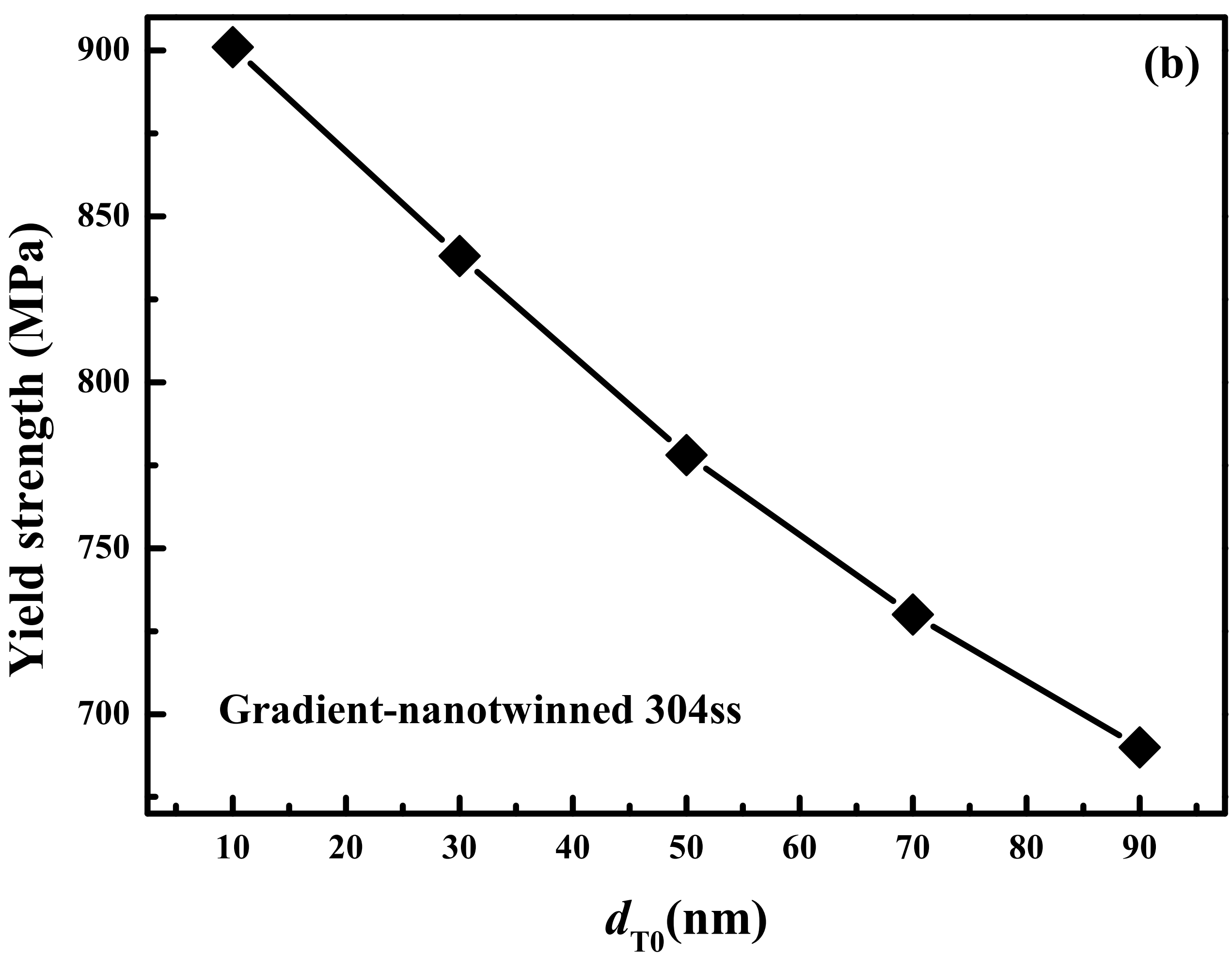

(b)
Gradient-nanotwinned 304ss
900
850
800
750
700
Yield strength (MPa)
10
20
30
40
50
60
70
80
90
d_{T0}(nm)

Figure9c

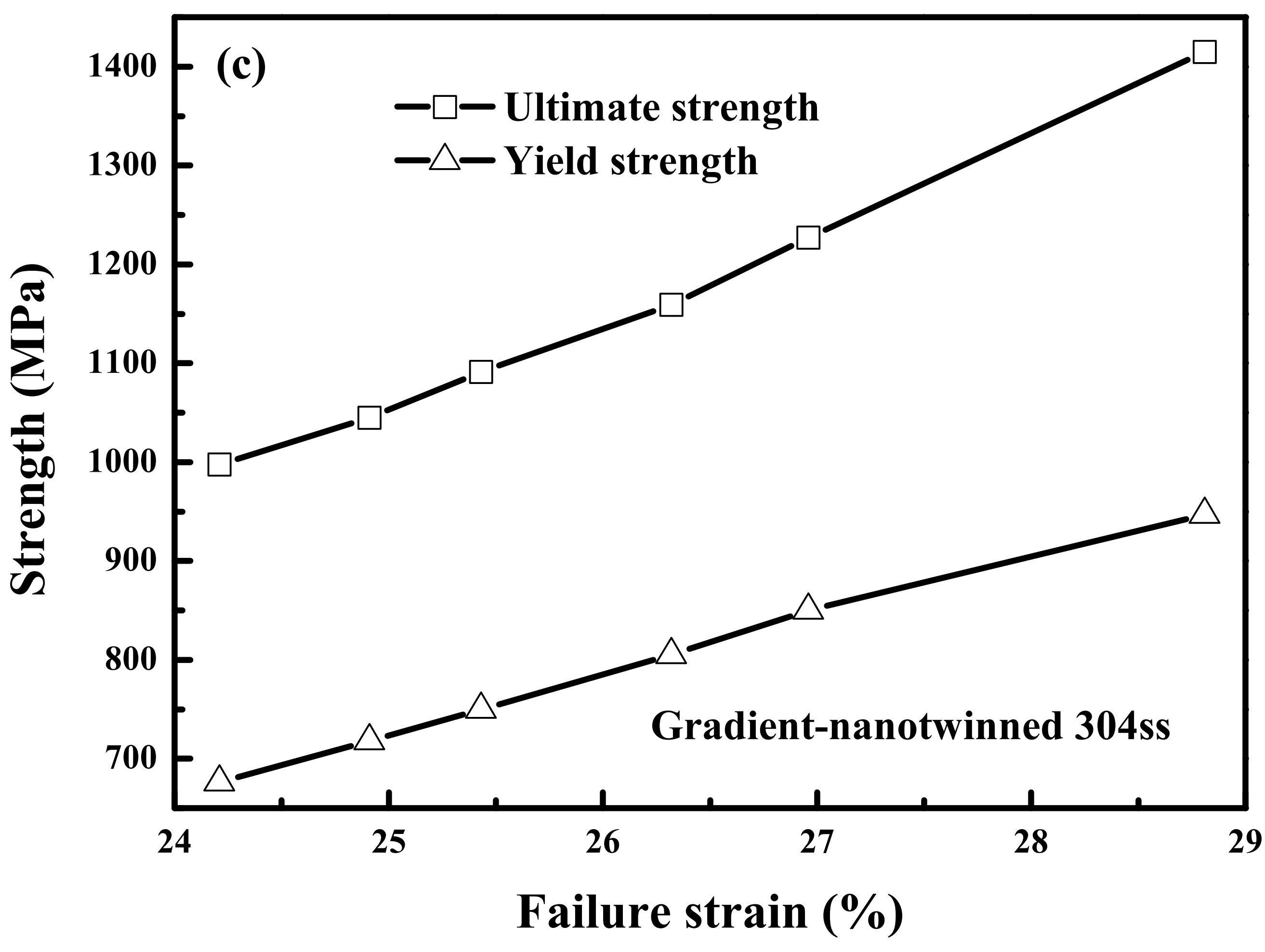
(c)
Ultimate strength
Yield strength
Gradient-nanotwinned 304ss
Strength (MPa)
Failure strain (%)
1400
1300
1200
1100
1000
900
800
700
24
25
26
27
28
29

Figure10a

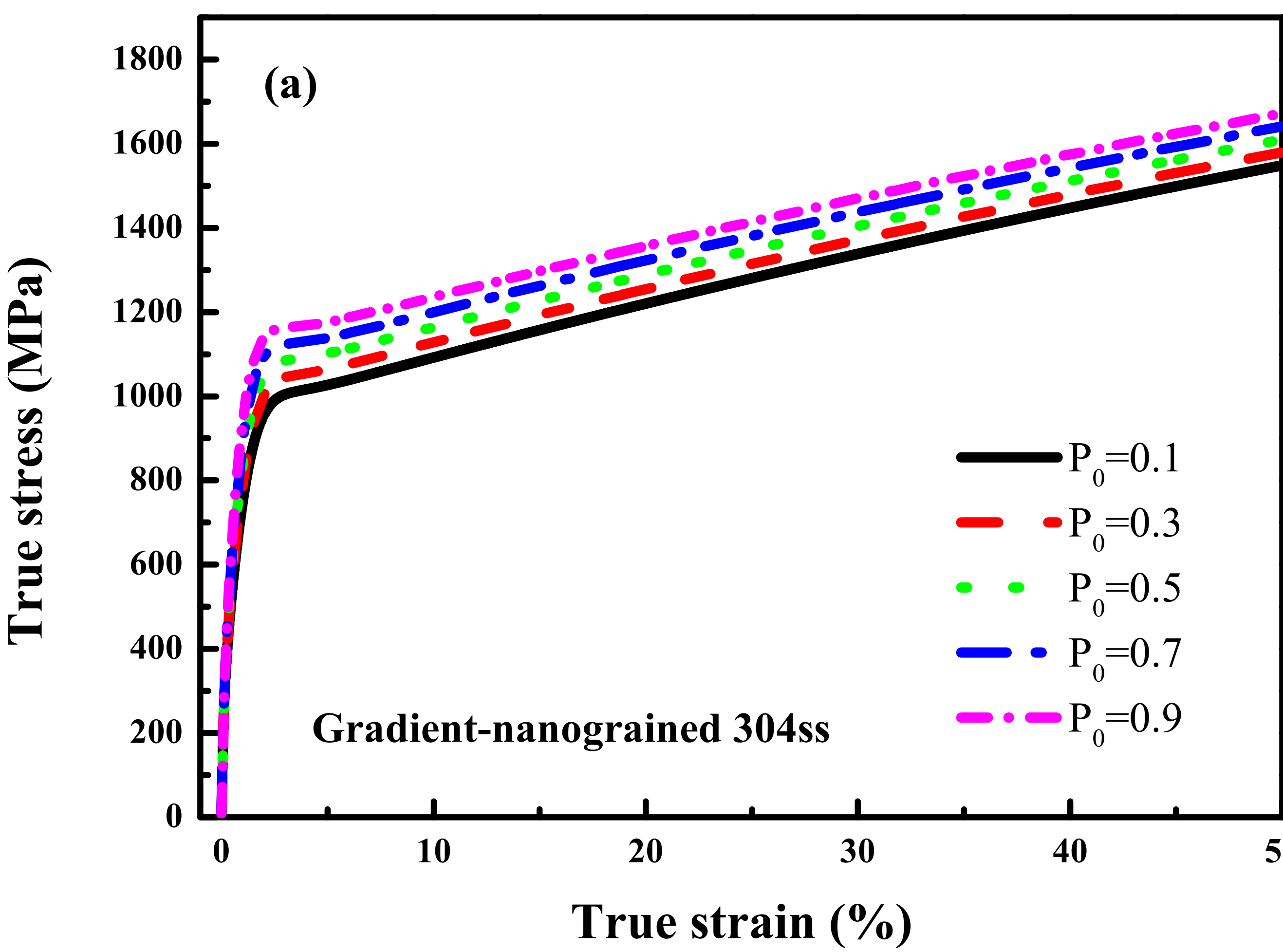

(a)
Gradient-nanograined 304ss
P_0=0.1
P_0=0.3
P_0=0.5
P_0=0.7
P_0=0.9
True stress (MPa)
True strain (%)
0
200
400
600
800
1000
1200
1400
1600
1800
0
10
20
30
40
50

Figure10b

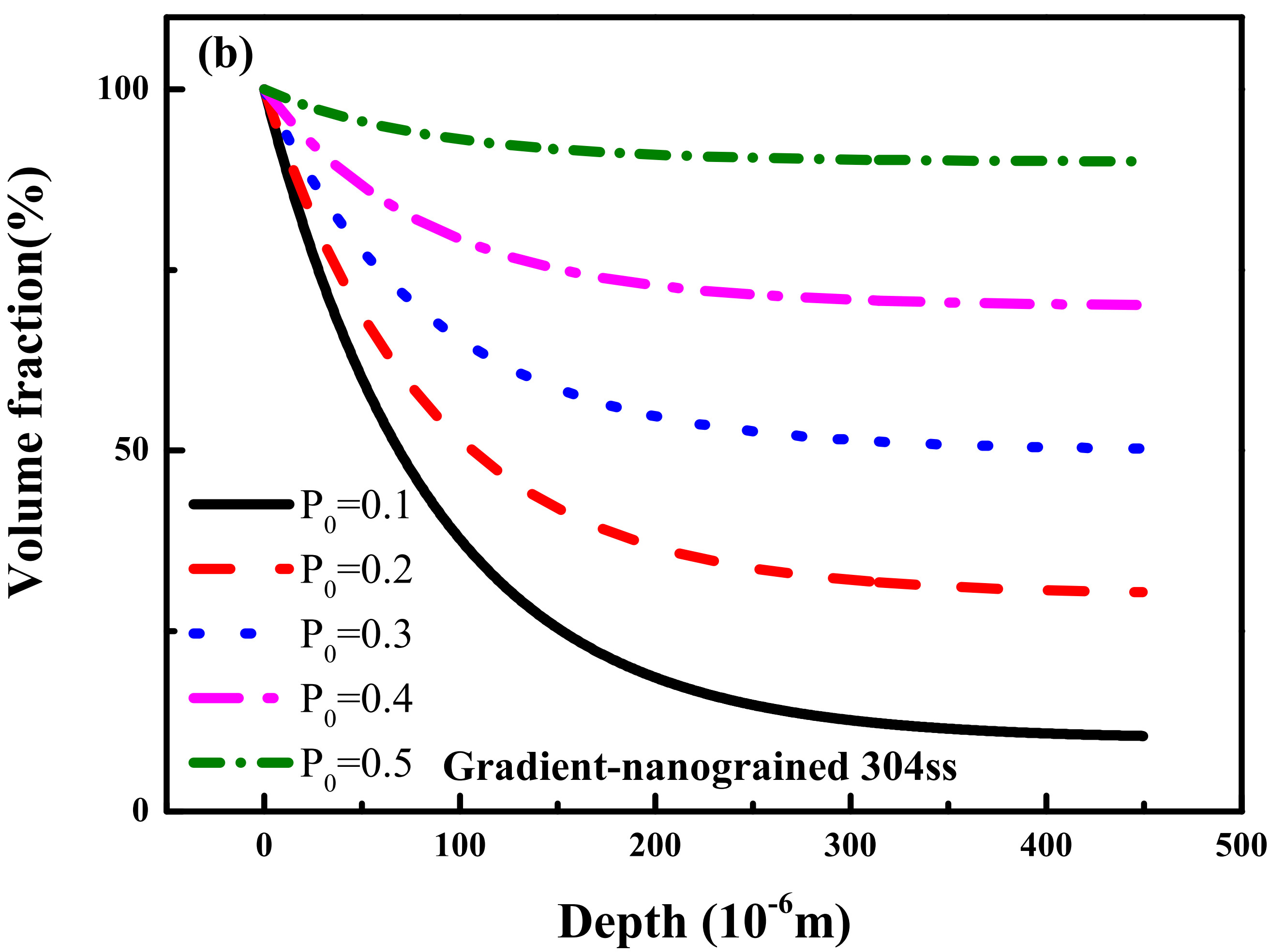

(b)
100
50
0
0
100
200
300
400
500
Volume fraction(%)
Depth (10-6m)
P0=0.1
P0=0.2
P0=0.3
P0=0.4
P0=0.5
Gradient-nanograined 304ss

Figure10c

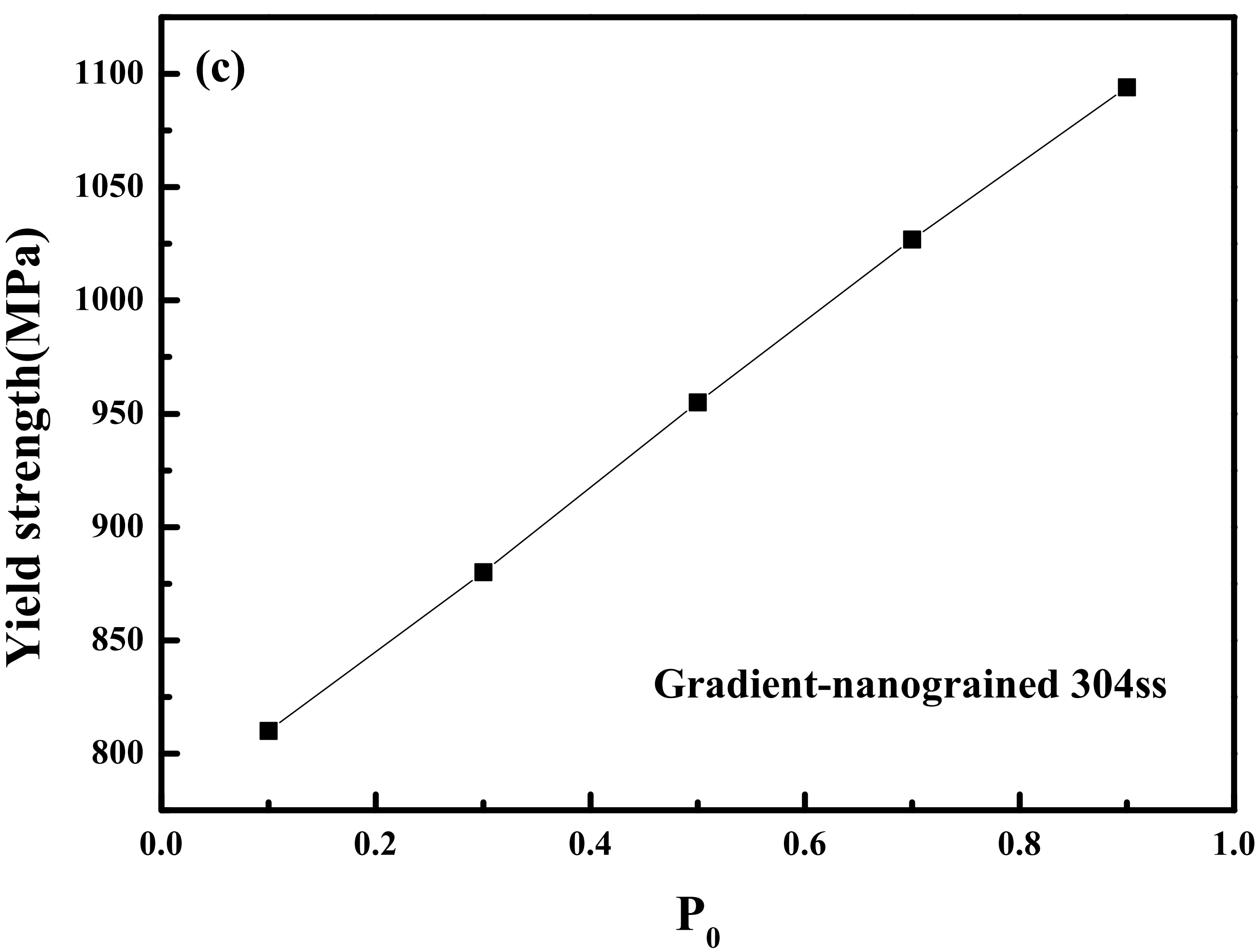

(c)
Yield strength(MPa)
1100
1050
1000
950
900
850
800
Gradient-nanograined 304ss
0.0
0.2
0.4
0.6
0.8
1.0
P_0

Figure10d

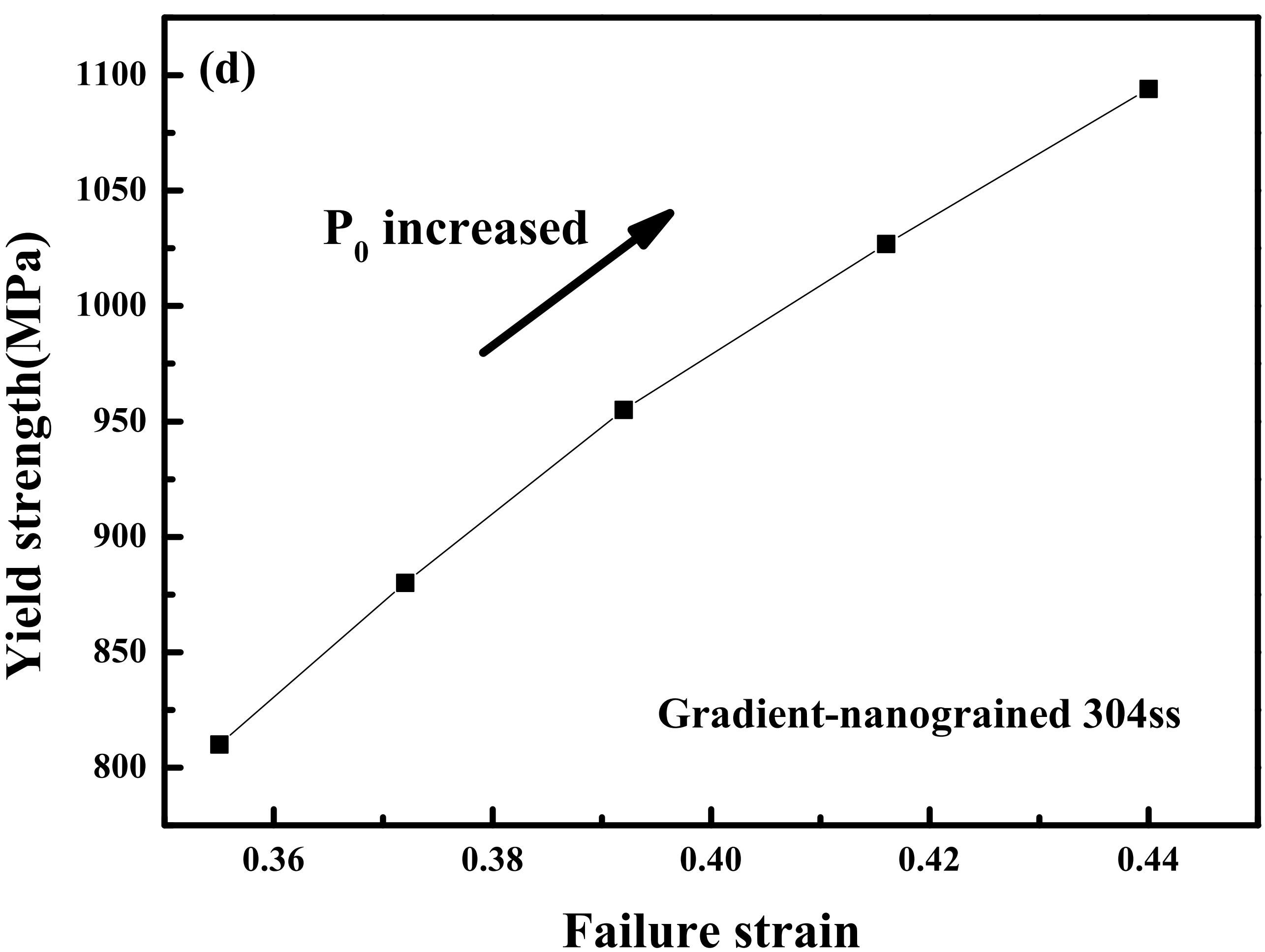

(d)
P_0 increased
Gradient-nanograined 304ss
Yield strength(MPa)
1100
1050
1000
950
900
850
800
0.36
0.38
0.40
0.42
0.44
Failure strain

Figure10e

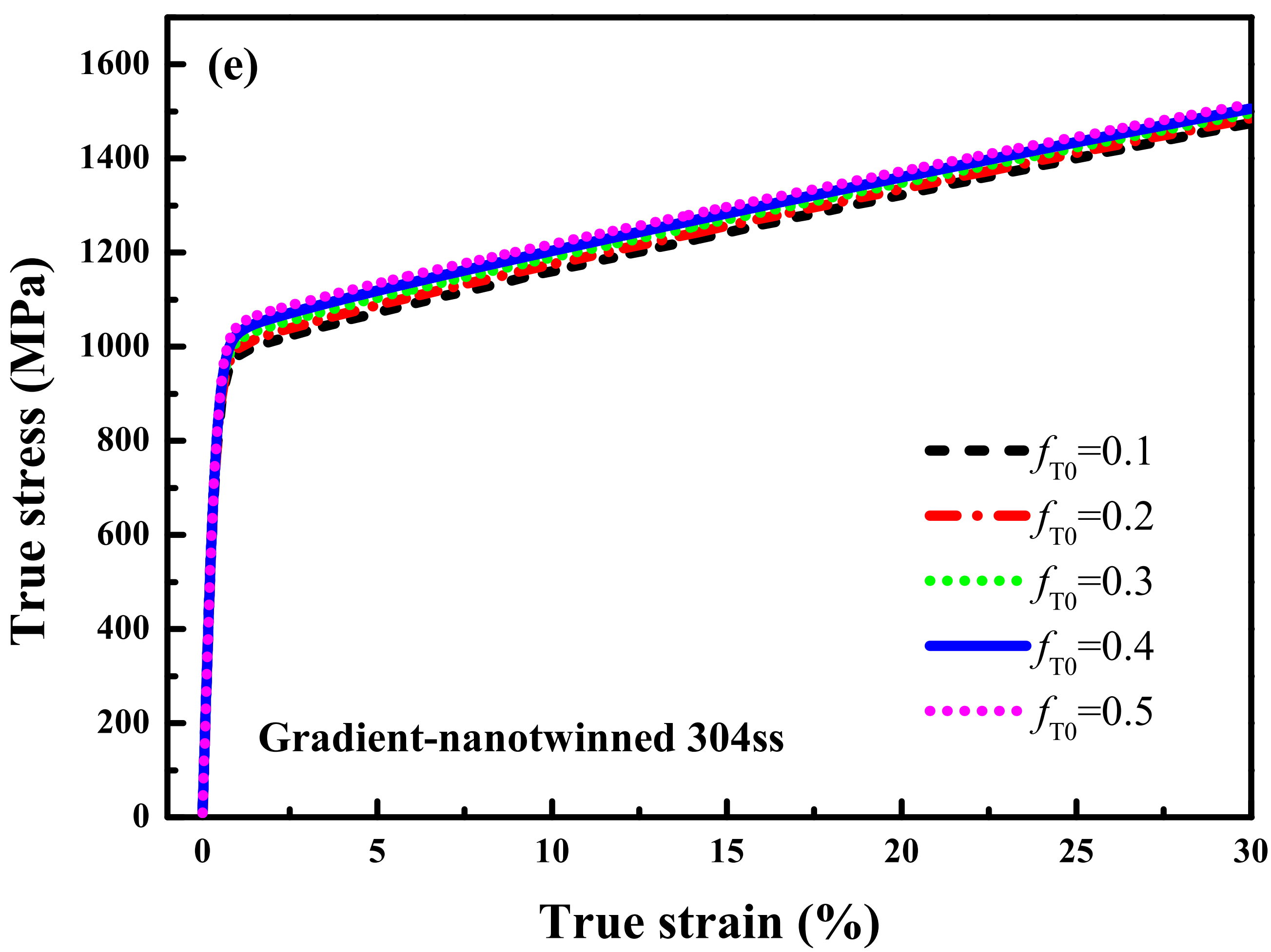
(e)
True stress (MPa)
1600
1400
1200
1000
800
600
400
200
0
0
5
10
15
20
25
30
True strain (%)
f_{T0}=0.1
f_{T0}=0.2
f_{T0}=0.3
f_{T0}=0.4
f_{T0}=0.5
Gradient-nanotwinned 304ss

Figure10f

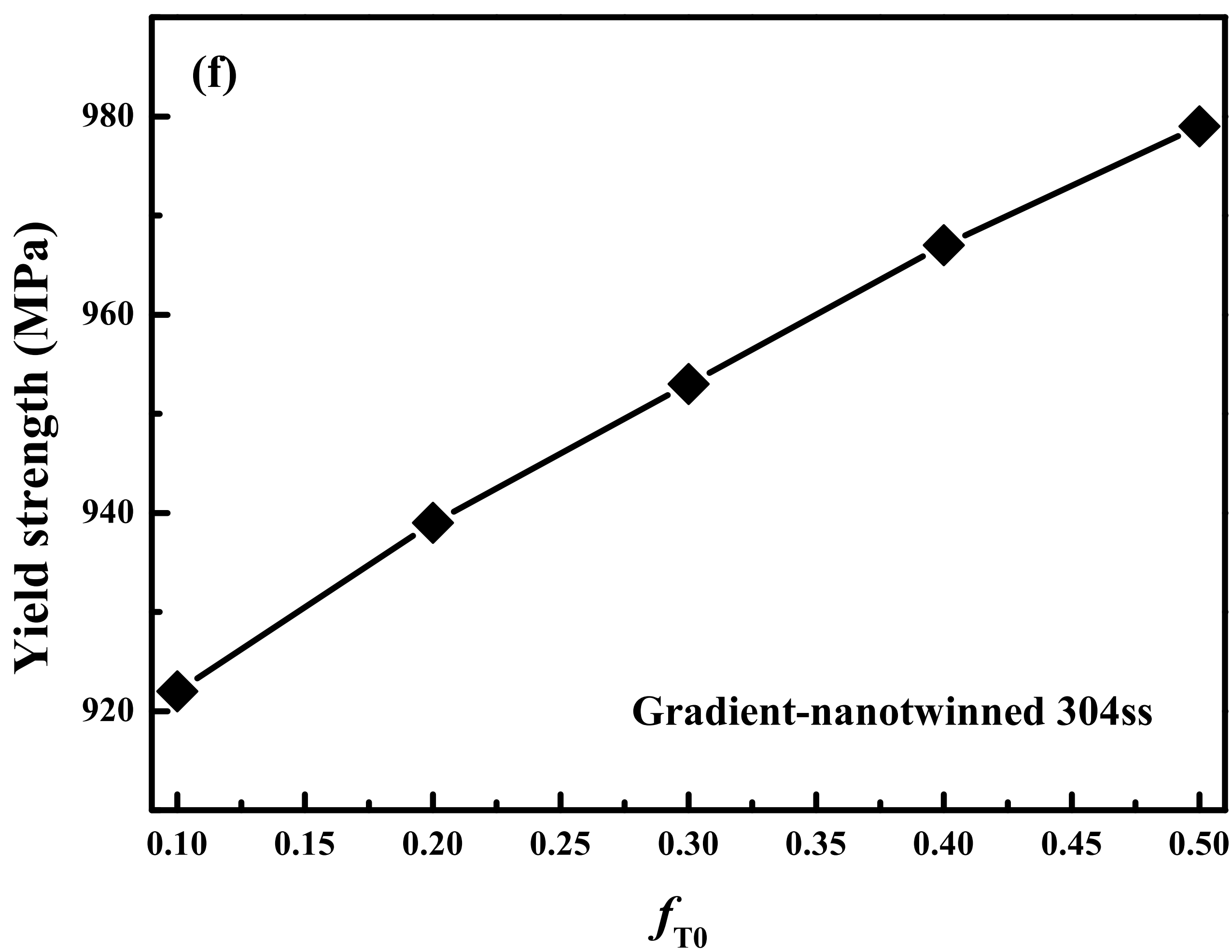
(f)
Gradient-nanotwinned 304ss
Yield strength (MPa)
980
960
940
920
0.10
0.15
0.20
0.25
0.30
0.35
0.40
0.45
0.50
f_{T0}

*Graphical Abstract